AFRL-AFOSR-VA-TR-2016-0089

Mo-Si-B Alloys and Diboride Systems for High-Enthalpy Environments: Design and Evaluation

DOUGLAS FLETCHER
UNIVERSITY OF VERMONT & STATE AGRICULTURAL COLLEGE

01/15/2016
Final Report

DISTRIBUTION A: Distribution approved for public release.

Air Force Research Laboratory
AF Office Of Scientific Research (AFOSR)/ RTB1
Arlington, Virginia 22203
Air Force Materiel Command

REPORT DOCUMENTATION PAGE

Form Approved
OMB No. 0704-0188

The public reporting burden for this collection of information is estimated to average 1 hour per response, including the time for reviewing instructions, searching existing data sources, gathering and maintaining the data needed, and completing and reviewing the collection of information. Send comments regarding this burden estimate or any other aspect of this collection of information, including suggestions for reducing the burden, to the Department of Defense, Executive Service Directorate (0704-0188). Respondents should be aware that notwithstanding any other provision of law, no person shall be subject to any penalty for failing to comply with a collection of information if it does not display a currently valid OMB control number.

PLEASE DO NOT RETURN YOUR FORM TO THE ABOVE ORGANIZATION.

1. REPORT DATE *(DD-MM-YYYY)*	2. REPORT TYPE	3. DATES COVERED *(From - To)*
14-12-2015	Final	15-09-2011 to 14-09-2015

4. TITLE AND SUBTITLE
MO-SI-B ALLOYS AND DIBORIDE SYSTEMS FOR HIGH-ENTHALPY ENVIRONMENTS: DESIGN AND EVALUATION

5a. CONTRACT NUMBER

5b. GRANT NUMBER
FA9550-11-1-0201

5c. PROGRAM ELEMENT NUMBER

5d. PROJECT NUMBER

5e. TASK NUMBER

5f. WORK UNIT NUMBER

6. AUTHOR(S)
Akinc, M., Kramer, M. J., Marschall, J., Perepezko, J., Ray, P. K., and Fletcher, D. G.

7. PERFORMING ORGANIZATION NAME(S) AND ADDRESS(ES)
University of Vermont and State Agricultural College, 85 Prospect St., Burlington, VT 05405
Iowa State University, 104 Marston Hall, Ames, IA 50011
University of Wisconsin-Madison, 1415 Engineering Dr, Madison, WI 53706
SRI International, 33 Ravesnswood Ave, Menlo Park, CA 94025

8. PERFORMING ORGANIZATION REPORT NUMBER

9. SPONSORING/MONITORING AGENCY NAME(S) AND ADDRESS(ES)
Air Force Office of Scientific Research
875 N. Randolph St, Room 3112
Arlington, VA 22203

10. SPONSOR/MONITOR'S ACRONYM(S)

11. SPONSOR/MONITOR'S REPORT NUMBER(S)

12. DISTRIBUTION/AVAILABILITY STATEMENT
Distribution A: Approved for Public Release

13. SUPPLEMENTARY NOTES

14. ABSTRACT
This final report summarizes work done by researchers from Iowa State University, University of Wisconsin- Madison, SRI International, and University of Vermont for this grant. The first two groups investigated candidate material systems for high-temperature aerospace applications. These investigations included theoretical, computational and experimental efforts, and focused mainly on molybdenum-silicon-boron and diboride alloy systems. These two groups also collaborated in the production of candidate test samples for evaluation in the inductively coupled plasma torch facility at the University of Vermont, and the molyborosilicate coating performed very well in plasma tests. Researchers from SRI International and the University of Vermont collaborated on the development of improved non-intrusive diagnostics aimed at providing measurements of key gas-surface interactions at plasma torch test conditions that could be related to flight environments. University of Vermont personnel focused their efforts on making quantitative measurements of key surface reaction rates from relative laser based measurements of the reacting species gradients near the surface.

15. SUBJECT TERMS
High temperature materials, ceramic materials, plasma testing, laser diagnostics,

16. SECURITY CLASSIFICATION OF:			17. LIMITATION OF ABSTRACT	18. NUMBER OF PAGES	19a. NAME OF RESPONSIBLE PERSON
a. REPORT	b. ABSTRACT	c. THIS PAGE			Douglas G. Fletcher
UU	UU	UU		100	19b. TELEPHONE NUMBER *(Include area code)* 802 656 9863

Standard Form 298 (Rev. 8/98)
Prescribed by ANSI Std. Z39.18
Adobe Professional 7.0

DISTRIBUTION A: Distribution approved for public release.

University of Vermont
Mechanical Engineering

201 Votey Bldg
33 Colchester Ave
Burlington, VT 05405

Mo-Si-B Alloys and Diboride Systems for High-Enthalpy Environments: Design and Evaluation

DISTRIBUTION A: Distribution approved for public release.

The UNIVERSITY of VERMONT	**CLASSIFICATION**		**CATEGORY**	
	1. Unclassified	☑	1. For approval	☐
	2. Industry	☐	2. For review	☐
	3. Restricted	☐	3. Other	☐
	4. Confidential			
University of Vermont Mechanical Engineering	**CONFIGURATION**			
	Controlled	☐	Not Controlled	☐

Agency	Program	Contract number:	Period:
AFOSR	High Temperature Materials	FA9550-11-1-0201	09/15/11 to 09/14/15

TITLE:

Mo-Si-B Alloys and Diboride Systems for High-Enthalpy Applications: Design and Evaluation

AUTHOR(S):
M. Akinc, M. J. Kramer, J. Marschall, J. Perepezko, P. K. Ray and D. G. fletcher

ISSUE.	Internal Reference Number	Number of pages: 99
Date: December 12, 2015 Issue 1 Rev. 0.	15/UVM/AFOSR/ICP-01	Number of included annexes: 0

SUMMARY:
This final report summarizes the work performed by researchers from Iowa State University, University of Wisconsin-Madison, SRI International, and University of Vermont during the four years of support from AFOSR Grant FA9550-11-1-0201. Given that this effort was a collaboration between material scientists from two universities (ISU and UW-M) and aerothermodynamicists from two institutions (SRI and UVM), each group pursued individual research paths while collaborating on the development of test samples for evaluation in plasma test facilities. The introduction of this report revisits the original objectives, and provides a summary of the important results of the research. Separate report sections follow with details of each investigation.

HOST SYSTEM	**HARDWARE EQUIPMENT.**	**MEDIA.**	**SOFTWARE.**
	Nature: Mac	Nature & Type: Identification:	Name: Microsoft Word 2010

KEY WORDS	**LANGUAGE CODE ENG**	**APPROVAL.**
Mo-Si-B alloys, diboride systems, ground test, high temperature materials, thermal protection material, laser diagnostics, heat flux		
		Laboratory: D. G. Fletcher

I. Investigation Objectives…….…….. 4

II. Objectives Accomplished …….…….…….. 6

III. Introduction……... 8

IV. Iowa State University Investigation…….…….…… 9

V. University of Wisconsin Madison Investigation ……...……..…… 51

VI. SRI International Investigation…….76

VII. University of Vermont Investigation……....82

I. Investigation Objectives

The overall objectives of the collaborative investigation were summarized in a four-year schedule that was included in the original combined proposal. These objectives are shown below to provide context for the reports that follow, but they have been rearranged for clarity by separating them into three categories: material science (ISU and UWM), diagnostics (SRI and UVM) and collaborative (all).

Material Science (ISU&UWM)

Year 1:

1.1 Characterize Mo-Si-B-TM bulk alloys and establish optimum phase distribution and TM content.
1.2 Perform computational analyses (thermodynamic and DFT) of the stability of advanced Mo-Si-B system alloys at UWM in concert with alloying efforts at ISU.
1.3 Conduct an experimental evaluation of the phase stability of the new alloy designs at UWM and ISU.
1.4 ISU and UWM will prepare test samples of the alloys for ICP facility testing (using UVM defined geometry) and evaluate post-test samples.

Year 2:

7.1 Process ZrB_2/SiC and ZrB_2/SiC/AlN composites and carry out detailed microstructural characterization.
7.2 Implement the integration of Mo-Si-B coating technology at UWM onto both Mo-Si-B alloys and Diboride composites provided by ISU.
7.3 Apply kinetic biasing and diffusion barriers to coatings to mitigate the development of any incompatible interphase reaction products at UWM.
7.4 Conduct a microstructure based FEM to evaluate the mechanical compatibility between the coating and substrate materials at UWM.
7.5 ISU and UWM will provide coated samples for ICP facility testing and evaluate sample performance.

Year 3:

3.1 Measure oxidation and mechanical properties of ZrB_2/SiC and ZrB_2/SiC/AlN composites as a function of temperature.
3.2 Establish optimum composition and processing parameters to obtain maximum density and oxidative stability of ZrB_2/SiC and ZrB_2/SiC/AlN composites.
3.3Thermo-gravimetric analysis at UWM will provide baseline to compare response of ICP-tested samples in concert with evaluations at ISU on other materials.
3.4 Further application of kinetic biasing at UWM will be used to optimize the coating/substrate compatibility and reduce oxygen transport to prolong lifetime.
3.5 Optimized bulk samples will be provided by ISU to UWM for coating and then sent to UVM for ICP testing.

Year 4:

4.1 Continue to optimize composition and microstructure of ZrB_2/SiC and ZrB_2/SiC/AlN composites for performance based on the ICP and FTIR feedback.
4.2 UWM will continue to supply coated samples for ICP testing and evaluation.

Diagnostics (SRI & UVM)

Year 1:

1.1 Set up and test simultaneous temperature, emittance, and spectral emission measurements at SRI using CO_2 laser heating and discharge-coupled flow cell.
1.2 Design, implement and compare results for several sample test configurations in UVM ICP based on achieved surface temperature and power settings.
1.3 Complete the boundary layer gradient measurements for carbon nitridation and evaluate CO production from graphite in air plasma in the UVM ICP facility.
1.4 Begin measurements of N-atom and O-atom gradients in air plasmas over fully- and non-catalytic surfaces using point-wise approach in UVM ICP facility.

Year 2:

2.1 Implement and test simultaneous surface temperature and emittance measurement capability in the UVM ICP facility.
2.2 Demonstrate diffuse-reflectance measurement capability and emittance estimation procedure at SRI.
2.3 Test performance of ICCD camera for detection of O- and N-atom gradients using discharge sources at SRI
2.4 Begin experiments for LIF detection of Si-, B-, and C- containing species using discharge sources at SRI.
2.5 Complete point-wise boundary layer surveys of N-atom and O-atom concentrations over fully- and non-catalytic surfaces in UVM ICP facility.
2.6 Test candidate material species production over a range of test gas enthalpies and pressures for UWM and ISU samples.

Year 3:

3.1 Begin FTIR emission measurements on CO_2-laser heated samples at SRI.
3.2 Continue experiments to optimize Si-, B-, and C-species LIF detection schemes in hot gas backgrounds and develop quantification procedures for key species.
3.3 Transfer ICCD camera to UVM and measure O- and/or N-gradients near catalytic surfaces in the ICP.
3.4 Compare the measurements with ICCD to those with point-wise approach to identify problems in quantifying species concentrations.
3.5 Continue parallel exploration of key species in the UVM ICP facility by testing ISU and UWM material samples and performing emission measurements.
3.6 Transfer and implement LIF diagnostics for Si-, B-, and C-species in the UVM ICP facility as they mature.
3.7 Employ the ICP facility diagnostics to provide insight on the coating behavior in the ICP environment (SRI and UVM).

Year 4:

4.1 Continue FTIR emission measurement experiments; design system for UVM ICP facility if the technique looks promising.
4.2 Continue to implement LIF diagnostics for Si-, B-, and C-species at the UVM ICP facility.
4.3 Demonstrate the measurement of concentration gradients for volatile surface reaction products in the UVM ICP facility for the test of a candidate TPS material in a trajectory-relevant plasma condition.

DISTRIBUTION A: Distribution approved for public release.

Full Collaboration

Year 4:

- Perform critical evaluation of material tests to identify data that can be used to benchmark development of physics-based models of gas-surface interactions.
- Employ the benchmark data set as a basis for a lifetime analysis and prediction kinetic model as a joint SRI, UWM and ISU collaboration.

II. Objectives Accomplished

A. Material Science

Regarding the Material Science objectives, the following sections contributed by ISU and UWM describe their respective efforts and accomplishments. Certainly they provided samples for testing in the UVM ICP Torch Facility in addition to carrying out their investigations into new, better-performing materials and coatings. One of the most difficult and frustrating aspects of this collaboration was the less than perfect reliability of the facility, which led to long delays in tests of materials. Winter testing at UVM was always subject to whether or not the ambient temperature on the building roof would allow the chiller to operate or not. Operation during the more temperate seasons was more reliable, but there were still the "normal" maintenance and repair issues, including: rebuilding the vacuum pump, fixing plumbing leaks and rebuilding the injection system and the induction zone. Efforts to reach higher material surface temperatures resulted in power supply operation at the limit of its capability, and this increased the rebuilding frequency.

Timely reporting of the test results to ISU and UWM was also an issue that was not addressed until the final year when the ICP lab at UVM adopted the policy of separate test reports for each sample test, so that there was no time lost in sending the report to the institution along with the sample so that it could be inspected at either institution.

The UWM final report was prepared well in advance of the deadline and sent to UVM before 01 August, 2015. The ISU report was delivered to UVM on 11 December, 2015. The delay in assembling the final report is entirely the fault of the PI at UVM.

B. Diagnostics

The objectives of the diagnostic technique development and implementation were shared by SRI International and UVM for the first three years of this investigation. After the SRI PI (Marschall) left the responsibility fell to UVM. All of the Year 1 objectives were accomplished, although the carbon nitridation work (1.3) developed into a PhD dissertation (A. J. Lutz) that finally finished in March, 2015. Although this investigation began with NASA funding in 2009, the final results, which included a direct demonstration of the fact that hot graphite his highly catalytic to nitrogen atom recombination, were funded entirely by AFOSR.

The second year objectives changed because the radiometer was still being tested at SRI, so (2.1) was postponed one year. Also the manufacture of the ICCD camera (Princeton

Instruments) decided NOT to honour the quote for the procurement that was used in the proposal (2.3). This led to a proposal to the Vermont Space Grant Consortium for supplemental funding to enable the purchase. Of course, this took until 2014 to execute, the camera was finally purchased and installed at the ICP Torch Facility (see UVM report for demonstration data) in year 4. This also meant that the development work was done entirely at UVM. SRI did complete the development of a laser diagnostic technique for BO (2.4). The point-wise boundary layer surveys of N and O atom concentrations in the boundary layers over fully and non-catalytic materials (2.5) was completed at UVM. This work provides a novel and important means for determining quantitative surface reaction rates for important gas-surface interactions. The first journal article describing these measurements has only recently been submitted, owing to the need to carefully check all aspects of the measured quantities. Note that this work was entirely funded by AFOSR and it provided the basis for measuring surface catalysed reaction efficiencies for flexible SiC coupons in support of the NASA HIAD effort. With the postponement of 2.1 and 2.3 to later years, all other second year objectives were accomplished. During this year AFOSR funding was used to pursue two objectives that were NOT in the original proposal. First, a doctoral student implemented a high-temperature gas property library into an open-source DNS code to enable simulations of the subsonic ICP torch facility for the gas mixtures being tested there. This work successfully concluded in March of 2015 with the thesis defense and publication. The most important aspect of this work is that it provides an on-site capability for developing more accurate models of gas-surface interactions. This work was entirely supported by AFOSR. Second, another graduate student used the SiC fabric samples to investigate material evolution and how that feeds back to the measurement of material surface properties in oxidizing environments. Except for the material samples, sample holder, and some SEM costs, this work was entirely supported by AFOSR.

During the third year, the SRI PI left the company after starting work on 3.1 and continuing work on 3.2. SRI also completed the transfer of the BO diagnostic information to UVM so that it can be implemented in the ICP Torch Facility (3.6). As UVM was directly purchasing the ICCD camera, objective 3.3 was moot. However, objective 3.4 was moved to year 4 when the ICCD camera was finally procured and installed at the facility. The major finding regarding the ISU and UWM samples during the third year was that the molyborosilicate coating performed extremely well, and provided no emitting species for detection. In contrast, the diboride samples provided by ISU and others continued to shed boron at a noticeably prodigious rate.

For the fourth year of the grant, the ICCD camera was implemented in the ICP Torch Facility (see the UVM report). Measurements of surface catalysed recombination for air plasma on copper showed that recombination happens first by $N+O+s \rightarrow NO+s$, and this is followed by a fast gas-phase exchange reaction $NO+N \rightarrow N_2+O$. As we had proposed to develop diagnostics for surface reaction products, an effort began to develop quantitative LIF of NO for both β ($B \leftarrow X$) and γ ($A \leftarrow X$) systems. To that end a MS student has written codes that predict the spectral distribution of ro-vibrational transitions that will be sued to extract temperature and concentration from the LIF measurements. This work will continue after the grant. This same student will also perform the BO LIF measurements using the SRI diagnostic approach.

C. Collaborative

We were less successful on the fully collaborative objectives that we would have hoped, but each group has benefited from the learning engendered from this ambitious collaborative investigation. While it was expected that the whole outcome would be greater than the sum of the parts, a realistic assessment states that the actual outcome is simply the sum. However, in our humble opinion, the sum is considerable.

III. Introduction

The following sections are the separate report from the investigators. The first section is the ISU report, and this is followed by the UWM report. Each of these reports is presented as delivered to UVM, and each is self-contained with references at the end of the report, as well as a summary of important statistics regarding graduate students, etc.

The third section is the journal article on BO LIF that represents the most important accomplishment of SRI International during this grant. Again, the article is self-contained with its own references. There are no statistics from SRI International, but the funding was used to support the PI (Marschall) and a post-doctoral researcher (Dr. Jason White), and to procure equipment and materials for developing the diagnostics.

The last section is a summary of the most important findings of the multiple investigations carried out at UVM. This is also self-contained with references and its final pages contain details of publications, presentations and graduate student support.

DISTRIBUTION A: Distribution approved for public release.

Table of Contents

Abstract 1

1. Introduction 2

2. Experimental Methods 5

2.1 Synthesis 5

2.2 Characterization and Testing 6

2.3 *Ab-initio* calculations 8

3. Research Highlights 10

3.1 Effect of W additions on the stability of A15 Mo_3Si phase 10

3.2 Transient Oxidation of Mo-W-Si-B alloys 13

3.3 Cyclic oxidation of Mo-W-Si-B alloys 16

3.4 Oxidation behavior of ZrB_2-SiC-AlN composites 19

3.5 Effect of AlN content on oxide scale evolution 23

3.6 Ultra-High Temperature testing of ZrB_2-SiC-AlN composites 29

3.7 Oxidation of coated UHTCs: collaboration with Univ. of Wisconsin, Madison 35

3.8 Oxidation in dissociated air: collaboration with Univ. of Vermont 37

4. Summary 39

5. Publications and Presentations 40

5.1 Journal Publications / articles under preparation 40

5.2 Conference Presentations 41

6. References 42

DISTRIBUTION A: Distribution approved for public release.

Abstract

The current work focuses on the development of high temperature materials for extreme environments, with emphasis on silica forming materials. The first class of silica forming alloys studied included materials in the Mo-Si-B system with alloying additions. Mo-Si-B alloys in the intermetallics rich region of the phase diagram are known to have excellent oxidation resistance, but poor fracture toughness. The alloys in the Mo rich section offer improved toughness, but poor oxidation resistance. In the current research, we attempted to destabilize the A15 phase that is common to both these composition regimes to synthesize materials comprising of a metal rich solid solution (which results in improved toughness) and the T1 Mo_5Si_3 and T2 Mo_5SiB_2 based intermetallics that result in excellent oxidation resistance. The amount of W required to destabilize the A15 phase was evaluated using a combination of *ab-initio* calculations and experimental studies. Following this, the oxidation behavior of these materials was studied at 1100 – 1500°C, and the effect of alloy chemistry and microstructure on oxidation resistance was established. It was seen that finer microstructures result in improved oxidation resistance, while W addition proves beneficial at elevated temperatures. In addition to Mo-Si-B alloys, ZrB_2-SiC-AlN composites were also assessed at elevated temperatures (1400 – 2000°C). The addition of AlN results in the formation of Al_2O_3 during the oxidation process, which acts as a viscosity modifier in the silica scale. Lower temperatures result in the formation of a relatively viscous silica scale. In these regimes, a lower ZrB_2 content, higher SiC content and an optimal AlN content was seen to result in improved oxidation behavior. With a progressive increase in temperature (and corresponding decrease in scale viscosity), the optimal compositions for oxidation resistance was seen to shift towards a ZrB_2 rich region.

DISTRIBUTION A: Distribution approved for public release.

1. Introduction

Speed, resilience and energy efficiency have been the key drivers for engineering research in the 21st century. For example, the need for vehicles and projectiles that fly faster directly fed the research on hypersonic technologies. Extreme velocities create extreme environments, which in turn calls for resilient materials capable of tolerating these conditions. In an increasingly energy conscious world, these objectives need to be met with maximal energy efficiency. This is a vicious cycle, as Carnot efficiencies for conventional fuel sources (fossil fuels, natural gas, nuclear, steam) increase as the temperature rises, and the environment poses increasingly harsh challenges. In short, development of materials for extreme environments will eventually dictate the technological progress in this century. Materials for ultra-high temperature environments must satisfy several stringent requirements that dictate a high melting temperature and stability in an oxidizing environment as well as other compatibility issues. While a few ceramic-based candidates have been identified such as zirconates, sialons and diborides, most of the recent attention has been focused on diborides (ZrB_2 and HfB_2) for ultra-high temperatures due to a number of attributes such as favorable mechanical and thermal properties. However, the diborides do not exhibit acceptable oxidation behavior as monolithic material since the oxidation reaction at high temperature yields a volatile B_2O_3 and a porous skeleton of ZrO_2 which is a fast ionic conductor of oxygen. This has been addressed in part by composite designs where SiC is incorporated with the diboride to provide an outer SiO_2 layer during oxidation. There are limitations to this approach. For example, SiO_2 decomposes to SiO(g) above about 1800°C and the reaction is enhanced at lower temperature in a combustion environment with water vapor and/or lower oxygen partial pressure in the combustion atmosphere. To enhance the oxidation resistance a number of different additives have been examined with the aim of altering the defect structure of ZrO_2 or modifying the constitution of the oxide scale (i.e. by promoting phase separation and increased viscosity). While there have been some improvements with these approaches, the oxidation attack is

DISTRIBUTION A: Distribution approved for public release.

still significant and limits the service life. Besides ceramic systems there are a number of metallic alloys under consideration, but the material that has demonstrated the most attractive performance and potential is based on alloys in the Mo-Si-B system. For Mo-Si-B alloys the borosilica coating that develops upon high temperature exposure has been shown capable of providing protection to 1400°C, but the performance is not satisfactory at ultra-high temperatures.

Composites based on ZrB_2/SiC for hypersonic vehicle leading edge applications have received considerable interest from the research community in recent years. The interest in this composite arises from the fact that both ZrB_2 and SiC have extremely high melting points (3245 and 2730°C (decomposes)), exceptionally high thermal conductivities (relative to most other ceramics) and low specific gravity compared to most refractory metals, making them attractive for aerospace applications. Due to their covalent bonding, processing of the powder compact to dense ceramics has been limited to hot pressing unless sintering additives are used at the risk of degrading high temperature strength and/or oxidative stability. Rapid oxidation of $ZrB_2$and SiC leads to formation of B_2O_3 and SiO_2 respectively. Borosilicate glass that forms from these oxides slows the oxidation of ZrB_2. Guo and Zhang showed that surface-layer oxidation leads to a SiC depleted layer. Although oxygen diffusion through the glass layer is relatively high at the temperatures of interest, it is believed that preferential evaporation of B_2O_3 at hyper-velocity conditions leads to a silica-rich glass layer which acts as an oxygen diffusion barrier preventing further oxidation at least at moderate temperatures. At higher temperatures the loss of the SiO_2 layer thickness is accompanied by substrate recession. Furthermore, if water vapor is present the degradation of SiO_2 is accelerated, further reducing the upper temperature limit for the active-passive transition.

To improve the processing of ZrB_2/SiC composites a number of additives were used with varying degrees of success. Among them, addition of AlN appears to be promising. Addition of AlN to the ZrB_2/SiC composite offers multiple attractive properties including high thermal conductivity, high melting point, thermodynamic compatibility with the constituents of the composite and finally, oxidation of AlN leads to formation of Al_2O_3 which modifies the viscosity of the borosilicate glass

DISTRIBUTION A: Distribution approved for public release.

substantially.

In this project we looked to develop new materials in this system by addressing the following challenges –

a) Understand the phase stability of Mo-Si-B alloys and microstructure development with W additions.

b) Study the effect of W additions and alloy microstructure on oxidation resistance.

c) Understand the role of additives such as AlN on the role of oxidation resistance of ZrB_2-SiC-AlN composites

d) Test base materials and coated alloys at high temperatures to assess their oxidative stability.

DISTRIBUTION A: Distribution approved for public release.

2. Experimental Approach

2.1 Synthetic Methods

Mo-Si-B based alloys were synthesized using two different routes, namely casting and solid state sintering. The cast alloys were synthesized by arc-melting of pure elemental chips (Alfa Aesar, +99.5%) on a water cooled copper hearth in an inert argon atmosphere. The alloy buttons were re-melted a minimum of four times in order to ensure adequate homogeneity. The high melting temperature of W resulted in minor W segregation initially. This problem was overcome by adopting a two-stage synthesis process. In the first stage, WSi_2, having a relatively low melting temperature (2160°C) was cast and remelted thrice. In the second stage, the WSi_2, along with the balance elements was cast by arc-melting and remelted four times. The as-cast button was again re-melted on a cylindrical copper mould and drop-cast to form a cylinder. The alloys were heat treated at 1850°C in an atmosphere of flowing ultra-high purity argon in tantalum containers. The heating as well as the cooling rates were controlled at 20°C/min. Studies on phase stability and oxidation was carried out using discs sectioned from the drop-cast cylinders.

Alloys and composites were also prepared by solid-state sintering, using methods adopted by Zhang et.al[1]. Mo-W-Si-B alloys were prepared using elemental powder of Mo, W, Si and B of 99.95%, 99.9%, 99.9%, 94-96% purity and with an average particle size of ~3-7micron, ~0.5 micron, ~1-5 micron, ~<5 micron, respectively, procured from the Materials Preparation Center, Ames Laboratory. ZrB_2-SiC-AlN composites were synthesized using ZrB_2 (Grade B, ~2 μm particle size, H.C.Starck, Karlsruhe, Germany), SiC (Grade UF-10, ~1μm particle size, H.C.Starck, Karlsruhe, Germany) and AlN (Grade C, ~1μm particle size, H.C.Starck, Karlsruhe, Germany) powders. Ceramic powders were wet milled in a plastic jar using WC as milling media using roller mill (Cole-Parmer Lab mill 8000, Vernon Hills, IL) and methyl ethyl ketone (MEK) as solvent for 24 hours. The powders were contaminated by a small amount (≈1-2%) of WC from milling media which is believed to be beneficial as a sintering aid [2]. The

DISTRIBUTION A: Distribution approved for public release.

mixture was milled for another 24 hours after binder (QPAC40, polypropylene carbonate) addition. Following wet milling, the solvent was evaporated at 40°C in vacuum. The sample was ground and sieved through a 300 µm sieve. Cylindrical samples were prepared by pressing powders, first uniaxially, followed by cold isostatic pressing at 310 MPa. The binder was burned out at 600°C for one hour in flowing argon atmosphere before sintering. The Mo-W-Si-B samples were sintered for 6 hours at 1900°C using a tungsten resistance furnace (M-60, Centorr Technologies). The ZrB_2-SiC-AlN samples were placed in a BN-coated graphite crucible and sintered in an electrical resistance furnace equipped with graphite heating elements (3060-FP20, Thermal Technology Inc., Santa Rosa, CA). The sintering profile included two one-hour isothermal holds at 1250°C and 1450°C in vacuum to remove the surface oxides. Samples were then sintered at 2000°C in flowing helium atmosphere for two hours.

2.2 Characterization and testing

The sintered samples were assessed using the Archimedes method according to the ASTM standard B962-13 for estimation of sintered densities. Theoretical densities were estimated using the rule of mixtures under the assumption that there was no change in composition during sintering. Microstructures and phase assemblages of the sintered samples were studied using a JEOL 5910Lv scanning electron microscope (SEM), a FEI Quanta-250 SEM and a Philips PANalytical x-ray diffractometer (XRD) using Cu-K_α radiation in a Bragg-Brentano geometry equipped with a double-bent monochromator for stripping the Cu-$K_{\alpha II}$ radiation. Composition mapping were done using the FEI Quanta-250 SEM equipped with Oxford Aztec energy-dispersive x-ray analysis system. Microprobe measurements were carried out using wavelength-dispersive spectroscopy (WDS). The WDS measurements were carried out using JEOL JXA-8200 microprobe. Data was acquired at an accelerating voltage of 20KV, with a beam current of 20 nA. Si-K_α, Mo-L_α and Nb-L_α lines were used for analysis. A counting time of 10 seconds on the peak and 5 seconds on the background on either side of the peak was used. Approximately 100 points were collected for each sample using automated data analysis. Cross

DISTRIBUTION A: Distribution approved for public release.

sections of the samples were polished before analysis. The samples were etched with molten NaOH/KOH (1:1 molar ratio) at ~200°C to reveal the ZrB_2 grain boundaries for estimation of the grain sizes. Measurements were done from 3 representative areas of each sample, and the grain sizes estimated using an Image Analysis program (Image J).

The cyclic oxidation tests, as well as the transient oxidation tests for Mo-W-Si-B alloys were carried out in flowing air in a tube furnace at the desired temperatures for various time intervals. Cyclic oxidation tests for the ZrB_2-SiC-AlN composites were carried out in a box furnace at different temperatures for varying time intervals. Samples were placed on ZrO_2 crucibles for these experiments, and no significant reaction was observed between the samples and the crucibles over the duration of the test. The oxidized surface was studied using variety of characterization tools such as SEM, XRD and X-ray Photoelectron Spectroscopy (XPS). The XPS measurements were done using PHI™ Physical Electronics 5500 Multitechnique ESCA system with monochromatic Al Kα radiation (1486.6 eV). The peak positions were determined with reference to the adventitious carbon peak at 284.6 eV. The atomic concentration was calculated by using the sensitivity factors provided with the PHI™ acquisition software.

The ultra-high temperature cyclic oxidation tests were carried out in the Ames Thermal Plasma Spray Facility. A plasma gun (SG-100, Praxair Surface Technologies, Indianapolis, IN), with a power input of 40kW was used for heating the test samples to the target temperature (2000°C). Argon was used as the plasma gas and helium was used as auxiliary gas (gas pressure 10.3 bar (150 psi) and 3.4 bar (50 psi) respectively). A ZrO_2 coated graphite hollow cylinder with a hollow push rod was used to hold the test specimen. A separate vacuum line was used against the rear surface of the sample through the push rod to hold the sample in place. A manual sliding sample holder system was designed to change the sample standoff (distance from the sample's anterior surface to the plasma gun). The gun and sample holder were placed inside a vacuum chamber. A pressure of 100 torr was used for the test with continuous air supply. The oxygen content was measured to be 21% by an oxygen sensor (MAX-250E, Maxtec Inc, Murray, UT) whose probe was placed ~1 inch from the sample front surface. Sample surface temperature

DISTRIBUTION A: Distribution approved for public release.

was measured by a two color optical pyrometer (Modline 5R-3015, Ircon Inc., Santa Cruz, CA) through a window at an angle. The pyrometer was calibrated using type R/S thermal couple (Omega Engineering Inc., Stamford, CT) and black body, with the accuracy of the measurements being ± 10°C. All compositions were subjected to ten minutes one- and five-cycle testing. The sample was place 6 mm above the holder (with ~14mm inside the hollow holder) for each test. The front surface and the 6mm length side surface were included in the surface area calculation. All the tests were started at an identical standoff to maintain identical initial heating rate. The standoff was adjusted manually during the test to maintain 2000 (±50)°C for ten minutes. For cyclic tests, the samples were cooled in vacuum for 30 minutes with plasma gun off before it was removed for measurement and inspection and reloaded for next cycle. The temperature was recorded during test using ModView software (Ircon Inc., Santa Cruz, CA) at 1.5 seconds intervals.

2.3 Ab-initio Calculations

The first principles calculations were carried out in the present work using the Vienna *ab-initio* simulation package (VASP) within the framework of the density functional theory (DFT). The calculation is conducted in a plane-wave basis, using the projector-augmented wave (PAW) method with ultra-soft pseudo-potentials [3]. The exchange and correlation items are described by the generalized gradient approximation (GGA), and the cutoff energies are 320 and 535 eV for the plane wave basis and augmentation charge respectively. During the relaxation calculation, the energy criteria are 0.01 and 0.1meV for electronic and ionic relaxations respectively, while for calculation of the density of states (DOS), the criterion is 0.001 meV. The k-point grid used for structural relaxation was 6×6×6, chosen according to the Monkhorst-Pack scheme [4], and symmetry reduced to the irreducible Brillouin zone. The calculations for the M_3Si ($M=Mo_{1-x}Nb_x$ or $M=Mo_{1-x}W_x$) phase were carried out using a super cell of the A15 structure of z M atoms and y Si atoms across the entire range of x. The amounts of Nb and Mo as

DISTRIBUTION A: Distribution approved for public release.

well as W and Mo were varied to calculate the formation enthalpies. The DOS for this structure was also calculated as a function of Nb and W content.

DISTRIBUTION A: Distribution approved for public release.

3. Research Highlights

3.1 Effect of Nb and W additions on the phase stability of the Mo_3Si phase

A combination of theoretical and experimental studies was employed to study the stability of Mo_3Si with Nb and W substitutions. *Ab-initio* calculations suggested that beyond critical levels of Nb additions, the formation enthalpy increases sufficiently to result in a destabilization of the A15 phase (figure 1a). In case of W additions, a monotonic increase in energies was observed, suggesting a possible destabilization as well (figure 1b). The density of states was plotted in conjunction with the formation enthalpies to study the phase stability. It was seen that with increasing levels of Nb and W additions, the Fermi surface moves out of the pseudo-gap indicating a structural instability (figure 2). The theoretical calculations provided a guide for experimental work. It was assessed using a combination of x-ray diffraction and electron microprobe measurements that ~ 27.5 atom % Nb was required for destabilizing the A15 phase. Similarly, for W containing alloys, 8-10% of W additions were sufficient to destabilize the A15 phase. Furthermore, Vegard's law was followed with progressive Nb and W additions, until the destabilization of the A15 phase. It was further dete rmined that upon destabilization of the A15 structure, Nb partitions preferentially to the T1 phase, whereas W partitions preferentially to a solid solution with Mo.

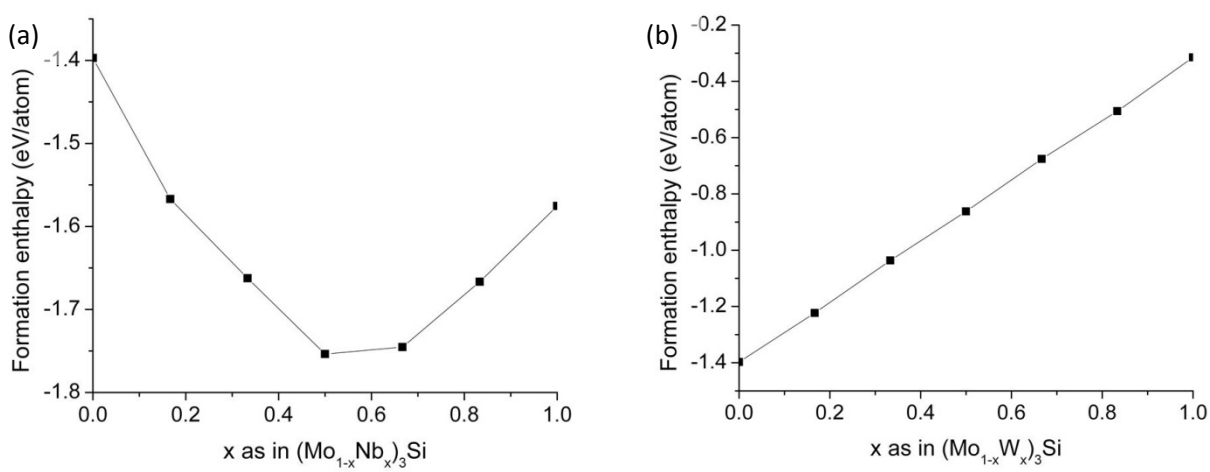

Figure 1: Formation enthalpy of the A15 Mo_3Si phase with (a) Nb and (b) W additions

DISTRIBUTION A: Distribution approved for public release.

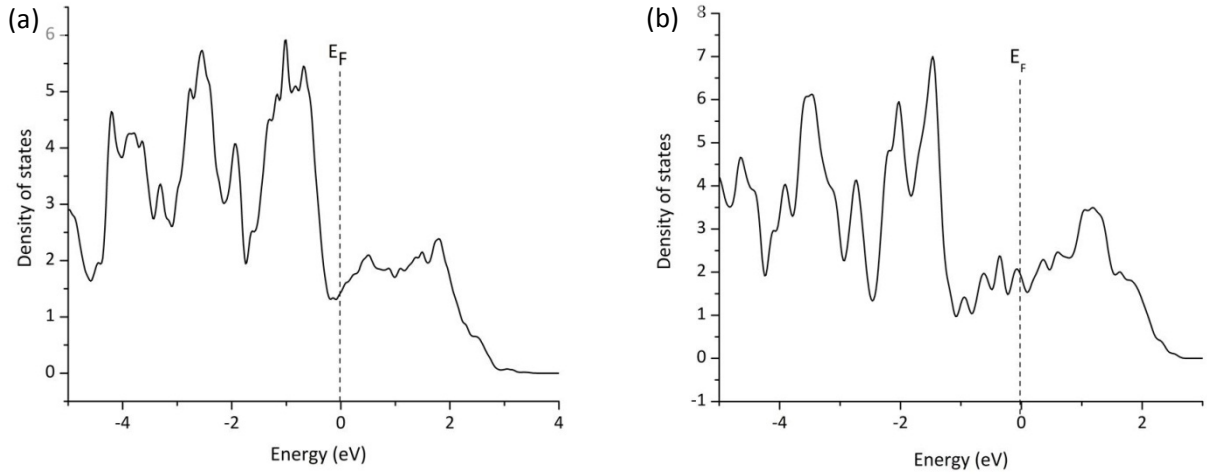

Figure 2: Density of States of the Mo_3Si phase with (a) 27.5 atom % of Nb and (b) 10 atom % W substitutions

Miedema described the interactions occurring at the interface of the Wigner-Seitz cell of an element being solved in another using an interfacial enthalpy term [5-7], which is a function of the electronegativity difference between the elements and the difference in the electron density at the Wigner-Seitz cell boundary of the elements. This term has a parallel in the interaction parameter as it is defined in the CALPHAD approach. Essentially, this is a measure of the strength of interaction between two atoms when brought together. This value, for solvation of Si in Mo was determined to be -120 kJ/mol of Si, whereas the corresponding value for solvation of Si in Nb was determined to be -195 kJ/mol [6-8]. Similarly, the interfacial enthalpy for solvation of Mo in Si is -126 kJ/mol of Mo while that for solvation of Nb in Si is -216 kJ/mol of Nb [6-8]. Therefore, the Nb-Si interaction is stronger compared to the Mo-Si interaction. With increasing levels of Nb substitution at the expense of Mo content, the contribution of Nb-Si interactions becomes more significant as compared to the Mo-Si interactions. In addition to the Mo-Si and Nb-Si interactions, Mo-Nb interactions need to be considered as well. The interfacial enthalpy values estimated for solvation of Mo in Nb is -22 kJ/mol of Mo, while the corresponding value for Nb in Mo is -23 kJ/mol of Nb. This metal-metal interaction is significantly weaker than the two metal-metalloid interactions. Consequently, initial Nb substitution serves to stabilize the Mo_3Si compound as evidenced by an initial reduction in formation enthalpy estimated from the *ab-initio* calculations (see Figure 1a).

DISTRIBUTION A: Distribution approved for public release.

However, once the number of Nb-Si pairs get saturated, further substitution of Nb leads to Nb-Nb interactions replacing the Mo-Nb interactions, which, by definition have interfacial enthalpy of zero. Consequently, an increase in the formation enthalpy is predicted. Since the Nb-Si interactions are stronger than the Mo-Si interactions and much stronger than the Mo-Nb interactions, the increase in formation enthalpy beyond a critical Nb content occurs with a slope that is shallower than the slope observed during the initial decrease in the formation enthalpy. This is in fact observed in our *ab-intio* calculations, where an initial decrease in the formation enthalpy followed by an increase. This would indicate an initial stabilization of the A15 compound followed by a subsequent destabilization beyond a certain level of Nb substitution.

The interfacial enthalpy for solvation of Si in W has been reported as -102 kJ/mol whereas the corresponding value for solvation of W in Si has been reported as -110 kJ/mol [6-8]. This would indicate that W-Si interactions are weaker than Mo-Si interactions (-120 and -126 kJ/mol respectively). Substitutionally, the interfacial enthalpy for solvation of Mo in W, as well as that of W in Mo has been reported as -1 kJ/mol [6-8]. Therefore, W substitution resulting in W-Si interactions at the expense of Mo-Si interaction will only serve to raise the formation enthalpy of the A15 compound (figure 1b). The Mo-W interactions are only slightly stronger than the Mo-Mo interaction; hence the slight decrease in formation enthalpy due to an increase in Mo-W interactions will be far outweighed by the significant increase in formation enthalpy due to the increased number of weaker W-Si interactions. Therefore, in this case, unlike the Mo-Nb-Si system, a monotonic increase in formation enthalpy is to be expected. With progressive W substitution, the two competing phases would be the Mo-W solid solution and the $(Mo,W)_5Si_3$ T1 phase. Using similar arguments as above, it would appear that W substitution would not reduce the formation enthalpy of either of these phases. However, the phase assemblage could still be more stable than the A15 structure if W preferentially partitioned into the solid solution, leaving only a relatively small amount of W available to substitute for Mo in the T1 phase. In such an event, the T1 structure would still contain a fairly large amount of Mo-Si interactions in comparison to the A15 phase resulting in the destabilization of the A15 structure. The key experimental results from this study have

DISTRIBUTION A: Distribution approved for public release.

been summarized in x-ray diffraction patterns with progressive Nb and W substitutions, shown in figure 3.

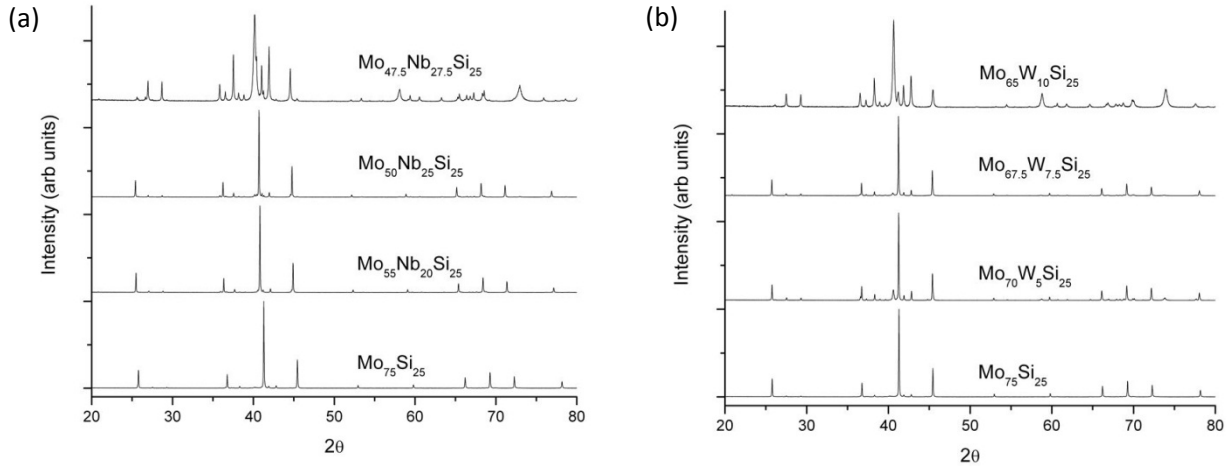

Figure 3: X-Ray diffraction pattern from (a) $(Mo,Nb)_3Si$ and (b) $(Mo,W)_3Si$ samples

3.2 Transient Oxidation of Mo-W-Si-B alloys

In order to understand the development of a protective oxide scale on Mo-W-Si-B alloys, the initial stages of oxidation were studied at 1100 and 1400°C. The same region in the samples was tracked, and the surface micrographs from this region were recorded to monitor the changes in the surface oxide scale with oxidation time. Two alloy compositions were synthesized ($Mo_{70}Si_{15}B_{15}$, henceforth referred to as W0 and $Mo_{55}W_{15}Si_{15}B_{15}$, henceforth referred to as W15) to study the effect of W substitution on the oxidation behavior. The alloys were synthesized using two different routes (solid state sintering and drop-casting) to understand the role of microstructure on the transient oxidation behavior. The oxide scale was seen to rapidly cover the surface of the W0 alloy at 1100°C. Surface coverage was attained faster for finer microstructures, i.e. for the drop-cast samples as opposed to the solid state sintered samples. Finer surfaces require lesser length scales that the glassy borosilicate scale being formed needs to flow, thereby resulting in improved oxidation resistance. These results are in agreement with the work of Rioult et.al.[9]. The oxidation resistance of the W15 sample was relatively poor due to incomplete scale coverage. Oxidation of W0 results in the formation of MoO_3, which volatilizes as $(MoO_3)_3$ from the surface.

DISTRIBUTION A: Distribution approved for public release.

Subsequently, once the Mo features evaporate, the borosilicate scale can flow and cover the surface. W15 on the other hand contains a significant level of W, which oxidizes to form WO_3. The vapor pressure of $(WO_3)_3$ is significantly lower than that of $(MoO_3)_3$[10]; hence it doesn't evaporate as fast, impeding the surface coverage by the borosilicate scale. The microstructural evolution of W0 and W15 drop-cast samples has been shown in figure 4, whereas the oxidized surfaces after 2 minutes of exposure at 1100°C have been shown in figure 5. Figure 6 shows the vapor pressures of $(MoO_3)_3$ and $(WO_3)_3$ with temperature.

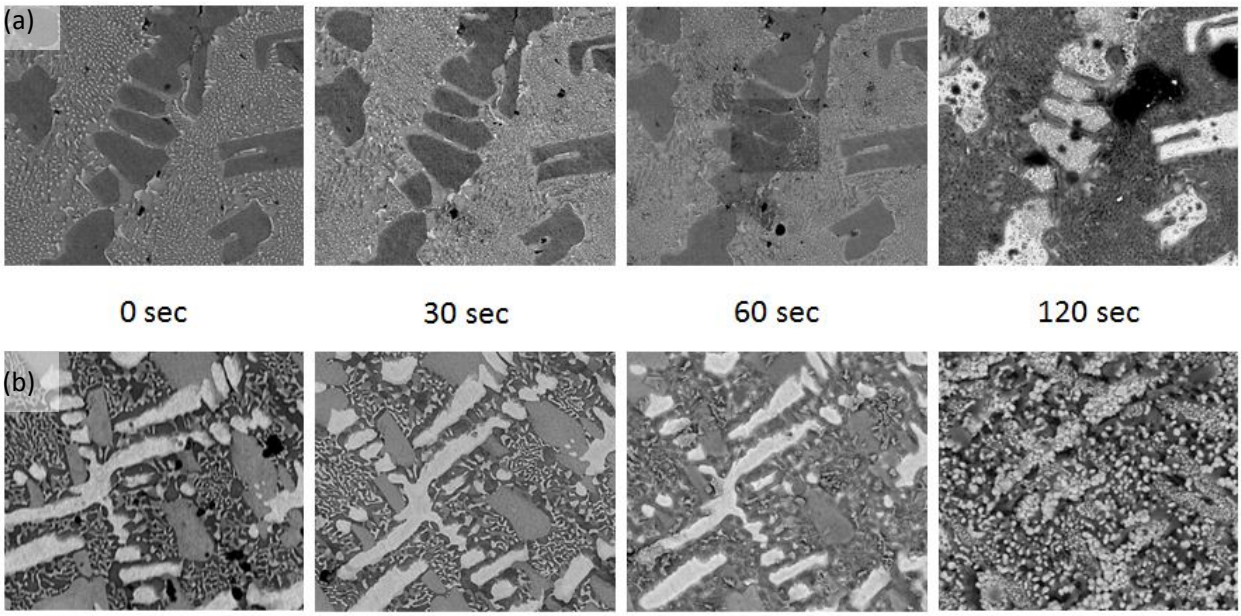

Figure 4: Evolution of surface oxide with time during oxidation of (a) W0 and (b) W15 samples

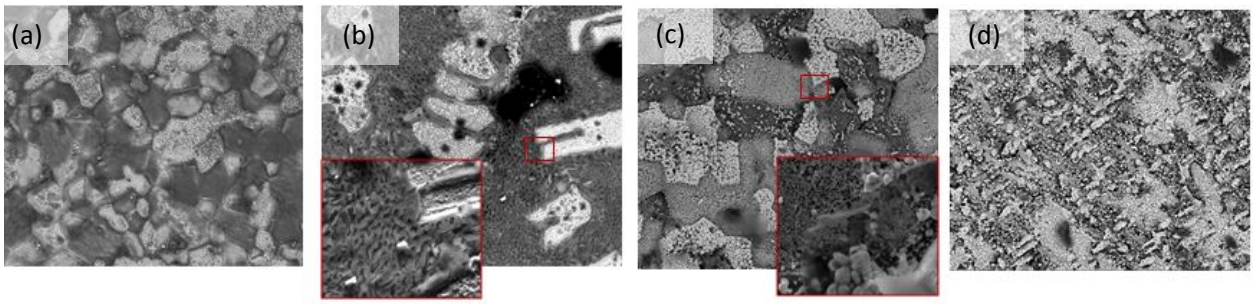

Figure 5: Comparison of the oxidized surface microstructures after 2 minutes at 1100°C (a) W0, sintered; (b) W0, cast; (c) W15, sintered and (d) W15 cast.

DISTRIBUTION A: Distribution approved for public release.

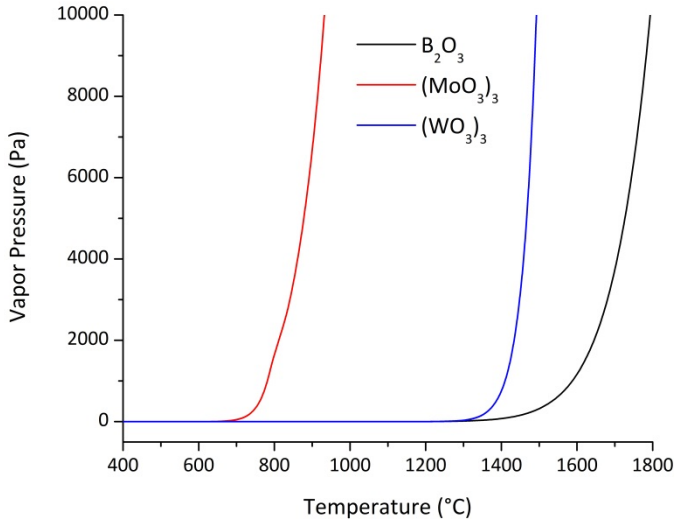

Figure 6: Vapor pressures of $(MoO_3)_3$, $(WO_3)_3$ and B_2O_3 as a function of temperature

As the oxidation temperature is increased to 1400°C, both $(MoO_3)_3$ and $(WO_3)_3$ evaporate, although $(MoO_3)_3$ is expected to evaporate much faster than $(WO_3)_3$. Consequently, significantly improved scale coverage is observed for the W15 sample in comparison to the oxidation studies at 1100°C. Figure 7 shows the evolution of

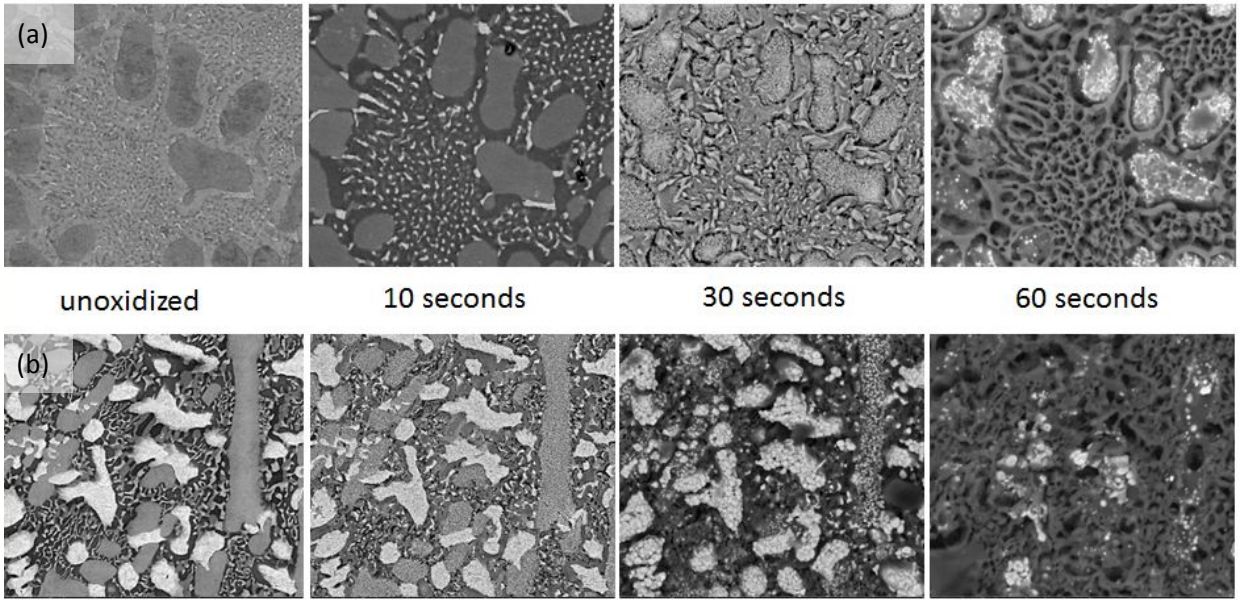

Figure 7: Comparison of the oxidized surface microstructures after 1 minute at 1400°C (a) W0, sintered; (b) W0, cast; (c) W15, sintered and (d) W15 cast.

the oxide scale with time for drop-cast W0 and W15 samples over a period of 60 seconds at 1400°C. At elevated temperatures, the role of microstructures assumes increasing significance for the W15 samples. Figure 8 shows the surface oxide scale formed after 1 minute on the different samples, i.e. drop-cast and

DISTRIBUTION A: Distribution approved for public release.

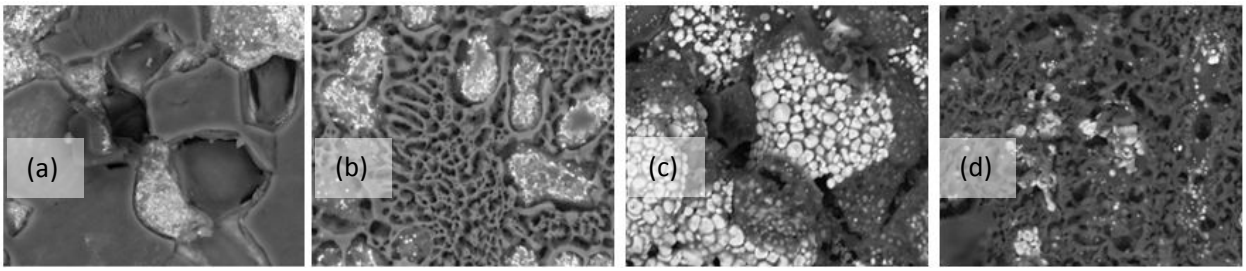

Figure 8: Comparison of the oxidized surface microstructures after 1 minute at 1400°C (a) W0, sintered; (b) W0, cast; (c) W15, sintered and (d) W15 cast.

solid-state sintered W0 and W15 samples. It can be seen that the drop-cast samples, again, perform better than solid-state sintered samples with the borosilicate scale providing a better surface coverage. Therefore, it can be concluded that (a) finer microstructures result in improved oxidation resistance due to better surface coverage by a protective oxide scale and (b) W substituted alloys show adequate oxidation resistance at elevated temperatures, which is consistent with the findings of Yoon et.al. on the oxidation of WSi_2[11].

3.3 Cyclic Oxidation of Mo-W-Si-B alloys

The oxidation behavior of a drop-cast $Mo_{50}W_{20}Si_{15}B_{15}$ alloy was studied cyclically in the 1000 – 1500°C temperature range. The addition of W to Mo-Si-B system resulted in destabilization of the A15 phase resulting in an almost complete removal of this phase from the microstructure (figure 9). The

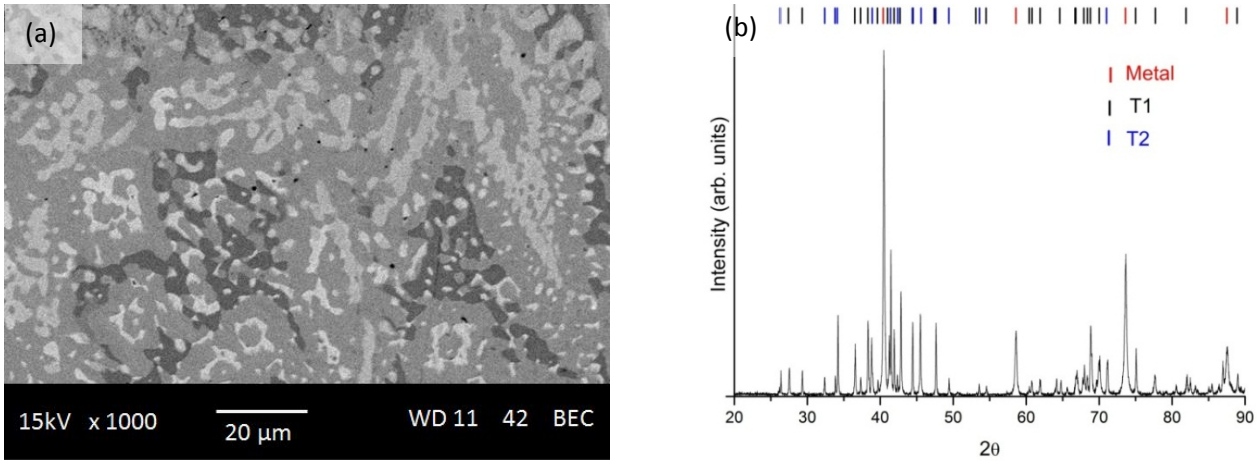

Figure 9: (a) Microstructures of the W substituted alloy showing a metal rich (bright) phase, a T1 $(Mo,W)_5Si_3$ with a dark contrast and a T2 $(Mo,W)_5SiB_2$ phase with a gray contrast and (b) x-ray diffraction showing the presence of three phases – Metal rich bcc solid solution, T1 and T2.

DISTRIBUTION A: Distribution approved for public release.

destabilization of the A15 phase leads to the formation of a metal rich (Mo,W) solid solution and a $(Mo,W)_5Si_3$ T1 phase. In addition to the (Mo,W) solid solution and the T1 phase, a $(Mo,W)_5SiB_2$ T2 phase was also observed in the microstructure. Based on the cyclic oxidation kinetics and the oxidized microstructures, it was seen that W additions result in a marked improvement in the oxidation behavior at temperatures T ≥ 1300°C with respect to a comparable Mo-Si-B alloy. In contrast, at temperatures below 1200°C, the oxidative stability deteriorated due to an enhanced pesting range. Appropriate pre-treatments were employed to address this issue.

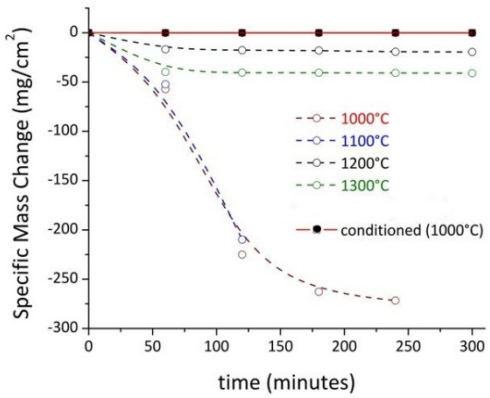

Figure 10: Oxidation kinetics of Mo-W-Si-B alloys as a function of temperature

The oxidation kinetics of these alloys is shown in figure 10. The W modified alloy loses significant mass at lower temperatures, i.e. at 1000 and 1100°C. However, this alloy appears to approach a steady state oxidation behavior at 1200 and 1300°C. These results appear to mirror the work of Yoon et. al. [11]. They observed that the oxidation resistance of WSi_2 deteriorates as the temperature was increased to 1200°C. However, a further increase in temperature to 1300°C resulted in a lower mass change. This apparent improvement in oxidation behavior at 1300°C was attributed to the rapid formation of an exclusive SiO_2, with the $(WO_3)_3$ steadily volatilizing. The presence of boron in the alloy under investigation is likely to change the kinetics of oxide scale development, due to the formation of a glassy borosilicate layer, which covers the surface of the alloy. Boron modifies the viscosity of the glassy oxide scale, and therefore provides rapid surface coverage in comparison to a pure silica scale [12]. Yoon et. al. attributed the rapid oxidation behavior of WSi_2 at 1200°C to the formation of cracks and pores during the pesting of W, which resulted in numerous short-circuit diffusion pathways for the oxygen. The presence of the glassy borosilicate scale allows the cracks and pores in the surface to get covered faster.

Figure 11 shows the cross-section microstructures after oxidation at 1200°C and 1300°C respectively for 5 hours. A glassy borosilicate oxide layer forms on the surface at both temperatures, with

DISTRIBUTION A: Distribution approved for public release.

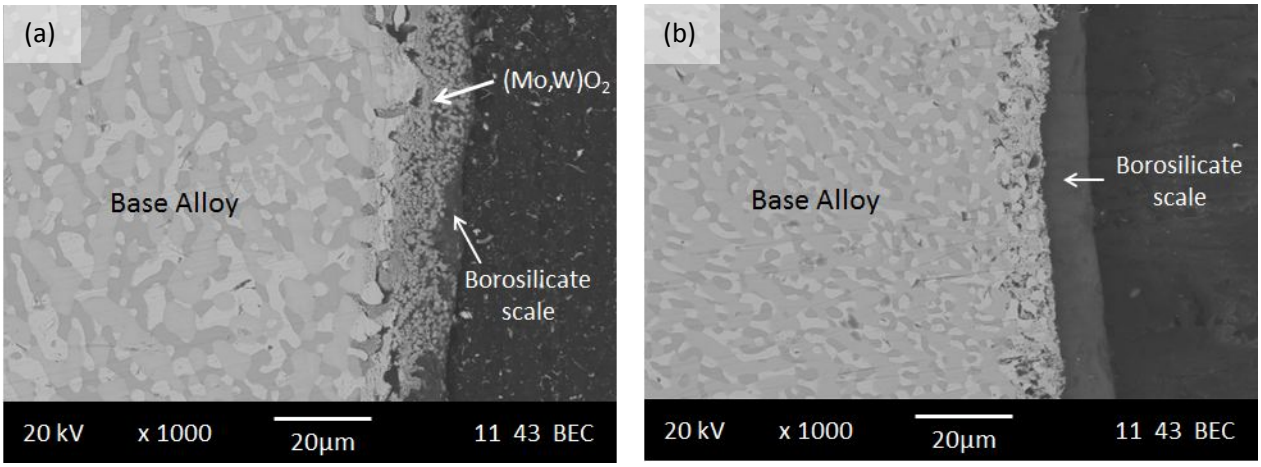

Figure 11: Cross-section micrographs after oxidation for 5 hours at (a) 1200°C and (b) 1300°C

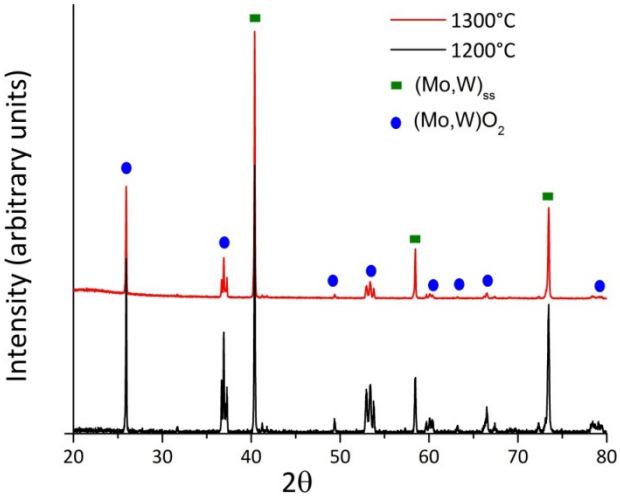

Figure 12: X-Ray diffraction patterns after oxidation at 1200 and 1300°C for 5 hours

the alloy oxidized at 1300°C exhibiting a thicker borosilicate scale. The amount of WO_x entrapped in the oxide scale is significantly larger at 1200°C as opposed to 1300°C. While the vapor pressure of $(MoO_3)_3$ starts increasing sharply as a function of temperature around 700°C, the vapor pressures of $(WO_3)_3$ shows a qualitatively similar increase at temperatures approaching 1300°C [10]. Consequently a greater amount of the oxides of W remain entrapped in the borosilicate scale at 1200°C as compared to 1300°C. These results bear some parallel to the oxidation studies on pure W coated with Si + B by Lu-Steffes et. al. [10]. They observed the formation of an aluminoborosilica layer (alumina being present as a consequence of the pack-cementation process involving inert alumina filler), with a significant amount of WO_3 remaining entrapped in the scale. The uncoated alloy presents a virgin surface containing all four elements Mo, W, Si and B in terms of (Mo,W) solid solution, T1 $(Mo,W)_5Si_3$ and T2 $(Mo,W)_5SiB_2$. Mo oxidizes to form MoO_3, which rapidly volatilizes as $(MoO_3)_3$ at the temperatures being studied. The rate of evaporation of $(WO_3)_3$ is much slower in comparison to $(MoO_3)_3$; hence a significant

DISTRIBUTION A: Distribution approved for public release.

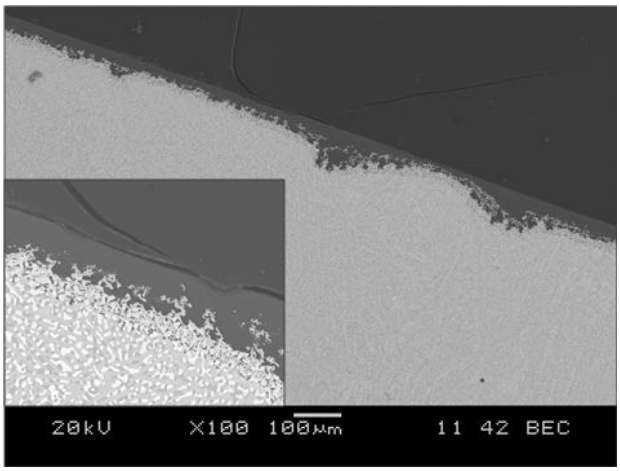

Figure 13: Cross-section micrograph following pre-treating at 1500°C

amount of WO_x stays entrapped in the oxide scale. The presence of boron and silicon results in the formation of a low viscosity borosilicate layer that results in a faster surface coverage (in comparison to pure SiO_2). At temperatures of 1100°C and below, the growth rates of the borosilicate scale is rather slow [11], and the silicon and boron content too low for complete surface coverage. Hence, a significantly larger mass change occurs, as the alloy coupons pest completely. Therefore, it is inferred that lower temperatures (T < 1200°C) represent the more severe oxidative conditions for this alloy. Figure 12 shows the x-ray diffraction patterns collected from the surface of the oxide scale. The diffraction patterns show a small hump around $2\theta = 20°$, which is due to the formation of a glassy borosilicate scale. In addition to this, the metal peaks can be seen clearly. Furthermore, peaks ascribed to $(Mo,W)O_2$ show up as well. The formation of a borosilicate scale results in a drop in the oxygen partial pressure in the subscale region. The low oxygen partial pressure results in the formation of the metal dioxide instead of the trioxide. Pre-treating the alloys at 1500°C for 5 hours resulted in the formation of a continuous silica scale on the surface (figure 13). Subsequent oxidation of pre-treated alloys showed a very small mass change even at the lower temperatures; hence this could be one way of improving oxidation resistance of these alloys.

3.4 Oxidation behavior of ZrB_2-SiC-AlN composites at 1600°C

The effect of AlN substitution on oxidation of ZrB_2-SiC was evaluated at 1600°C. Substitution of ZrB_2 by AlN, with 30 vol% SiC resulted in improved oxidation resistance with a thinner scale and reduced oxygen affected area. Substitution of AlN for SiC on the other hand, resulted in a deterioration of the oxidation resistance with an abnormal scale and significant recession. The effect of SiC content was

DISTRIBUTION A: Distribution approved for public release.

also studied, and was found to be consistent with the literature for the composites without AlN additions. A similar effect was observed when AlN was added, with the higher SiC content materials showing improved oxidation resistance. X-ray photoelectron spectroscopy (XPS) showed the presence of Al_2O_3 and SiO_2 on the surface, which could possibly lead to a modification in the viscosity of the glassy oxide scale. Possibly, the oxidation behavior of ZrB_2-SiC composites can be improved with controlled AlN additions by adjusting the Al:Si ratios.

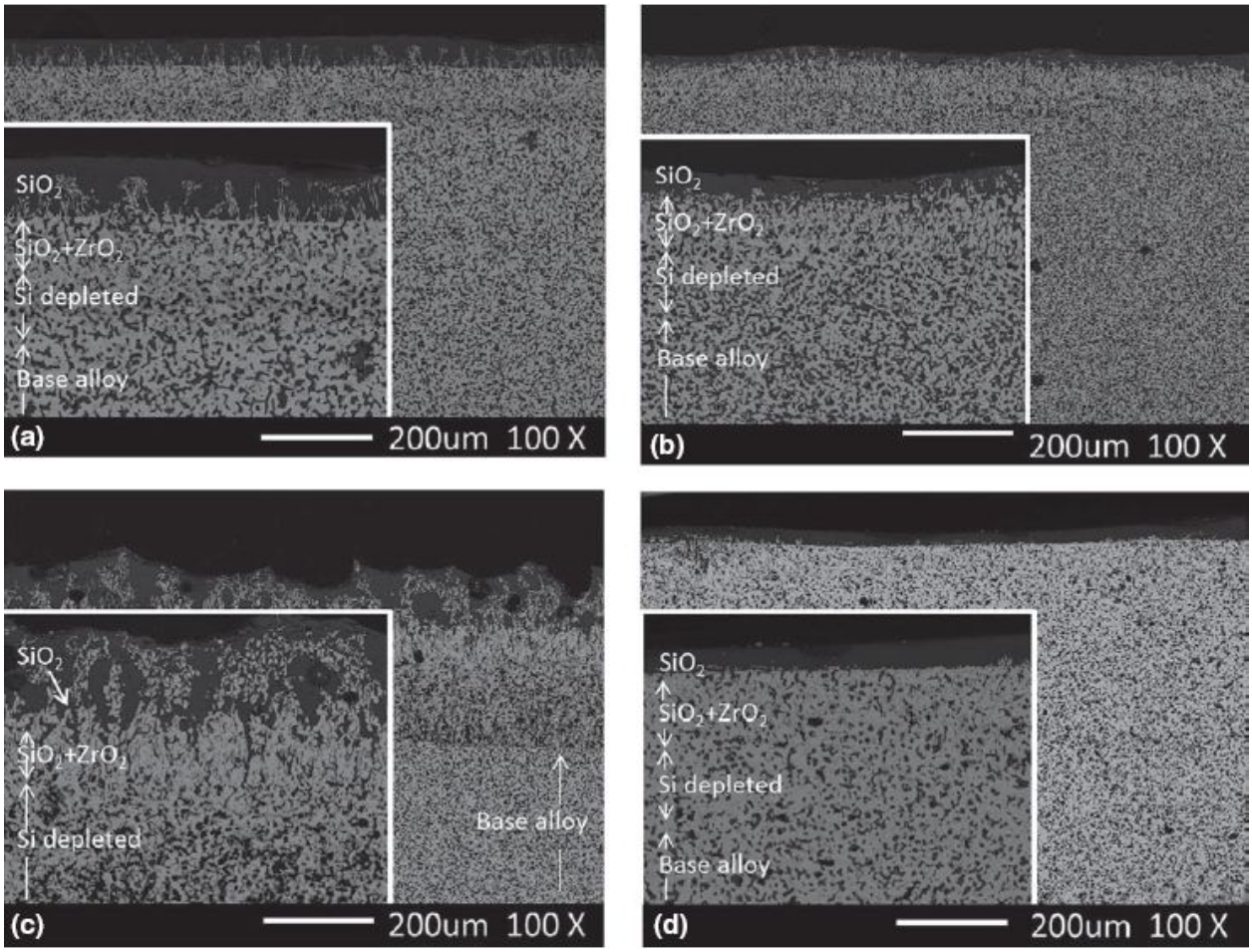

Figure 14: Cross-section microstructures of the 1600°C, 5-h oxidized coupons—(a) ZS73, (b) ZSA631, (c) ZSA721, and (d) ZS82. The inset shows the structure of the oxide scale at a higher magnification (300x).

Figure 14 shows cross-section microstructures of these composites after oxidation at 1600°C for 5 hours. ZrB_2-30 vol% SiC (ZS73), ZrB_2-30 vol% SiC- 10 vol% AlN (ZSA631) and ZrB_2-20 vol% SiC – 10 vol% AlN (ZSA721) show a degree of similarity in their oxidation behavior, with the scale comprised

DISTRIBUTION A: Distribution approved for public release.

of three layers. While the thickness of these layers differed for each sample, the general nature remained the same. The top layer exhibiting a dark contrast corresponds to the silica scale. ZS73 (Figure 14a) and ZSA631 (Figure 14b) exhibit a thinner continuous oxide scale in comparison to ZSA721 (Figure 14c). ZSA721 has numerous pores and discontinuities within the oxide scale. Additionally, ZSA721 sample also shows the presence of ZrO_2 channels perpendicular to the surface, extending well into the oxide subscale. Multiple ZrO_2 clusters could also be seen throughout the microstructure. High oxygen diffusivity in ZrO_2 is well known in comparison to other oxides such as HfO_2 or SiO_2 [13,14]. Hence, the presence of ZrO_2 channels and clusters exacerbates the oxidation of the composite. The oxidized microstructures of ZrB_2-20 vol% SiC (ZS82) showed the similar layered microstructures, but followed by a large and irregular Si depleted region, as shown in figure 14(d).

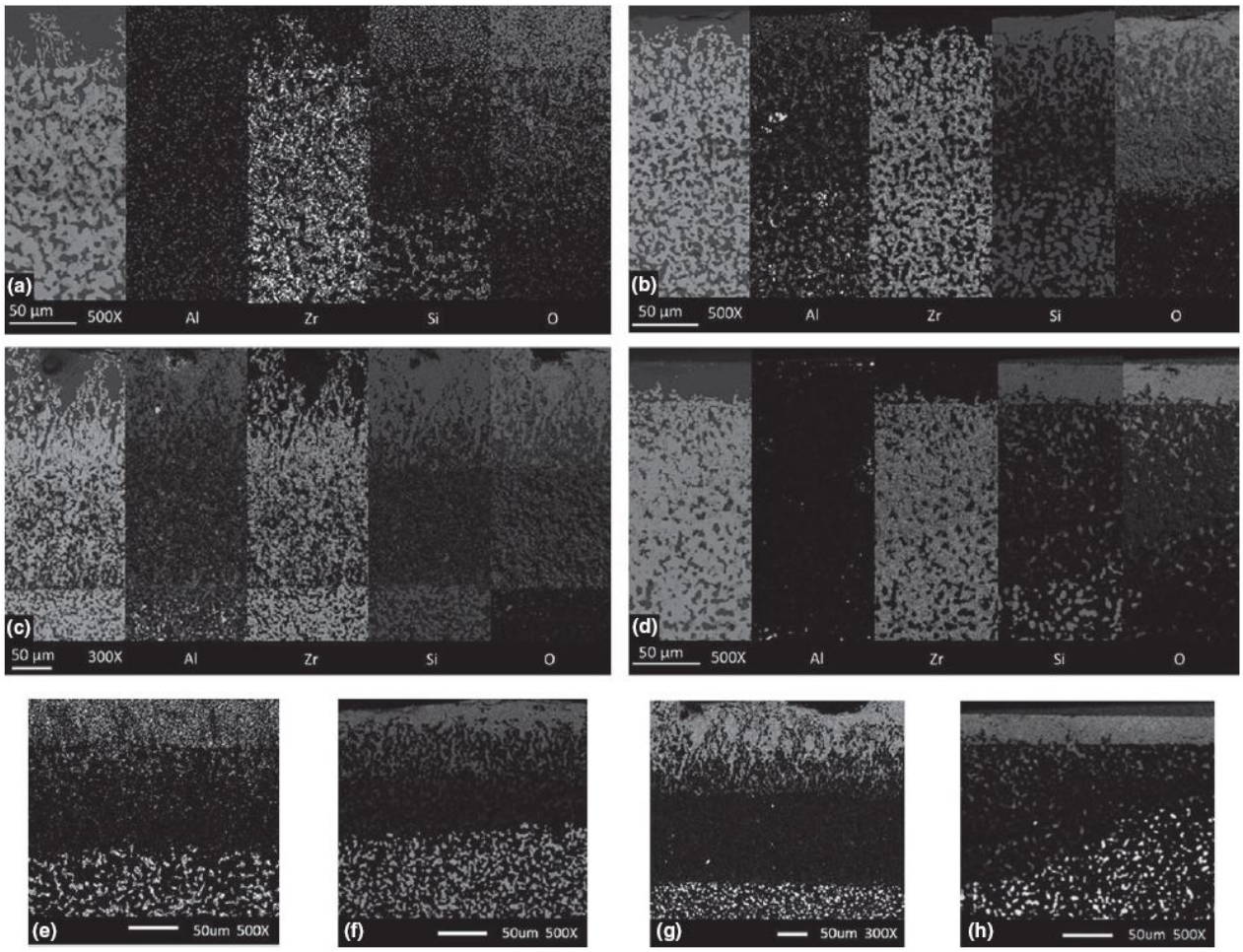

Figure 15: EDS maps of corresponding elements for four 5-h oxidized coupons. (a) ZS73, (b) ZSA631, (c) ZSA721, and (d) ZS82; Their corresponding Si maps are shown in e, f, g, and h.

DISTRIBUTION A: Distribution approved for public release.

It can be seen from the composition maps in figure 15 that the various layers in ZSA631, ZS73 and ZSA721 are rather regular and relatively planar, whereas ZS82 shows significant irregularities, which is in agreement with the results reported by Williams et. al.[15]. The Si map shown in figure 15(h) shows this irregularities clearly, especially in case of the Si depleted region. The oxidation behavior in this composite is therefore expected to be relatively stochastic. The microstructures show the presence of an intermediate layer of oxide underneath the silica scale for ZS73, ZSA631 and ZS721. The elemental distributions mapped using EDS indicate the presence of Zr, Si and O, while the backscattered images suggest the presence of two phases. Hence, presumably, this layer is comprised of ZrO_2 + SiO_2, which would be in accordance with the results reported in the literature. [16,17] The layer underneath this mixed oxide scale exhibits significant silicon depletion. This Si depleted region forms the final layer of the oxygen affected area. The mechanism of silicon depletion has been discussed elsewhere [17]. While all these three compositions show an intermediate layer of ZrO_2 + SiO_2 of comparable thickness, they exhibit significant differences in the top layer and the subscale region. ZSA631 (Figure 4b) has the thinnest top layer of ~ 30±10 μm, while ZSA721 (Figure 4c) has the thickest silica layer, ~ 120±10 μm. ZS73 has a silica top layer thickness of ~ 50±5 μm. The thickness of the silica scale in ZS82 shows a significant variation, but the relatively uniform regions of the scale are comparable to ZSA631, showing a thickness of 35±10 μm. The subscale region is comparable for ZS73 and ZSA631, with the latter having a marginally thinner subscale (65 μm vis-à-vis 50 μm). However, ZSA721 shows a very thick silicon depleted subscale, ~ 150 μm. The ZS82 sample also exhibited the layered structure. The presence of SiO_2 in the SiO_2 + ZrO_2 layer is quite low that the layer boundary not easily recognizable to eye. In this case, there is a significant variation in the Si depleted region ranging from 80–150μm. Based on the microstructure and EDS analysis, the net oxygen affected region for ZS73, ZSA631, ZSA721 and ZS82 were 160 μm, 130 μm, 300 μm and 110– 180μm respectively.

Urbain *et. al.* reported the viscosities in the Al_2O_3-SiO_2 system over a range of compositions and temperatures [18]. They showed that as the Al_2O_3 content increased, the viscosity of the Al_2O_3-SiO_2 system decreased at 1600°C. The presence of Al_2O_3 from the oxidation of AlN in ZSA631 is therefore likely to

DISTRIBUTION A: Distribution approved for public release.

lower the viscosity of the oxide scale in comparison to the ZS73 sample and hence result in a continuous surface coverage. This, in fact, is reflected in the cross-section micrographs (Figure 14a and 14b for ZS73 and ZSA631 respectively), where it can be clearly seen that the top layer in oxidized ZS73 has a higher ZrO_2 content compared to ZSA631, which would have formed before complete scale coverage was obtained. The presence of ZrO_2 is not detected primarily because the depth probed by XPS is typically of the order of tens of nanometers, whereas the ZrO_2 islands in the micrographs show up at a depth of few microns. As expected, given the similar AlN content, the XPS spectra from the oxidized ZSA721 showed a similar surface Al content. However, a greater volume fraction of ZrB_2 leads to greater availability of Zr to form ZrO_2, in comparison to ZSA631. The permeable ZrO_2, once formed in significantly larger quantities, compared to ZSA631, provides oxygen pathway deeper into the material, which accounts for the difference in oxidation resistance between these two composites [14].

3.5 Effect of AlN content on the microstructure of the surface oxide

The oxidation behavior of ZrB_2-SiC composites, with varying amounts of AlN substituting for ZrB_2, was studied under steady ambient air atmosphere at 1600°C for up to one hour. Small amounts of AlN substitutions (≤ 10 vol%) were found to result in marginally improved oxidation resistance, whereas larger amounts resulted in a deterioration in the oxidation resistance. The size of ZrO_2 clusters on the oxidized surface was found to be a function of the AlN content. This effect was more pronounced after longer oxidation times (~ 1 hour) as opposed to shorter durations (~ 5 minutes). The coarsening of the surface ZrO_2 grains was attributed to Ostwald ripening. It was postulated that presence of AlN results in the formation of Al_2O_3 during the oxidation process, subsequently resulting in a lowering of viscosity of the glassy silica scale and increasing oxygen permeation through the scale which adversely affects the oxidation resistance of the high AlN containing composites.

Figure 16 shows the surface of the oxidized samples after 1 hour of isothermal oxidation. It can be seen that as the AlN content increases, the ZrO_2 features in the scale grow coarser. The addition to 5

DISTRIBUTION A: Distribution approved for public release.

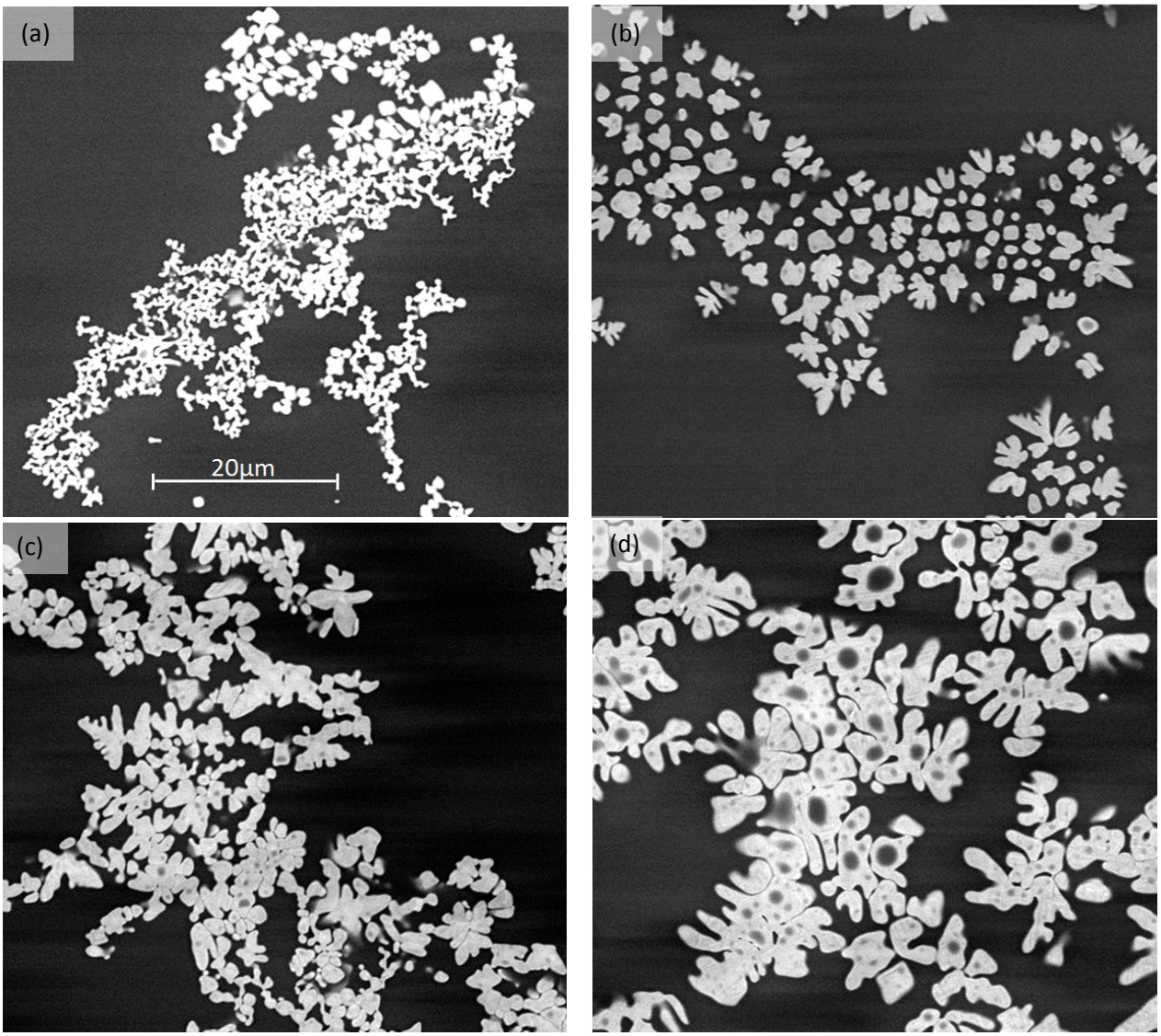

Figure 16: ZrO_2 features on the surface oxide scale after 1 hour of oxidation at 1600°C. (a) $ZrB_2$30SiC, (b) ZrB_2-30SiC-5AlN, (c) ZrB_2-30SiC-10AlN and (d) ZrB_2-30SiC-15AlN.

vol% AlN resulted in a significant coarsening in comparison to the unmodified sample. Increasing the AlN content to 15 vol% caused further coarsening, with ZrO_2 assuming a dendritic morphology. The formation of dendritic ZrO_2 features during oxidation has been previously reported by Karlsdottir and Halloran[19,20]. We postulate that the coarsening of ZrO_2 occurs via the Ostwald ripening mechanism[21]. Addition of Al_2O_3 to SiO_2 melts has been known to result in a reduction in viscosity[18]. A reduction in viscosity will result in enhanced diffusivity according to the Stokes-Einstein equation –

$$D = \frac{kT}{6\pi\eta r} \tag{1}$$

DISTRIBUTION A: Distribution approved for public release.

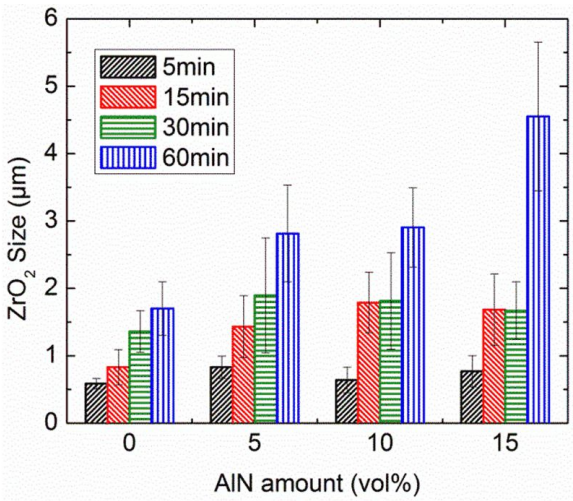

Figure 17: Variation of ZrO_2 crystallite size with time and composition at 1600°C

where D denotes the diffusivity, η denotes the fluid viscosity, k is the Boltzmann constant, T is the absolute temperature and r is the radius of the molecules.

Diffusion controlled Ostwald ripening is governed by the Lifshitz-Slyozov-Wagner (LSW) theory according to the equation –

$$\langle R \rangle^3 - \langle R_0 \rangle^3 = \frac{8\gamma c_\infty v^2 D}{9kT} t \qquad (2)$$

Where $\langle R \rangle$ is average particle size at a time t, $\langle R_0 \rangle$ is the initial particle size, D is the diffusion constant, c_∞ is solubility of the particle in the liquid, γ is the specific surface energy, v is the atomic volume, k is Boltzmann constant, and T is absolute temperature. Karlsdottir and Halloran have reported that ZrO_2 dissolves in liquid B_2O_3 during the oxidation of ZrB_2-SiC composites, and the initial liquid that forms is a ZrO_2-SiO_2-B_2O_3 ternary liquid[19,20]. With the evaporation of B_2O_3, the composition of the ternary liquid shifts to the SiO_2 rich compositions, in which ZrO_2 is not soluble, and hence re-precipitates, facilitating the Ostwald ripening process. Figure 17 shows the variation in the size of the surface ZrO_2 features as a function of time and composition at 1600°C. It can be seen that the particle size increases with time for all four compositions studied. The rate of increase (difference in initial and final size over time) also accelerates with increasing AlN content.

At temperatures as high as 1600°C, it is expected that B_2O_3 will evaporate rapidly from the surface oxide scale. In fact, Shugart et.al. reported a rapid decrease in the B_2O_3 content at the surface of the oxide scale following oxidation at 1500°C, although the boron content increased deeper into the scale[22]. Figure 18(a) shows the vapor pressure of B_2O_3 as a function of temperature. The vapor pressure diagram is based on the thermodynamic data available in the NIST-JANAF tables[23]. The vapor pressure exceeds 1 atmosphere at ~ 1150°C, and B_2O_3 starts to evaporate. The rate of increase in vapor pressure

DISTRIBUTION A: Distribution approved for public release.

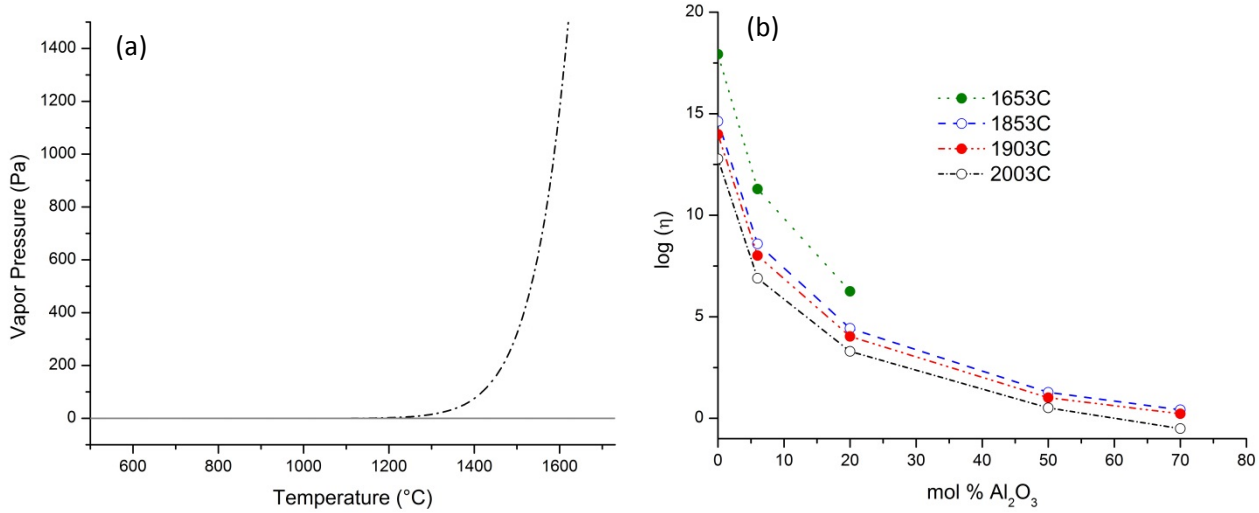

Figure 18: (a) Vapor pressure of B_2O_3 as a function of temperature and (b) viscosity of SiO_2-Al_2O_3 melt

accelerates with temperature, and the vapor pressure is doubled going from 1500 to 1600°C . Therefore, it is expected that the retained B_2O_3 after an hour of oxidation at 1600°C will be significantly lower in comparison to the work done by Shugart et.al. at 1500°C. As a first approximation, we can get a qualitative understanding of the viscosity of the oxide scale by considering the viscosities of SiO_2-Al_2O_3 melts. Interestingly, the Al_2O_3-ZrO_2 phase diagram shows the presence of a eutectic at ~ 42 mol% ZrO_2, with a eutectic temperature of ~ 1700°C[24]. Figure 18(b) shows the variation of viscosity with Al_2O_3 content in SiO_2 at four different temperatures. This plot is based on the experimental data reported by Urbain et.al.[18]. It should be noted that the viscosities of pure SiO_2 at 1853, 1953 and 2003 °C have been calculated from the silica data at different temperatures assuming an Arrhenius relationship. This assumption appears to be valid since Urbain et.al. demonstrated a linear relation between the logarithm of viscosity and 1/T. It can be seen that at all temperatures, a similar trend can be observed in the reduction of viscosity with Al_2O_3 additions in silicate melts. Initially, small Al_2O_3 content results in a sharp decrease in viscosity. However, the rate of viscosity reduction decreases with higher Al_2O_3 content. Oxidation of AlN is expected to lead to the formation of Al_2O_3, whose presence in the SiO_2 scale will affect the viscosity, and hence its ability to seal the surface of the coupon. The reduction in viscosity by AlN (and hence Al_2O_3) additions would imply enhanced mobility of ZrO_2 in the glassy scale, which facilitates an Ostwald ripening process in the oxide scale. The viscosity of B_2O_3-Al_2O_3 melts reported by Riebling[25]

DISTRIBUTION A: Distribution approved for public release.

also indicates a reduction in viscosity with increasing Al_2O_3 content. We are not aware of any reports on the viscosity variation in the ternary Al_2O_3-SiO_2-B_2O_3 melts (without alkali metal oxide additions), but it is reasonable to assume that the viscosity is expected to decrease with higher Al_2O_3 content since Al_2O_3 additions to both B_2O_3 and SiO_2 result in a reduction in viscosity of the binary systems, which in turn is likely to result in enhanced mobility of ZrO_2 particles in the scale.

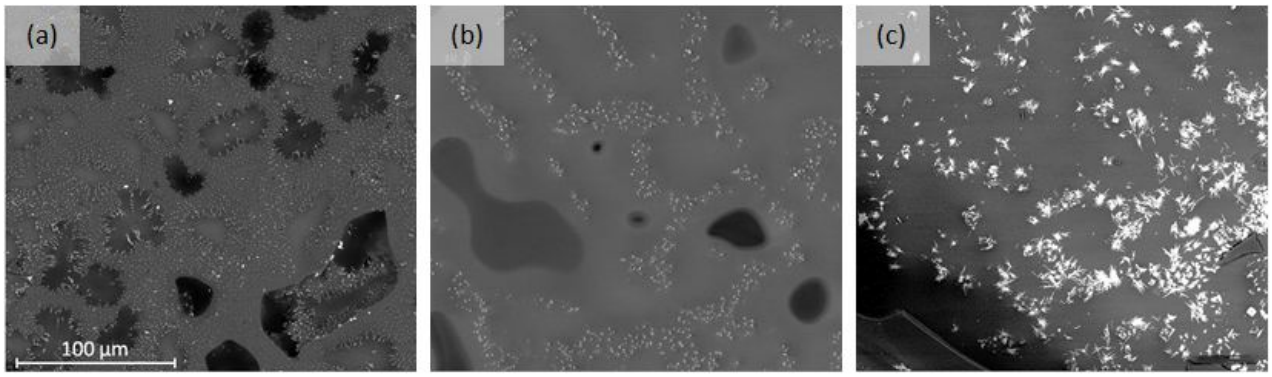

Figure 19: Surface oxide on ZrB_2-30SiC after (a) 5 minutes, (b) 15 minutes and (c) 60 minutes of oxidation at 1600°C

Figure 19 shows the surface micrographs after 5 minutes of oxidation for the ZrB_2-30SiC sample at three different temperatures (1400, 1500 and 1600°C). ZrO_2 fingers growing outwards, surrounded by a small region with darker contrast can be seen clearly after 5 minutes of oxidation at 1600°C, in figure 6(c). These elongated fingers are not quite as prominent at 1500°C (figure 19(b)), and hardly distinguishable at 1400°C (figure 19(a)). The mass transport of ZrO_2 to the surface was studied by Karlsdottir and Halloran and explained using a convection cell theory[19,20,26,27]. They observed "island-in-lagoon" patterns on the surface of ZrB_2-15SiC samples after oxidation at 1550°C for 2 hours[27], somewhat similar to the patterns we observed in the ZrB_2-30SiC samples at 1600°C, albeit at much shorter time intervals. In their work, bright ZrO_2 rich regions could be seen (islands) in SiO_2 rich regions, with dark petals of B_2O_3 being observed in the immediate vicinity of ZrO_2. In this study, after 5 minutes of oxidation at 1600°C, shown in figure 19(c), we observed ZrO_2 fingers (instead of islands) surrounded by regions of dark contrast (presumably B_2O_3) in a SiO_2 matrix. Relatively smaller amounts of ZrB_2 results in a lower fraction of ZrO_2 in comparison to Karlsdottir and Halloran's work[27], which coupled with short

DISTRIBUTION A: Distribution approved for public release.

time intervals, explains the presence of isolated fingers rather than larger islands. With subsequent coarsening, larger ZrO_2 clusters, or islands can be seen, for instance, in figure 19(c), although the B_2O_3 petals were not clearly evident. The absence of B_2O_3 petals can be attributed to faster evaporation of B_2O_3 at 1600°C in comparison to 1550°C (vapor pressure changes to ~ 1200 Pa at 1600°C from ~ 350 Pa at 1550°C). Additionally, lower ZrB_2 content results in smaller amounts of B_2O_3 formation during the oxidation process. In fact, Karlsdottir and Halloran indicated that the convection cell mechanism become less and less apparent with a reduction in boron content[19]. B_2O_3 content is relatively high when it forms deeper in the scale, but gradually reduces towards the surface of the scale. The loss of boria in the scale caused large viscosity difference between the freshly formed ZrO_2-SiO_2-B_2O_3 liquid in the subsurface and the viscous surface[27] which in turn creates the convection cell. Due to large volume increase upon oxidation (380%), this fresh borosilicate liquid is squeezed up away from the interface to the surface through convention cells. After upwelling on the surface, the borosilicate liquid flows radially from the center ZrO_2 column and resulting in the SiO_2 rich surface. ZrO_2 is transported to the surface by solution-precipitation mechanism in the borosilicate liquid[26], which is consistent with the mechanism of Ostwald ripening of solute particles in liquids[28].

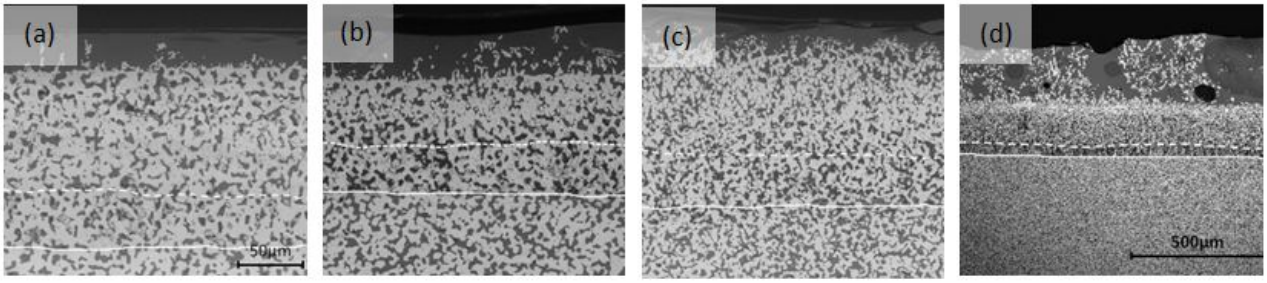

Figure 20: Cross-section of the oxidized coupons after 5 hours of oxidation at 1600°C. (a) $ZrB_2$30SiC, (b) ZrB_2-30SiC-5AlN, (c) ZrB_2-30SiC-10AlN and (d) ZrB_2-30SiC-15AlN.

Figure 20 shows the cross section images of all four compositions after 5 hours of oxidation at 1600°C. The oxide scale, including the SiO_2 rich top layer, ZrO_2 inter layer and the Si depleted region, is comparable in figures 20(a-c) and is consistent with the literature on ZrB_2-SiC composites[19,29-31]. However, the oxide scale is significantly thicker in figure 20(d) for the 15 vol% AlN containing

DISTRIBUTION A: Distribution approved for public release.

composite. The scale thickens at a much faster rate with 15 vol% AlN addition, and hence micrograph for this sample (figure 20(d)) was taken at a lower magnification to show the whole thickness of the oxide scale. The oxide scale for the 15 vol% AlN composition is significantly thicker (~ 440 μm) compared to the scale on ZrB_2-30 vol% SiC composite (170 μm). The scale thicknesses in the 5 and 10 vol% AlN were found to be approximately 130 and 140μm respectively. Clearly, higher levels of AlN do not provide adequate oxidation protection at elevated temperatures. The composites studied by Brach et.al.[32] had even higher AlN content (~ 55 vol%) and failed at even lower temperatures (~ 1300°C). However, the failure mode in their study was different, involving rupturing of the external scale, due to the formation of aluminoborates, which was not observed in the present study due to the relatively lower Al_2O_3 content.

In summary, low AlN substitutions (5%, 10%) for ZrB_2 resulted in enhanced oxidation resistance with thinner scales. High AlN substitutions (i.e. , 15%) resulted in severe oxidation with excessive ZrO_2 dissolved in the oxide scale and formed a thick scale. The altering of the oxidation performance can be ascribed to the viscosity reduction in the oxide scale due to the presence of Al_2O_3 formed as a result of AlN oxidation. The coarsening of ZrO_2 particles formed during the initial stages of oxidation further indicated the reduced viscosity and enhanced mass transport with increasing AlN additions. A lower viscosity scale can provide better surface coverage, but at the same time allows for rapid oxygen permeation. The rate of oxygen diffusion through the silica scale is governed by temperature, and hence the optimal viscosity of the oxide scale is likely to be a function of the temperature. Basically, the optimal viscosity (and hence the composition) is dictated by the need for adequate surface coverage, and slow oxygen transport through the scale.

3.6 Oxidation behavior of ZrB_2-SiC-AlN at 2000°C in low O_2 pressures

ZrB_2-SiC-AlN ceramics with varying amounts of SiC and AlN have been tested in our plasma spray facility at approximately 2000°C at 100 torr pressure using compressed air. The temperature profile measured using a two-color optical pyrometer is shown in figure 21. High ZrB_2 containing samples

DISTRIBUTION A: Distribution approved for public release.

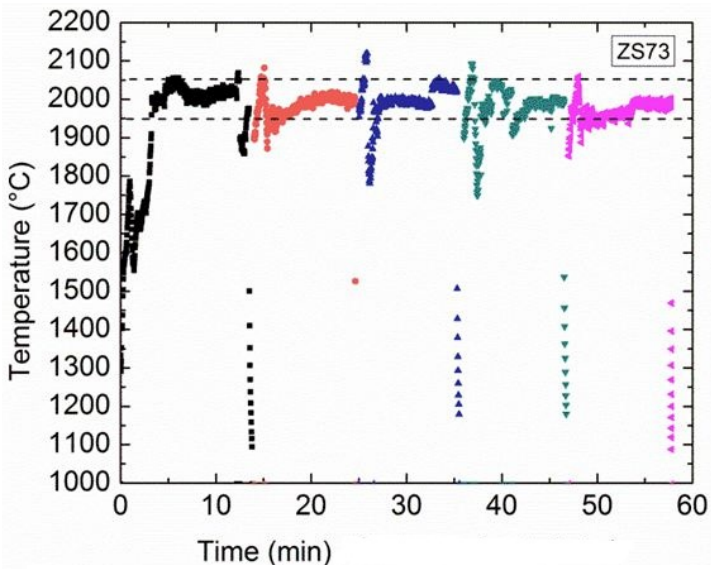

Figure 21. Temperature profile recorded for ZS73 sample for the cyclic test.

(ZrB_2-20vol%SiC) experienced oxide detachment during multiple cycles while low ZrB_2 composites (ZrB_2-30vol%SiC, ZrB_2-30vol%SiC-10vol%AlN) suffered from severe oxidation and structural damage. SiC in itself was not sufficient to provide oxidation resistance due to active oxidation and mechanical scouring at this test condition. Addition of AlN while maintaining an adequate amount of ZrB_2 and SiC was essential for alleviating the thermal shock damage and improving the oxidation resistance.

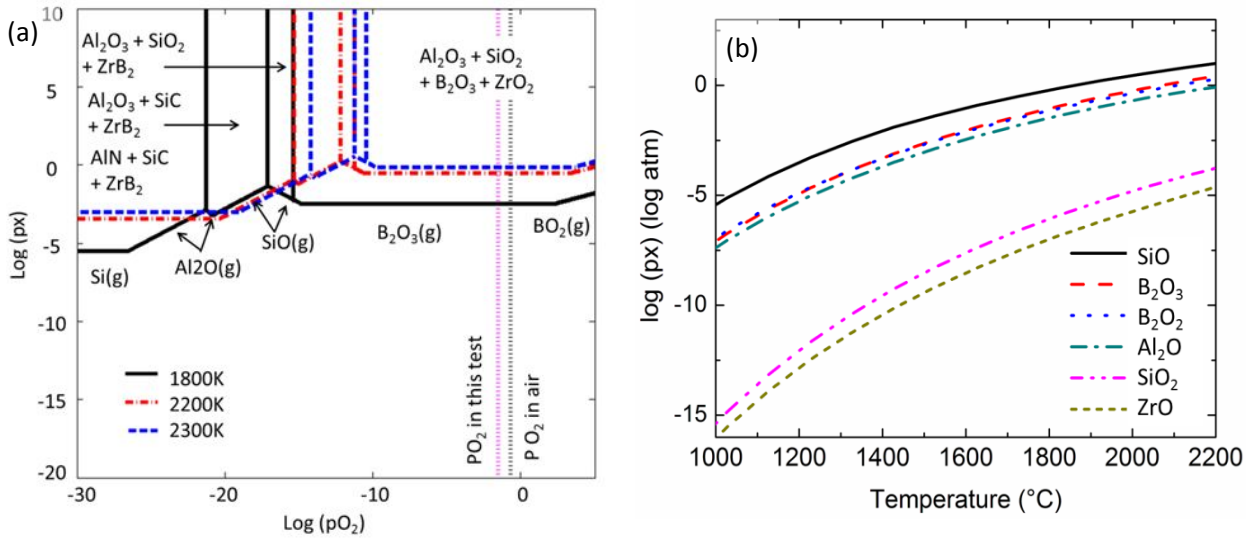

Figure 22: (a) ZrB_2-SiC-AlN volatility diagram and (b) vapor pressure of relevant oxide species as a function of temperature

The volatility diagram was constructed by considering all possible boron, silicon and aluminum vapor species while carbon and nitrogen species were ignored. The relevant chemical reactions for boron, silicon were taken from available literature [15,17]. The thermodynamic data and equilibrium constants were taken from the NIST-JANAF tables [33]. The volatility diagram in figure 22 covers the species with the highest vapor pressure at each P_{O2}.

DISTRIBUTION A: Distribution approved for public release.

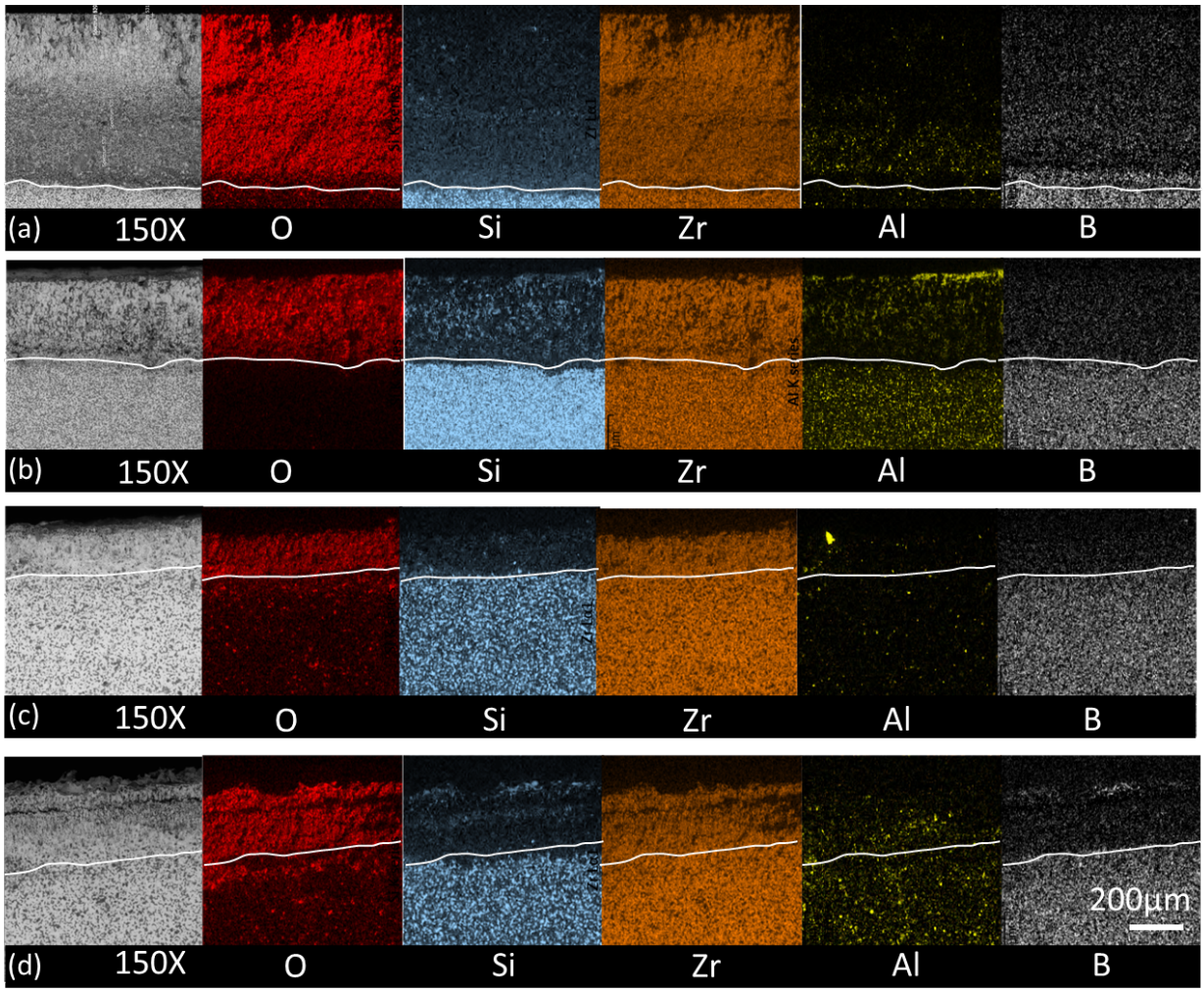

Figure 23. Cross-section SEM and EDS maps of 10 minute tested samples. (a) ZS73, (b) ZSA631, (c) ZS82, (d) ZSA721. The first column on the left shows the back scattered images. The elements mapped in EDS maps are indicated below the EDS maps.

The species that have lower vapor pressure are not plotted for simplicity. The vapor pressures estimated for various Si and B species are in agreement with the values reported in the literature by other researchers [15,17,34]. The volatility diagram indicates that the significant vapor species in this system are B_2O_3, SiO and Al_2O. A separate graph of vapor pressure containing these species as a function of temperature is calculated and plotted. B_2O_2 is also considered since it has comparable vapor pressure to B_2O_3 at the ZrB_2-ZrO_2 interface and has higher vapor pressure than B_2O_3 at lower oxygen partial pressure regime. ZrO is the most dominant vapor species among Zr species, so it is plotted on the diagram. SiO_2 is also considered due to its high vapor pressure at high oxygen partial pressures. The vapor pressures of B_2O_3, SiO_2 are in equilibrium with their corresponding liquid and independent of P_{O2}. Since SiO has the

DISTRIBUTION A: Distribution approved for public release.

highest vapor pressure at Si-SiO_2 interface [34], P_{O2} at this interface was used. Similar approach was used for ZrO, Al_2O and B_2O_2 to determine the P_{O2} needed.The cross-section SEM and corresponding EDS maps after a single cycle of 10 minutes at ~ 2000°C are shown in figure 23. In all the samples, the scale primarily consists of ZrO_2. In ZS73, Si is completed depleted in the oxide layer. Some Si remained in ZS82 and ZSA721 samples oxides. ZSA631 showed the highest amount of Si in the oxide scale.

Elemental distribution of Al has been shown in figure 23b (ZSA631) and 23d (ZSA721). ZSA631 sample showed an Al rich top layer. The thermodynamically stable oxides of ZrB_2-SiC-AlN system are Al_2O_3, SiO_2, B_2O_3 and ZrO_2. Destabilization of the stable oxides is possible only at extremely low oxygen pressures. For instance, the destabilizing these oxides at 2300K requires an oxygen pressure under 10^{-10} atm. However, the stability of the oxides also depends on their relevant vapor species. During the experiment, a green fluorescence was observed at the initial stage of the plasma exposure but diminished after a few minutes. This green fluorescence emission corresponds to volatilization of the boron species[35]. This was further confirmed by EDS map (figure 23), with boron being largely absent on the surface. SiO_2 has a low enough vapor pressure that it is not likely to vaporize as SiO_2 (g). However, SiO_2 is susceptible to active oxidation [36], and this reaction is accompanied by a decrease in mass. The high vapor pressure of SiO is likely to result in large depletion of Si species at high temperatures. The highest vapor pressure in Al species is more than one order of magnitude lower than Si species. Therefore, it is expected that Al should be less prone to depletion in comparison to Si. ZrO_2 is not likely to vaporize from the surface, since its vapor ZrO reached only $10^{-5.58}$ atm at 2300K. Therefore, the overall surface oxides thermodynamically favorable would be ZrO_2 and possibly some SiO_2 and Al_2O_3. Not surprisingly, both ZrO_2 and SiO_2 were observed in the XRD pattern and SEM micrographs (with the exception of ZS73, which showed the presence of ZrO_2 only). Al_2O_3 was not observed at the oxidized surface for any of the samples investigated. The absence of SiO_2 in the diffraction pattern of ZS73 is consistent with the surface micrographs of ZS73 (figure 23a), which shows a preponderance of ZrO_2 clusters, but no visible SiO_2 glassy outer scale. The EDS map (figure 23a) suggests a large oxygen affected region, and indicates the presence of SiO_2 at depths below 300μm from the surface, and hence can't be detected by x-rays. ZS82

DISTRIBUTION A: Distribution approved for public release.

(figure 23c), on the other hand, has a much thinner scale, as a result of which the SiO_2 is close enough to the surface and is observed in correspoonding XRD pattern. ZSA631 and ZSA721 (figure 23b and d respectively) show the presence of the oxides of Si and Al at the surface. In the case of Al species, the possibility of forming volatile Al_2O needs to be considered. At the testing temperature (~2300K), with Al_2O_3 vapor pressure being close to 10^{-3} atm [37], the oxygen partial pressure needed for formation of Al_2O is less than $10^{-11.8}$ atm. The oxygen partial pressure at ZrB_2-ZrO_2 interface at 2300K based on figure 3 is $10^{-10.43}$ atm. Hence, thermodynamically Al_2O_3 would form instead of Al_2O (the formation of some Al_2O can is also possible due to uncertainties in temperature and other variables). Consequently, Al, Si species were retained in the sample of ZSA721 and ZSA631.

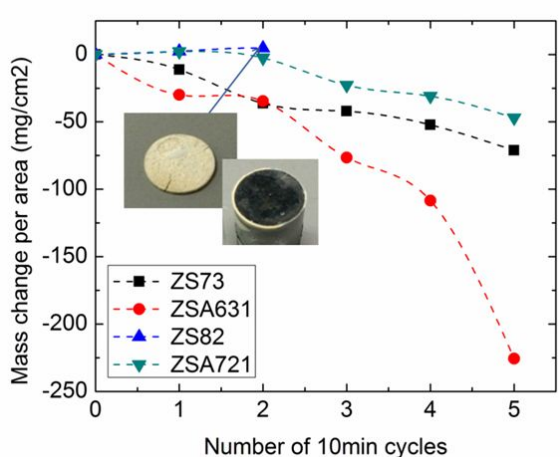

Figure 24. Mass change data and sample photos after each cycle of ten minutes cyclic tests. The insert shows the ZS82 after two test cycles.

The specific mass change (figure 24) revealed a net mass loss after cyclic tests for all compositions. The mass change was accompanied by oxide scale spallation, with the oxide layer spalling completely in ZS82 (figure 24, inset), possibly as a result of thermal shock and high stresses due to the subsonic plasma stream. Since, the entire oxide scale of ZS82 spalled off after the second cycle, the sample was not subjected to further cycling. Other samples showed varying degrees of oxide scale spallation, although none of them showed a complete spallation of the scale as observed in ZS82.

Figure 25 shows the cross-section micrographs at the end of cyclic tests (cross-section micrographs pertaining to ZS82 were recorded after 2 cycles). Figure 25a shows the cross-section of the face exposed to plasma heating and oxygen of ZS73 sample. It can be seen that the scale has spalled off in some region, while it remains intact in other regions. More importantly, an interfacial zone is observed in the sub-surface, underneath the regions from where the scale has spalled off. The cross-section microstructure of ZSA631 (figure 25b) differs significantly from that of ZS73. The outer layers of the

DISTRIBUTION A: Distribution approved for public release.

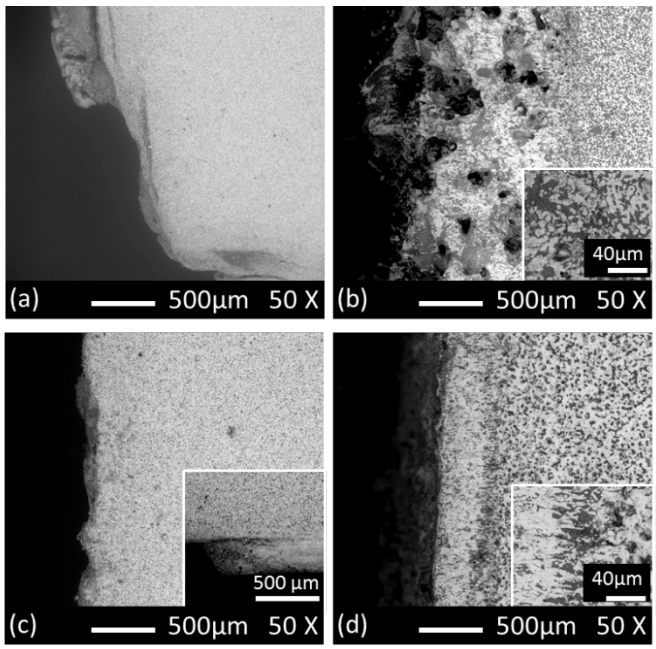

Figure 25. Cross-section micrographs of samples a. ZS73, b. ZSA631, c. ZS82, d. ZSA721 after cyclic tests (cross-section micrographs pertaining to ZS82 were recorded after 2 cycles).

scale are significantly more porous. The inset shows a higher magnification image of the interfacial region between the external oxide scale and the base alloy. EDS analyses in this region confirmed that presence of Al rich SiO_2 (dark contrast) along with ZrO_2 (bright contrast). ZSA631 showed the maximum mass change (and recession) during testing, with the sample being progressively ablated. Unlike the ZS73 sample, the external scale was not comprised exclusively of zirconia, with a fair amount of SiO_2 being present as well. Figure 25c shows the cross-section of the ZS82 sample after 2 cycles. It can be seen that the external ZrO_2 layer is completely missing. The inset shows the side face of the sample (not directly exposed to the plasma stream during testing). Clearly, the scale spalled off from the exposed face, and from a small region on the side of the sample. The scale was still present in the regions exposed to relatively lower temperature, and the scale sub-surface showed a degree of similarity with ZS73, albeit the volume fraction of ZrO_2 is considerably higher, and the SiO_2 considerably lower in comparison to ZS73. This is possibly due to the higher Zr content of the pristine alloy in ZS82 as opposed to ZS73. Figure 10d shows the cross-section microstructure of ZSA721. This sample did not show any obvious scale spallation, but the external ZrO_2 region was interspersed with SiO_2 with Al containing species. The inset shows a high magnification image of the interfacial region between the base alloy and the oxide scale. EDS analyses revealed the interfacial chemistry to be a combination of silicon, aluminum, and oxygen possible a mixture of largely SiO_2 and a small amount of Al_2O_3.

DISTRIBUTION A: Distribution approved for public release.

3.7 Oxidation of Coated UHTCs: collaboration with Univ. of Wisconsin Madison

The Mo-W-Si-B alloys were prepared at Iowa State University and shipped to University of Wisconsin, Madison for application of the Mo-Si-B coatings. The samples received from University of Wisconsin Madison were tested under oxidative conditions at Iowa State University. Figure 26(a) shows

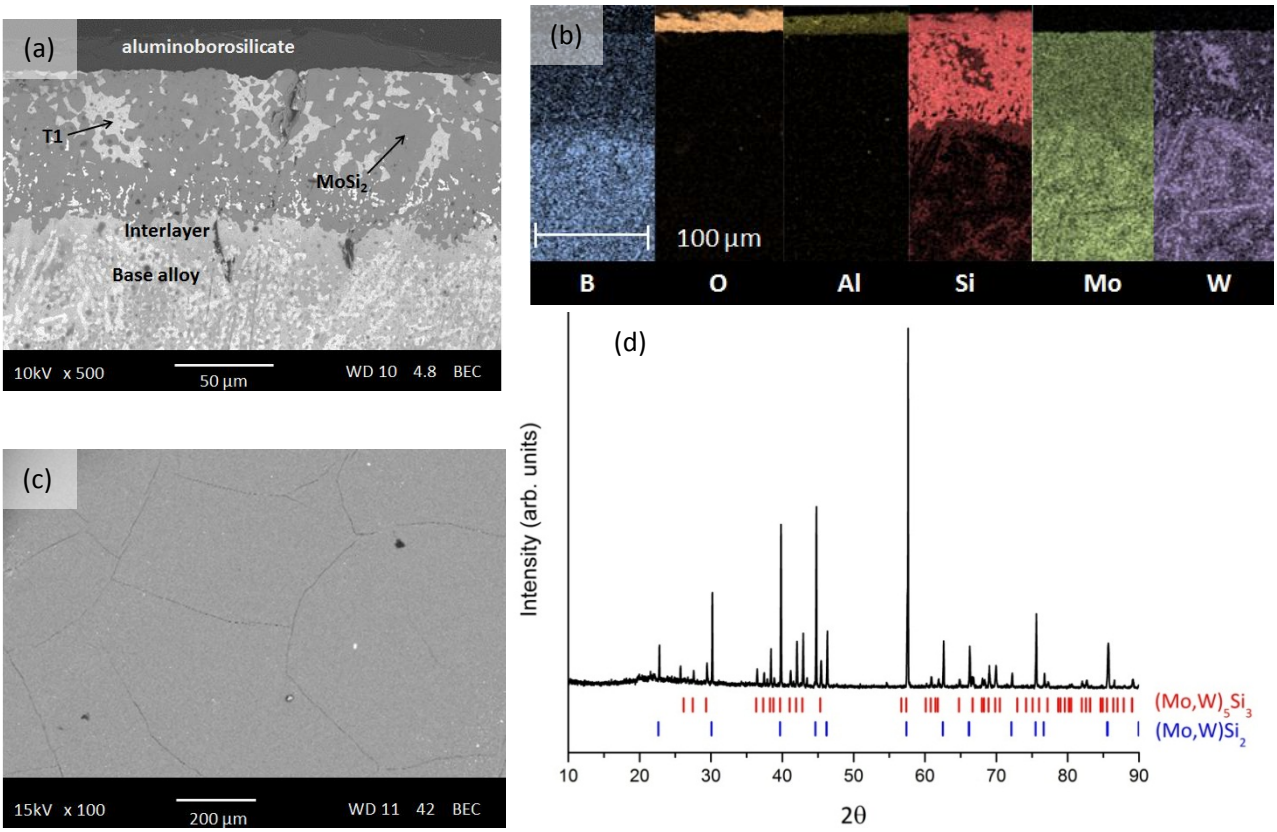

Figure 26: (a) Cross-section microstructures of the coated alloy; (b) EDS elemental map of the coated alloy – each slice represents the distribution of a given element from the same region of the microstructure; (c) Surface micrograph of the coated alloy; (d) X-Ray diffractogram from the coated surface.

the cross-section microstructure of the coated Mo-W-Si-B alloy. The microstructure comprises of four major regions – a thin oxide layer at the top, followed by the Mo-Si-B coating, an interlayer between the coating and the base alloy, and the base alloy itself. Figure 26(b) shows the EDS elemental map collected from the corresponding region. The elemental map shows the presence of Aluminum, Silicon, Oxygen and a small amount of Boron in the top layer, indicating this to be the aluminoborosilicate layer. The second layer is the Mo-Si-B coating, comprised of $(Mo,W)Si_2$, (Mo,W)B and T1 $(Mo,W)_5Si_3$. The presence of the $(Mo,W)Si_2$ is in agreement with the results reported by Lu-Steffes et.al.[10] following the

DISTRIBUTION A: Distribution approved for public release.

pack cementation of pure W with Mo-Si-B. Underneath the coating, a T1 $(Mo,W)_5Si_3$ interlayer was observed to form as well. The tungsten content in the base alloy seems to be higher in comparison to the coating since the interdiffusion between Mo and W is extremely sluggish[38]. Figure 26(c) shows the surface microstructure of the coated alloys. In general, it can be seen that the coating provides an excellent surface coverage. However, minor cracks could still be observed. Figure 26(d) shows the x-ray diffraction pattern collected from the coating surface. It can be seen clearly that the major phases visible are the c11b $(Mo,W)Si_2$ and the T1 $(Mo,W)_5Si_3$. This is in complete agreement with the SEM micrographs and EDS analyses presented in figure 26(a) and (b).

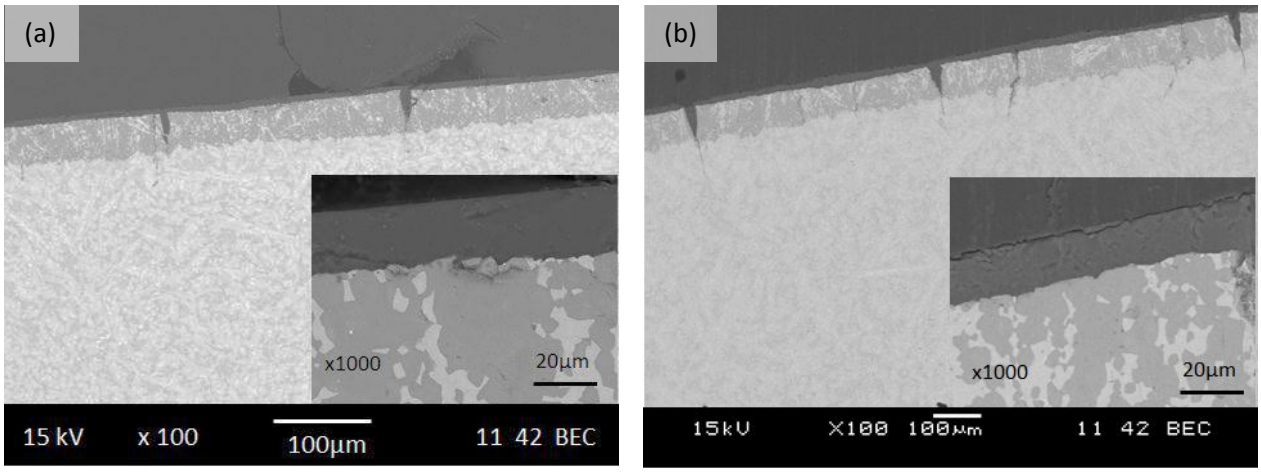

Figure 27: Cross-section micrographs of the coated alloy after oxidation at (a) 1000° and (b) 1300°C

Figure 27(a) and (b) shows the cross-section microstructures of the coated alloys at 1000°C and 1300°C for 25 hours and 5 hours respectively. It can be seen that there is very little change in the oxide scale as opposed to the un-oxidized sample. The aluminoborosilicate scale formed during the pre-treatment of the coating provides an excellent oxygen barrier. The absence of MoO_2 or WO_2 further indicates the efficacy of the Mo-Si-B coating. The coating, however, does indicate the presence of a number of cracks. The insets in figure 27(a) and (b) show high magnification SEM micrographs of the cracked region. It can be seen that this region comprises of the glassy oxide scale. If these cracks are limited to the coatings, then the self-healing nature of the coating serves to "heal" these cracks, thereby

DISTRIBUTION A: Distribution approved for public release.

protecting the underlying base alloy from oxidation. Oxidation behavior of the coated alloys, therefore, compare very favorably to materials like WSi_2 [11] as well as the uncoated alloy.

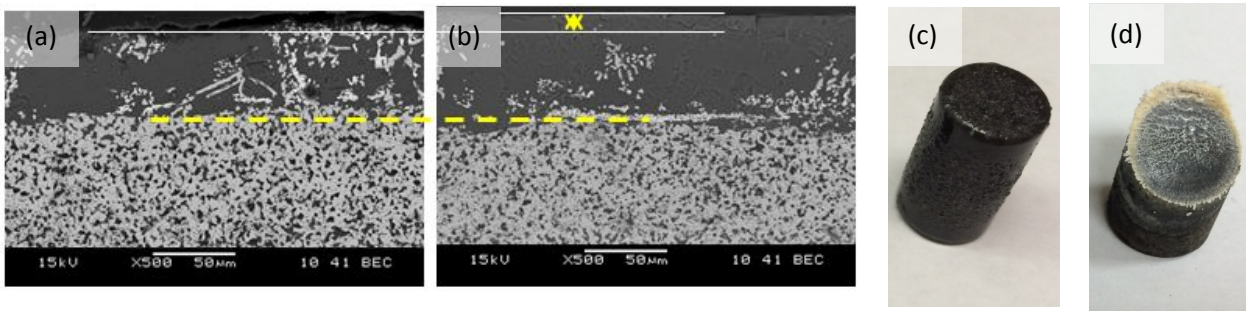

Figure 28. (a) cross-section of the coated ZS73 composites prior to oxidation (b) post-oxidation cross-section, (c) coated ZrB_2-SiC-AlN sample prior to plasma heating tests and (d) post-test sample showing complete ablation of the coating, after oxidation at 2000°C or 10 minutes

ZrB_2-SiC based composites coated with Mo-Si-B, from University of Wisconsin, Madison, were oxidized at 1600°C for 5 hours. Figure 28 shows the cross-section micrographs of the coated alloys before and after oxidation. It can be seen that the coated alloys resulted in very little Si depletion, resulting in improved oxidation resistance. However, as the temperature is increased to ~ 2000°C, the pressure reduced to 100 torr, the coating ablates completely, and afforded to protection whatsoever, as seen from the visual image of the samples before and after testing.

3.8 Oxidation in dissociated air: collaboration with Univ. of Vermont

ZrB_2-SiC-AlN composites, namely ZS73 and 631 were tested using the arc-jet facility at University of Vermont in dissociated air at elevated temperatures. Bulk samples were prepared in the shape of a cone (figure 29), and tested over a range of temperatures (1600 – 1900°C). The oxide scale in ZS73 was eroded completely during the tests, while some surface damage was obser ved in ZSA621 at the highest temperature tested (~ 1900°C). At lower temperatures, ≤ 1800°C, the oxidative damage was negligible. During the initial stages of the test, emissions of BO_x were observed, indicating the loss of boron and its oxides, which is consistent with the available literature. The external scale at 1777°C was seen to be comprised of SiO_2. The external layer was followed by a zone of mixed ZrO_2 and SiO_2 and

DISTRIBUTION A: Distribution approved for public release.

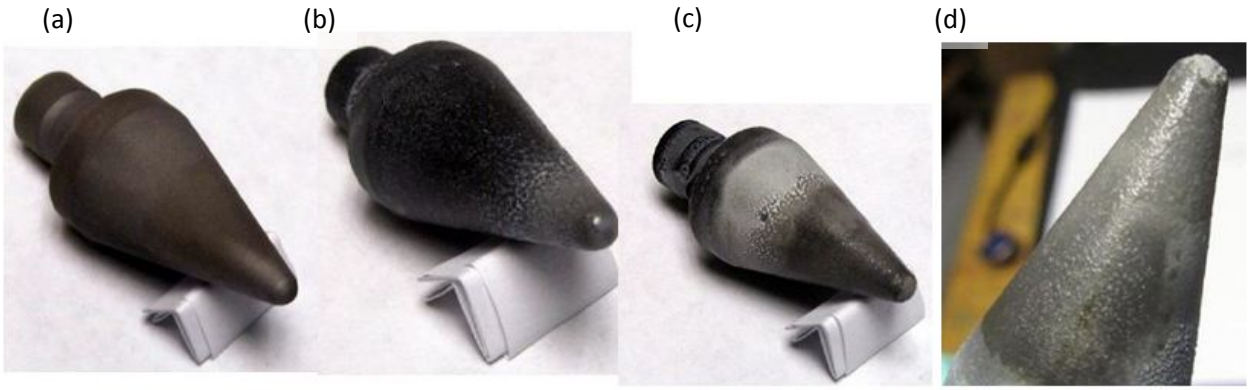

Figure 29: (a) sample before testing, (b) sample after testing at 1777°C, (c) sample after testing at 1877°C and (d) higher magnification image of the nose cone shown in (c).

finally a Si depleted region. It is possible that as the temperature was increased to a regime where active oxidation of SiC occurs, the external scale gets eroded and damaged, since the SiO_2 is unstable under such conditions. Samples were also sent to University of Wisconsin, Madison for application of Mo-Si-B coatings.

DISTRIBUTION A: Distribution approved for public release.

4. Summary

Mo-Si-B alloys comprising of sufficient oxidative stability suffer from inherent brittleness arising due to the presence of the A15 Mo_3Si phase. We demonstrated that this phase can be destabilized by controlled alloying additions with W and Nb. Destabilization of the A15 phase results in the formation of a metal-T1-T2 phase field which is expected to have a greater degree of resilience. The effect of W additions on the oxidation behavior of Mo-Si-B alloys was assessed. It was seen that the oxidation resistance is dependent on chemistry, temperature and microstructure. Higher W content proves beneficial at higher temperatures (≥ 1300°C) in drop-cast alloys, since at these temperatures $(WO_3)_3$ volatilizes leaving behind no impediment for the borosilicate scale to flow and cover the surface. Furthermore, oxidation resistance improves as the microstructural length scales reduce, this finer microstructures require the borosilica scale to flow over smaller lengths in order to cover the surface.

The effect of AlN content on the oxidation behavior of ZrB_2-SiC-AlN was also studied. It was seen that the presence of AlN resulted in the formation of Al_2O_3, which reduces the viscosity of the silica scale. This has a beneficial effect at lower temperatures. As the temperatures increase, the viscosity of silica decreases. This results in faster oxygen dissolution and diffusion through the oxide scale resulting in enhanced oxidation. Therefore, at higher temperatures, a more viscous scale is preferred. Also, the presence of ZrO_2 has a beneficial effect at temperatures ~ 2000°C. The ZrO_2 forms the external scale, and acts as a thermal barrier. It is noteworthy that the thickness of the external scale is comparable to the thicknesses of commercial thermal barrier coatings. Excessively high amounts of ZrO_2 in the scale results in spallation of the external scale with thermal cycling. Lowering the ZrO_2 content and increasing the AlN results in the formation of a subscale at the interface between the external scale and the base alloy comprising on an Al rich silica layer that effectively "pins" the columnar ZrO_2. Such an assembly was found to show greater resilience in an atmosphere comprising of low pressure (100 torr) molecular oxygen at 2000°C.

DISTRIBUTION A: Distribution approved for public release.

5. List of Publications

The following papers were published / are being prepared from the current research supported by AFOSR Grant # FA9550-11-1-201

5.1 Journal publications / articles under preparation

1. P.K. Ray, Y.Y. Ye, M. Akinc and M.J. Kramer, *Effect of Nb and W substitutions on the stability of the A15 Mo_3Si phase,* Journal of Alloys and Compounds 537 (2012) 65 – 70.
2. G. Ouyang, P.K. Ray, M.J. Kramer and M. Akinc, *High Temperature Oxidation of ZrB_2-SiC-AlN Composites at 1600°C*, accepted, Journal of the American Ceramic Society, 2015.
3. G. Ouyang, P.K. Ray, M.J. Kramer and M. Akinc, *Effect of AlN substitutions on the oxidation behavior of ZrB_2-SiC composites at 1600°C*, submitted, Journal of the American Ceramic Society, 2015
4. G. Ouyang, M.F. Besser, P.K. Ray, M.J. Kramer and M. Akinc, *Ultra-High Temperature Cyclic Oxidation tests of ZrB_2-SiC-AlN composites at low oxygen pressure using plasma heating*, under preparation.
5. G. Ouyang, P. Ritt, Pratik K. Ray, M.J. Kramer, J.H. Perepezko and M. Akinc, *Oxidation resistance of a Mo-W-Si-B alloy at 1000 – 1300°C: the effect of a Mo-Si-B multicomponent coating*, under preparation.
6. T. Karahan, G. Ouyang, P.K. Ray, M. Akinc and M.J. Kramer, *Effect of microstructures and W substitution on the transient oxidation behavior of Mo-Si-B alloys at 1100 and 1400°C*, under preparation.
7. T. Karahan, G. Ouyang, P.K. Ray, M. Akinc and M.J. Kramer, *Effect of temperature and W content on the oxidation behavior of Mo-W-Si-B alloys*, under preparation.

DISTRIBUTION A: Distribution approved for public release.

5.2 Conference Presentations

1. M.J. Kramer, G. Ouyang, P.K. Ray, C. Tillson, J.M. Meyers, D.G. Fletcher and M. Akinc, *Ultra-high temperature oxidation of ZrB_2-SiC-AlN composites*, MS&T Fall meeting, 2015, Columbus, OH.
2. G. Ouyang, P.K. Ray, M.J. Kramer and M. Akinc, *Pressureless sintering of a Mo-Si-B alloy with Fe additive*, MS&T Fall meeting, 2014, Pittsburgh, PA.
3. P.K. Ray, Y.Y. Ye, S. Thimmaiah, M.J. Kramer and M. Akinc, *Destabilizing the Mo_3Si phase with W additions and its oxidative stability*, TMS Annual Technical Meeting, 2014, San Diego, CA.
4. P.K. Ray, S. Thimmaiah, Y.Y. Ye, W. Wang, M.J. Kramer and M. Akinc, *Phase stability and microstructures of W substituted Mo-Si-B alloys*, MRS Fall meeting, 2012, Boston, MA.

DISTRIBUTION A: Distribution approved for public release.

6. References

[1] Shi C Zhang, Greg E Hilmas, and William G Fahrenholtz, Journal of the American Ceramic Society **91** (1), 26 (2008).

[2] S. C. Zhang, G. E. Hilmas, and W. G. Fahrenholtz, Journal of the American Ceramic Society **91** (1), 26 (2008).

[3] G. Kresse and J. Furthmüller, Computational Materials Science **6** (1), 15 (1996).

[4] Hendrik J. Monkhorst and James D. Pack, Physical Review B **13** (12), 5188 (1976).

[5] A. R. Miedema, P. F. de Chatel, and F. R. de Boer, Physica B+C **100** (1), 1 (1980).

[6] F.R. de Boer, R. Boom, W.C.M. Mattens, A.R. Miedema, and A.K. Niessen, *Cohesion in metals: Transition Metal Alloys* (North Holland, Amsterdam, 1988).

[7] H. Bakker, *Enthalpies in Alloys: Miedema's semi-empirical model*. (Trans Tech Publications, Switzerland, 1998).

[8] A. K. Niessen, F. R. de Boer, R. Boom, P. F. de Chatel, W. C. M. Mattens, and A. R. Miedema, CALPHAD **7** (1), 51 (1983).

[9] F. A. Rioult, S. D. Imhoff, R. Sakidja, and J. H. Perepezko, Acta Materialia **57** (15), 4600 (2009).

[10] O. J. Lu-Steffes, R. Sakidja, J. Bero, and J. H. Perepezko, Surface and Coatings Technology **207**, 614 (2012).

[11] Jin-Kook Yoon, Kyung-Whan Lee, Sung-Jae Chung, In-Jin Shon, Jung-Mann Doh, and Gyeung-Ho Kim, Journal of Alloys and Compounds **420** (1–2), 199 (2006).

[12] Mitchell Meyer, Matthew Kramer, and Mufit Akinc, Advanced Materials **8** (1), 85 (1996).

[13] A. W. Smith, F. W. Meszaros, and C. D. Amata, Journal of the American Ceramic Society **49** (5), 240 (1966).

[14] Triplicane A. Parthasarathy, Robert A. Rapp, Mark Opeka, and Ronald J. Kerans, Journal of the American Ceramic Society **92** (5), 1079 (2009).

[15] P. A. Williams, R. Sakidja, J. H. Perepezko, and P. Ritt, J Eur Ceram Soc **32** (14), 3875 (2012).

DISTRIBUTION A: Distribution approved for public release.

[16] A Rezaie, WG Fahrenholtz, and GE Hilmas, J Eur Ceram Soc **27** (6), 2495 (2007).

[17] W. G. Fahrenholtz, Journal of the American Ceramic Society **90** (1), 143 (2007).

[18] G Urbain, Y Bottinga, and Po Richet, Geochimica et Cosmochimica Acta **46** (6), 1061 (1982).

[19] Sigrun N. Karlsdottir and John W. Halloran, Journal of the American Ceramic Society **92** (2), 481 (2009).

[20] Sigrun N Karlsdottir and John W Halloran, Journal of the American Ceramic Society **92** (6), 1328 (2009).

[21] P. W. Voorhees, J Stat Phys **38** (1-2), 231 (1985).

[22] Kathleen Shugart, Siying Liu, Forrest Craven, and Elizabeth Opila, Journal of the American Ceramic Society **98** (1), 287 (2015).

[23] M.V. Chase, *NIST-JANAF Thermochemical Tables*, 4th ed. (American Institute of Physics, Washington D.C., 1998).

[24] Maria Conceição Greca, JoséVitório Emiliano, and Ana Maria Segadães, J Eur Ceram Soc **9** (4), 271 (1992).

[25] E. F. Riebling, Journal of the American Ceramic Society **49** (1), 19 (1966).

[26] Sigrun N Karlsdottir, John W Halloran, and Anthony Nicholas Grundy, Journal of the American Ceramic Society **91** (1), 272 (2008).

[27] Sigrun N Karlsdottir, John W Halloran, and Carl E Henderson, Journal of the American Ceramic Society **90** (9), 2863 (2007).

[28] Mohamed N Rahaman, *Ceramic processing*. (Wiley Online Library, 2006).

[29] WG Fahrenholtz and GE Hilmas, International Materials Reviews **57** (1), 61 (2012).

[30] William G Fahrenholtz, Journal of the American Ceramic Society **90** (1), 143 (2007).

[31] Peter A Williams, Ridwan Sakidja, John H Perepezko, and Patrick Ritt, J Eur Ceram Soc **32** (14), 3875 (2012).

[32] Mylène Brach, Diletta Sciti, Andrea Balbo, and Alida Bellosi, J Eur Ceram Soc **25** (10), 1771 (2005).

DISTRIBUTION A: Distribution approved for public release.

[33] M. W. Chase, *NIST-JANAF Thermochemical Tables, 4th Edition*. (American Institute of Physics, Washington, DC, New York, 1998).

[34] M. M. Opeka, I. G. Talmy, and J. A. Zaykoski, Journal of Materials Science **39** (19), 5887 (2004).

[35] M. Playez, D. G. Fletcher, J. Marschall, W. G. Fahrenholtz, G. E. Hilmas, and S. M. Zhu, Journal of Thermophysics and Heat Transfer **23** (2), 279 (2009).

[36] A Rezaie, W. G. Fahrenholtz, and G. E. Hilmas, Journal of the American Ceramic Society **89** (10), 3240 (2006).

[37] William. M. Haynes, *CRC handbook of chemistry and physics*. (CRC press, 2014).

[38] P. C. Tortorici and M. A. Dayananda, Materials Science and Engineering: A **261** (1–2), 64 (1999).

DISTRIBUTION A: Distribution approved for public release.

AFOSR Report University of Wisconsin-Madison

Arc Jet Testing and Evaluation of Mo-Si-B Coated Mo and SiC-ZrB_2 Ceramics

The transition from blunt leading edges to sharp leading edges on re-entry aircrafts is necessary to increase both maneuverability and safety. However, the oxidation resistance of current materials is inadequate for the extreme conditions experienced by sharp leading edge re-entry vehicles. The Mo-Si-B alloy system has been utilized to design a multilayer coating that has the ability to protect from 800-1700°C. Substrates of Mo and ZrB_2-50 vol% SiC with a flat profile were coated with the Mo-Si-B based coating and evaluated using arc jet testing performed at NASA Langley Research Center (figs.1 and 2). Heat fluxes of 2.5 to nearly 3.5 MW/m^2 and surface temperatures of 1500-1650°C were achieved during the 20-minute tests. The samples presented in this study showed < 3% mass loss and retention of sample shape and integrity, demonstrating the robust environmental protection under a simulated hypersonic environment offered by the Mo-Si-B based coating on refractory metals and ceramics.

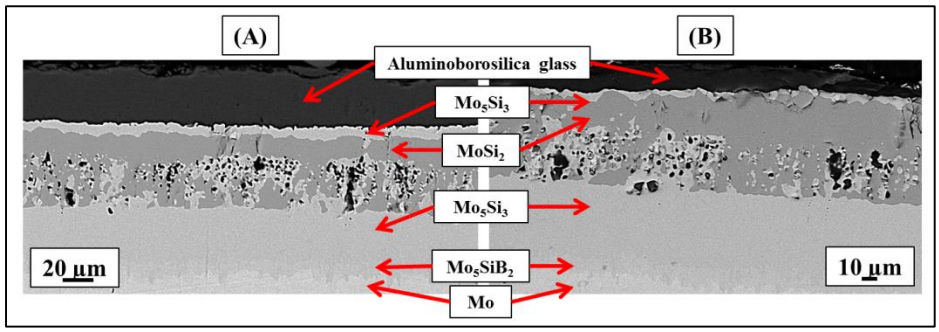

Fig. 1 Backscattered cross-sectional SEM images of (A) Mo sample coated with Si and B via pack cementation and oxidized in air for 2 hours at 1600°C, as was the condition of the Mo-Si-B samples before arc jet testing; and (B) sample Mo-Si-B coated Mo after 20 minutes of exposure during arc jet testing.

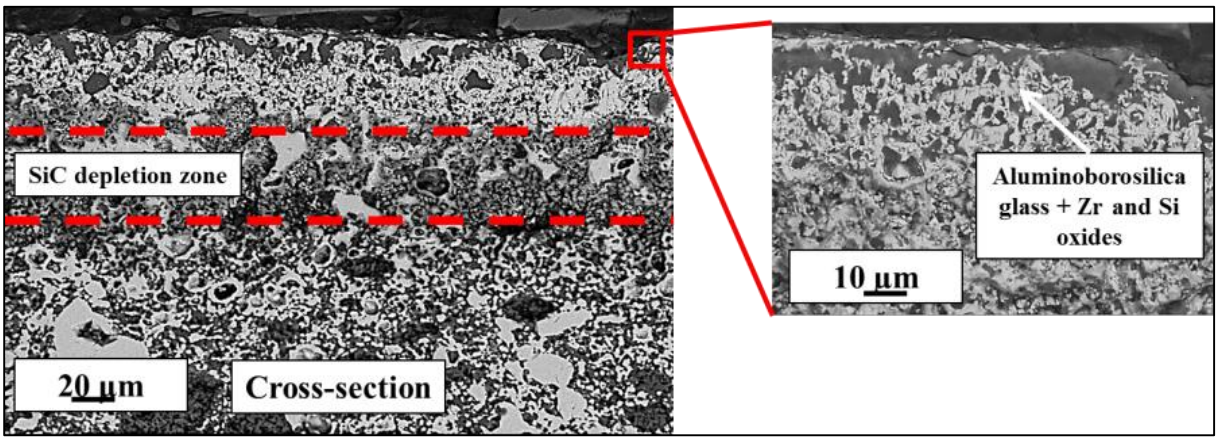

Fig. 2 Backscattered SEM images of the cross-section of ZrB_2-50 vol% SiC after arc jet testing.

DISTRIBUTION A: Distribution approved for public release.

UVM ICP Torch Testing

Two "mushroom"-shaped Mo samples with a diameter of ~25mm were coated with Si and B via pack cementation. This process takes place under argon at 1000°C for 50 hours. The Si-to-B ratio was 35:1 in weight percent. After the co-deposition of Si and B, the samples were oxidized in air at elevated temperature (at least 1300°C) for several hours and sent to the University of Vermont for inductively-coupled plasma (ICP) torch testing in pure nitrogen. The conditions of both tests are summarized in the table below.

Gas flow	Chamber pressure	Heat flux	Free stream temp.	Sample surface temp.	Exposure time
40 liters per minute	160 Torr	60 +/- 5 W/cm^2	6000 +/- 500K	1500K	10 minutes

Both samples survived the tests. Sample #1 showed both matte and glassy regions on the surface, depicted below (figs. 3 and 4). The reason for the glassy surface appeared to be retention of Na within the aluminosilica glass. The matte region was still amorphous, but the lack of Na appears to increase the viscosity of the glass. No detectable microstructural changes were seen. The cross-sectional view of both regions shows the layered structure consisting of $MoSi_2$, Mo_5Si_3 and Mo_5SiB_2 was retained after the test.

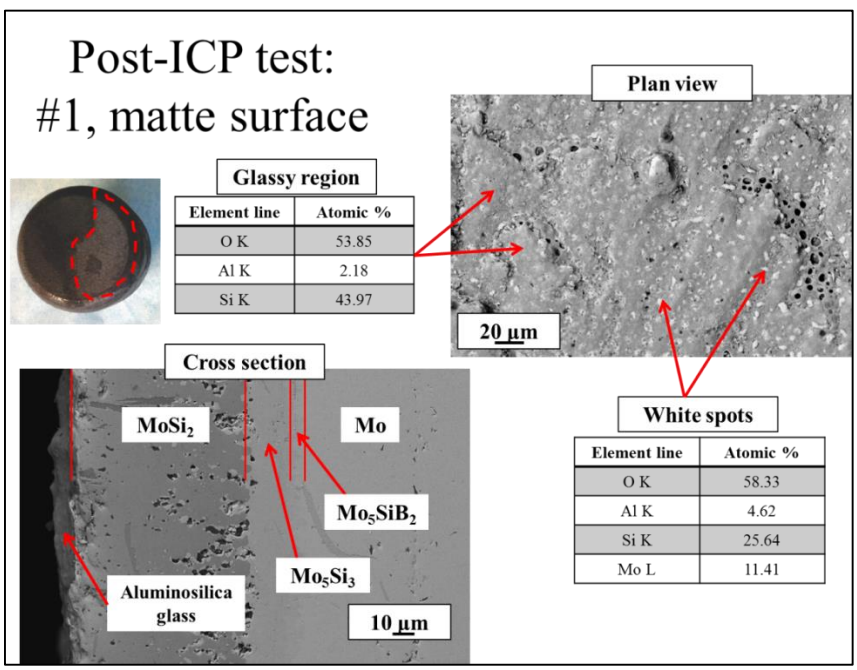

Fig. 3 Matte surface microstructure for sample 1 after ICP test.

DISTRIBUTION A: Distribution approved for public release.

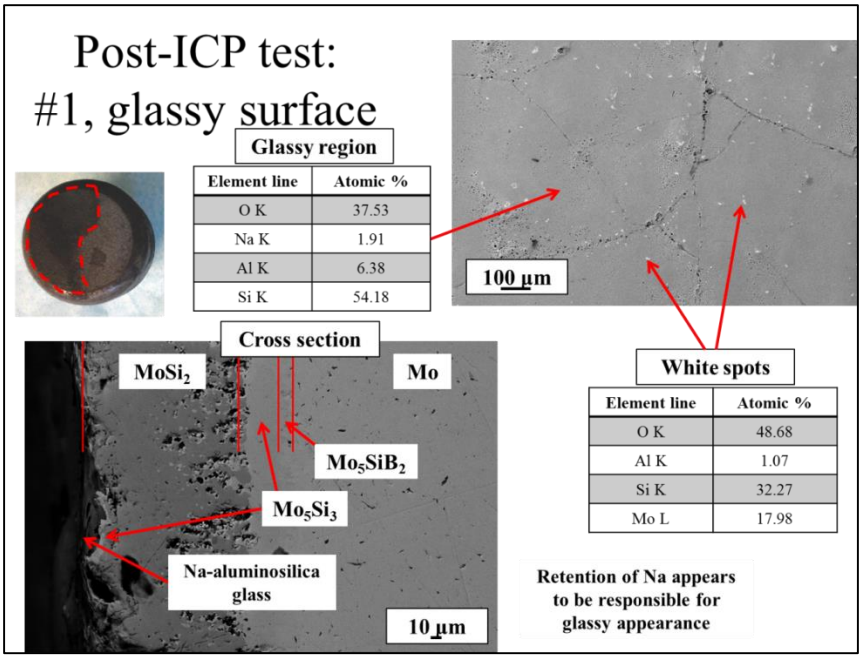

Fig. 4 Glassy surface microstructure for sample 1 after ICP test.

Sample #2 had a surface that was completely matte grey (fig.5), and the external glass composition was found to be nearly identical to that of the matte region in Sample #1. There were some Al-rich regions found on the surface as well. However, as in the case of Sample #1, there were no microstructural changes seen, and the oxidation-resistant layered structure was retained after testing.

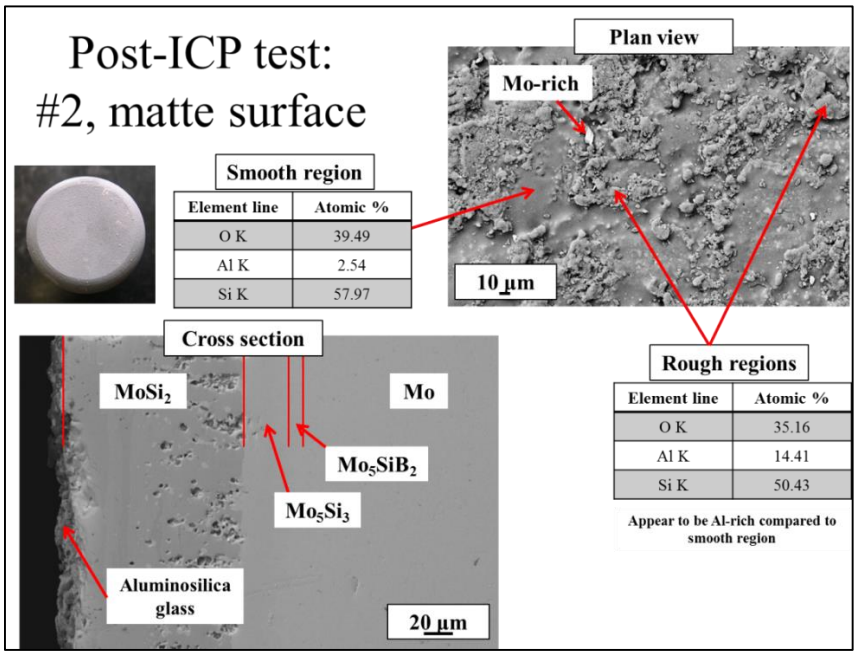

Fig.5 Matte surface microstructure for sample 2 after ICP test.

DISTRIBUTION A: Distribution approved for public release.

Two “mushroom”-shaped Mo-14.2 at.% Si-9.6at.% B alloys with a diameter of ~18 mm were coated with Si and B via pack cementation as described above. The move to smaller diameters was an attempt to test at higher temperatures than in the 25mm diameter case. After the co-deposition of Si and B, the samples were conditioned at 1300°C for 15 hours and sent to the University of Vermont for inductively-coupled plasma (ICP) torch testing. The 30 kW torch developed at UVM simulates the high temperature chemically reacting boundary layer of reentry and atmospheric hypersonic flight. Surface temperatures are measured using a two-color infrared optical pyrometer, and a spectrometer was employed to perform qualitative and quantitative assessment of the near-surface plasma and surface ejected material species. One sample was run a total of three times; the first two tests were to establish suitable conditions for a 20-minute test at ~2000K. During the first two tests, the gas used was air with a flow rate of 40 liters per minute (LPM) and a pressure of 160-190 Torr. These conditions were held for 8 and 6 minutes, and resulted in maximum surface temperatures of 1970 and 2000K, respectively. The final test used a mixture of air and argon flowing at 10 and 30 LPM, respectively, with a pressure of 200+ Torr and was run for 20 minutes. The resulting maximum surface temperature during this final run was 2000K. After the three tests the total mass loss of the sample was 0.007 g, or 0.02 wt%.

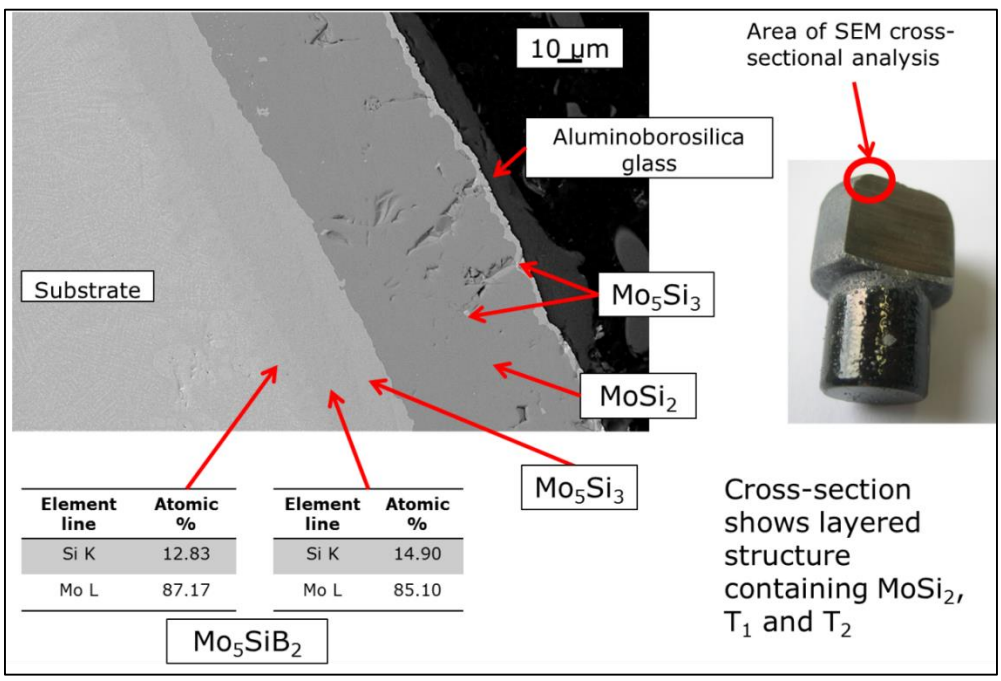

Fig. 6 Cross section of a coated Mo-14.2 at.% Si-9.6at.% B alloy after three ICP test runs.

Emission data showed no clear signs of ejected coating species (i.e., Si or B) during any of the tests, demonstrating the stability of the Mo-Si-B coating under the extreme conditions imposed by ICP torch testing. Visually the outer surface of the sample had changed from a glossy black exterior to a matte grey exterior after the three tests, indicative of some devitrification of the

external aluminoborosilica glass. This is likely due to the cycling between the test conditions and ambient conditions. Cross-sectional analysis using scanning electron microscopy (SEM) (Fig.6) equipped with energy dispersive X-ray spectroscopy (EDS) showed a layered structure consisting of Mo_5Si_3 (T_1), $MoSi_2$, and Mo_5SiB_2 (T_2). No penetrating cracks were seen. Surface examination revealed majority Si-rich oxides, with some Al and Na oxides present as a byproduct of the pack cementation. Some Mo-rich particles were also seen on the surface. Overall the test shows the superior performance of the Mo-Si-B coating as a protective barrier for the extreme conditions imposed by hypersonic flight and reentry conditions. Further testing at UVM will confirm the efficacy of the coating for such environments.

One cone-shaped Mo sample (Fig. 7) was coated with Mo-Si-B and sent to the University of Vermont for ICP torch testing. The cone geometry allows for higher heat fluxes during ICP torch testing, thus allowing for a more stringent test of the oxidation protection provided by the Mo-Si-B coating. The cone-shaped sample is shown schematically below alongside a ZrB_2-30 vol% SiC cone-sample sample manufactured at Iowa State University.

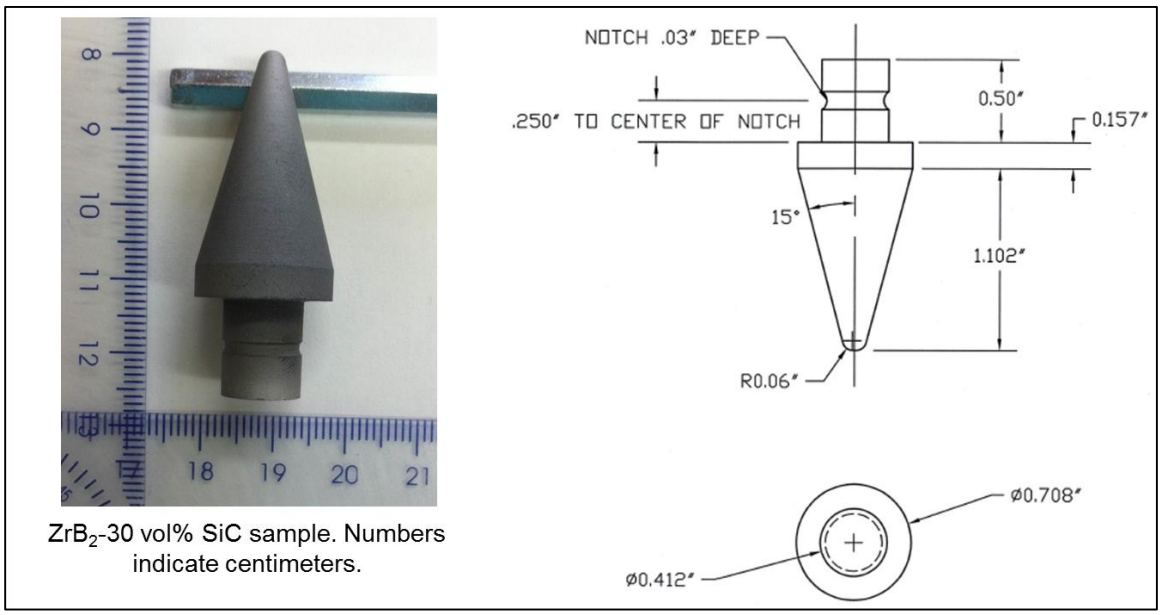

Fig. 7 Cone shaped sample geometry.

The Mo-Si-B coated and conditioned Mo cone sample was tested five times at the University of Vermont (fig.8). Details of the tests are given in the table below. In all cases, no Si or B emission species were detected. As can be seen in the image below, the sample did not undergo any major external changes after the five ICP torch tests performed, again demonstrating the robust oxidation protection offered by the Mo-Si-B based coating. Cross-sectional SEM analysis (fig.9) shows that the coating offered protection even at the very tip of the Mo cone, with the only notable changes in the coating structure being a slight reduction in the external glass thickness. This is consistent with the results of the arc jet testing performed at NASA Langley. Some glass

was seen within the coating structure as well, which may indicate a breach that likely resulted due to the cyclic nature of the testing. However, the glass was effectively able to flow to cover any breach within the coating structure, even under the aggressive conditions of ICP torch testing.

Summary of ICP Torch Test Conditions for Mo-Si-B Coated Mo Cone Sample

Test	**Gas flow (LPM)**	**Chamber pressure (Torr)**	**Sample elevation (mm)**	**Max surface temperature (°C)**	**Time (s)**
20140506a	40 (N_2)	160	90	1450	~305
20140506b	40 (air)	160	90	1610	~290
20140512a	40 (air)	160	48	1680-1700	~325
20140512b	40 (air)	160	26	1745-1755	~135
20140513	10 (air)/30 (Ar)	200	26	1450	~150

Fig. 8 Mo-Si-B coated Mo cone sample before (left) and during (middle) and after all five ICP torch tests (right).

DISTRIBUTION A: Distribution approved for public release.

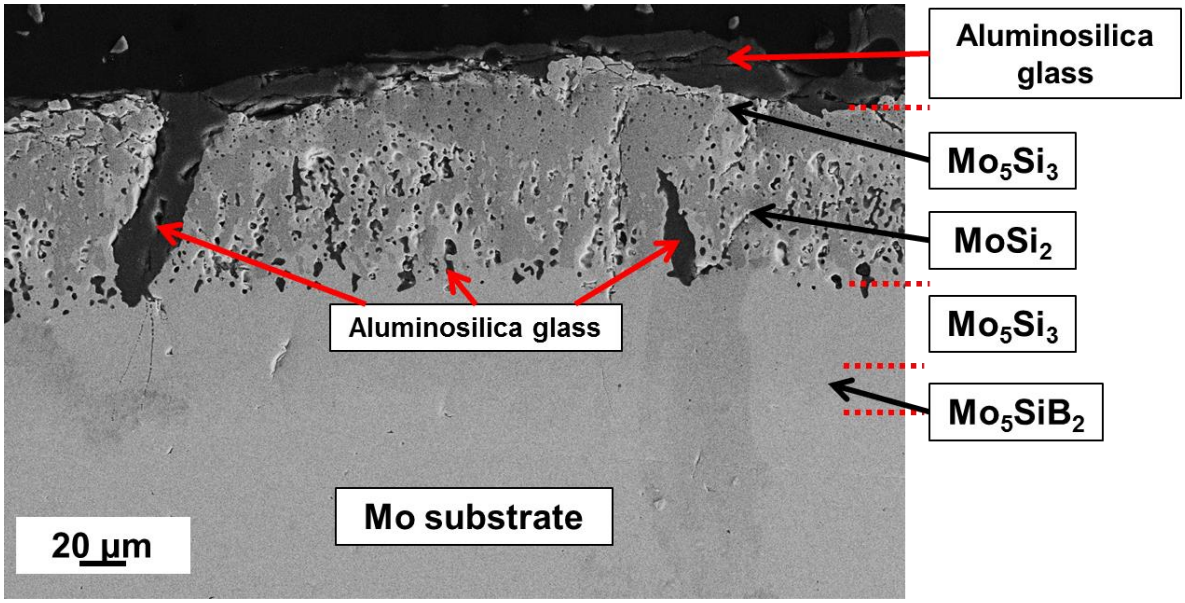

Fig. 9 Cross-sectional SEM image of the tip of the Mo-Si-B coated Mo cone after five consecutive ICP torch tests.

Cone-shaped Mo and ZrB_2-30 vol% SiC samples have been manufactured and sent to the University of Wisconsin-Madison to be coated with Mo-Si-B. The samples were coated in the following manner:

1) A mixture of 5 mL of 1-5 µm Mo powder and 20 mL of nitrocellulose lacquer was mixed and deposited onto the surface of the samples with a siphon-feed airbrush. After complete coverage of the substrate was achieved, samples were allowed to air dry.

2) An annealing treatment for the Mo layer was carried out at 1300°C for 2 hours under a pressure of 10^{-5} Torr. The ramp rate to 1300°C was 350°C/hour.

3) Steps 1 and 2 were repeated to make sure that the substrates were completely covered in Mo.

4) Co-deposition of Si and B through pack cementation. The Si:B ratio was 35:1 in weight percent. Alumina was used as a filler and NaF as the activator. The samples were immersed in the powder and coated at 1000°C for 90 minutes.

After removal from the pack cementation, the samples were oxidized in ambient air to form the external glass of the Mo-Si-B based coating. The oxidation treatment was at 1400°C for 5 hours.

The ICP torch testing conditions were as follows: Air flowed over the sample at 40 liters per minute at a pressure of 160 Torr. The temperature reached was ~1423°C during the 20 minute test, which is lower than previous conical tests. The mass loss after testing was 0.747 g, mostly

due to the erosion of the coating during the first 2-3 minutes of testing (fig. 10). Mo, Si and Na emission spectra were detected during testing, confirming the coating erosion. It is believed that the differing Mo deposition process used on these samples may not have good adhesion to the sample substrate, especially when compared to the arc jet testing results above. However, the initial result shows a still-minimal mass loss and retention of the substrate shape and dimensions after 20 minutes of testing.

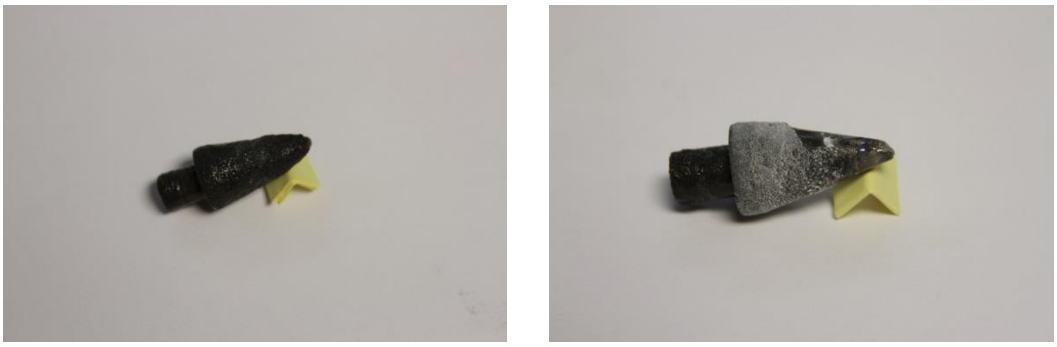

Fig. 10 Pre-test (left) and post-test (right) images of Mo-Si-B coated ZrB2-30 vol% SiC cone after a 20-minute ICP torch test.

Oxidation Tests in Partially Dissociated Low Pressure Flow

Ten Mo-Si-B coated Mo coins were sent to SRI International for oxidation in partially dissociated oxygen. These pure Mo coins were coated with Si and B using pack cementation at 1000°C for 50 hours under argon. The Si to B ratio was 35:1 in weight percent. After the pack cementation process, samples were oxidized in air at elevated temperature (at least 1300°C) for several hours. The testing apparatus is shown schematically below (fig.11), and test conditions are summarized for the four tested samples in the table below.

DISTRIBUTION A: Distribution approved for public release.

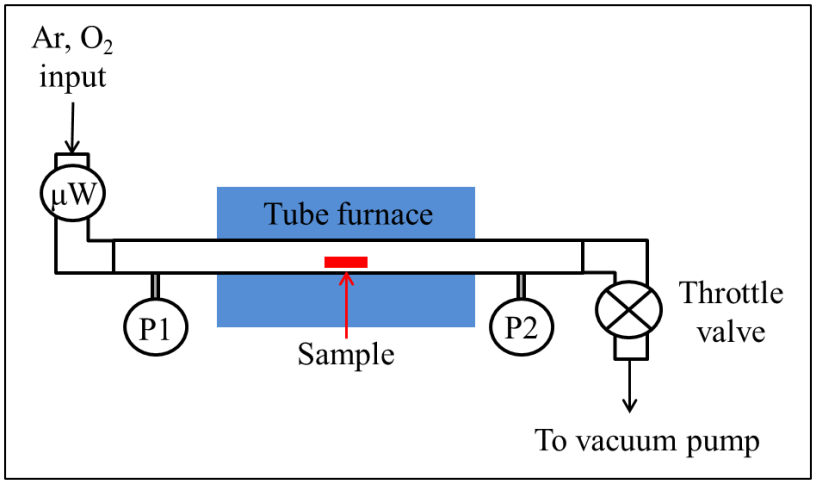

Fig. 11Schematic of experimental setup at SRI International

Test Conditions at SRI International

Sample	T (°C)	Time (min)	O_2 flow (sccm)	P_1 (Torr)	P_2 (Torr)	P_{sample} (Torr)*	v_{sample} (m/s)*	Discharge	Mass change (mg)
JP1	1000	600	303	1.460	0.946	1.25	37	Off	-2.25
JP2	1000	600	303	1.458	0.941	1.25	37	On	-0.77
JP3	1200	600	303	1.577	0.944	1.34	40.7	Off	-0.33
JP4	1200	600	303	1.594	0.931	1.36	40.1	On	-17.03

*Estimated from the measured oxygen mass flow, furnace temperature and P1 and P2 using the ideal gas law and the Hagen-Poiseuille equation

For the 1000°C tests, the O-atom concentration at the sample location was estimated to be about 1.6x10-4 moles/m3 or, equivalently, an O-atom partial pressure of about 12 mTorr or an O-atom mole fraction of about 1%. A similar O-atom mole fraction was expected for the 1200°C tests. The O-atom mole fractions in the discharge flow tube are three to four orders of magnitude higher than in thermal equilibrium.

There were no noticeable microstructural differences across the four samples tested. SEM micrographs of samples JP1 and JP4 are shown below (figs. 12 and 13). Though JP4 lost more mass than the other samples, there is no discernible difference between the two samples. Both exhibit an amorphous aluminosilica glass on the surface, and both show that the oxidation-resistant layered structure of $MoSi_2$, Mo_5Si_3 and Mo_5SiB_2 was retained after the test. The Mo-Si-B coated Mo samples appeared to survive the tests without any major microstructural change or mass loss and show excellent repeatability.

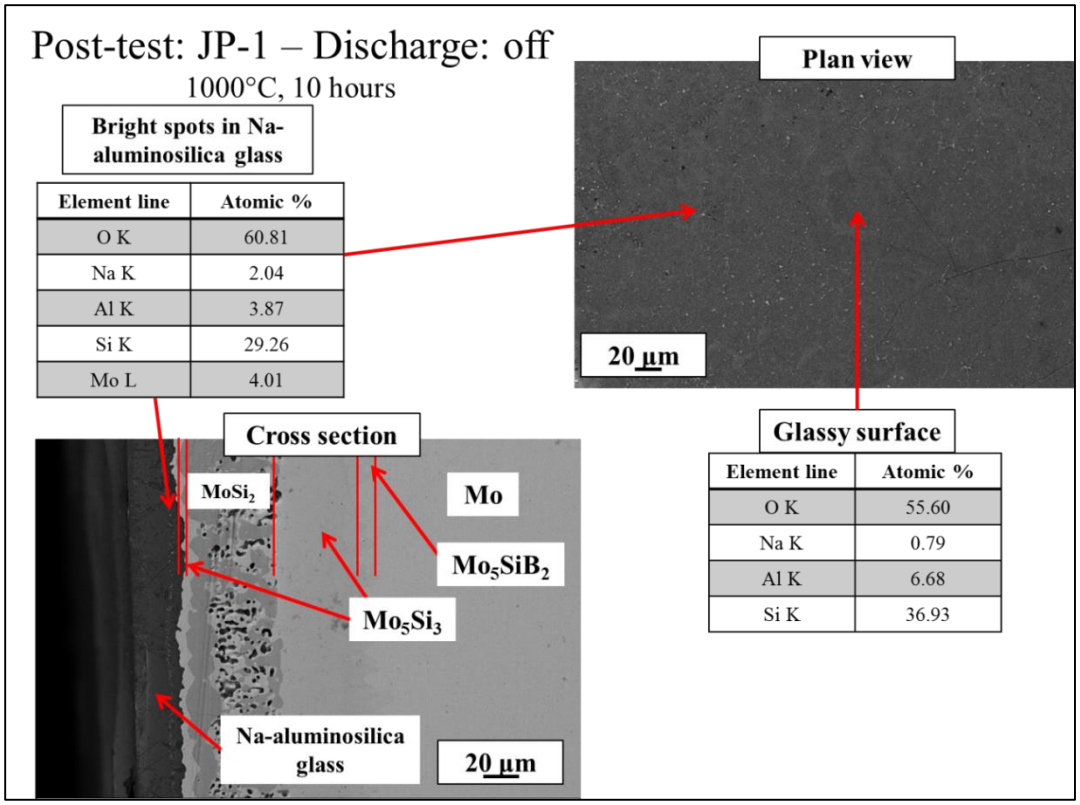

Fig. 12 Microstructure of MoSiB coated Mo sample after JP-1 test.

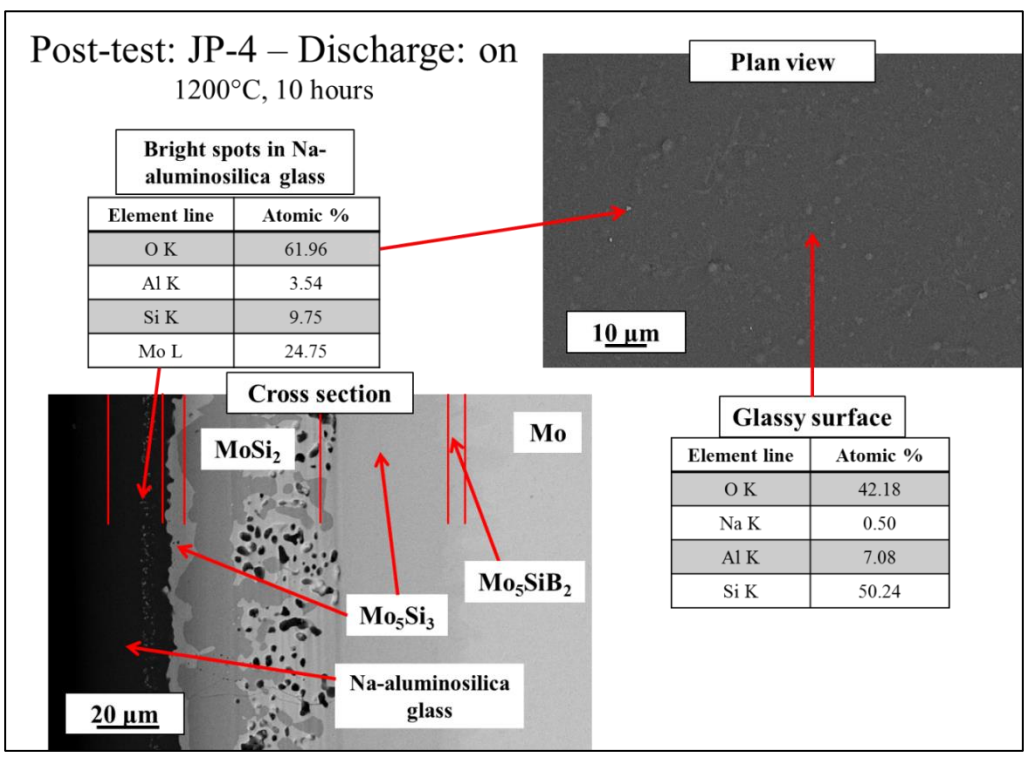

Fig. 13 Microstructure of MoSiB coated Mo sample after JP-2 test..

Mo-Si-B Coating on SiC-ZrB_2 Ceramics and Mo-W-Si-B Alloys

Previously two ZrB_2-30 vol% SiC samples were sent to the University of Wisconsin-Madison from Iowa State University to deposit the Mo-Si-B based coating. These samples were coated with Mo-Si-B via a two-step process in which an initial layer of Mo is deposited followed by co-deposition of Si and B (35:1 Si:B wt % ratio) for 1.5 hours at 1000°C under Ar. One Mo-Si-B coated sample was tested for ten 1-hour cycles at 1450°C (fig. 14) and showed significantly less mass loss than the uncoated ZrB_2-30 vol% SiC sample (2.5 mg/cm^2 for the coated sample and 12.8 mg/cm^2 for the uncoated sample). The thickness of the borosilicate scale on the coated sample increased from 60 to 80 microns after 10 cycles at 1450°C. One coated ZrB_2-30 vol% SiC coupon was also isothermally oxidized at 1600°C for 10 hours, resulting in a mass gain of 2.3 mg/cm^2. By comparison the uncoated ZrB_2-30 vol% SiC coupon gained 18 mg/cm^2 after only 5 hours at 1600°C. Initial test results indicate that the Mo-Si-B based coating is effective in protecting the ZrB_2-30 vol% SiC substrate from rapid oxidation.

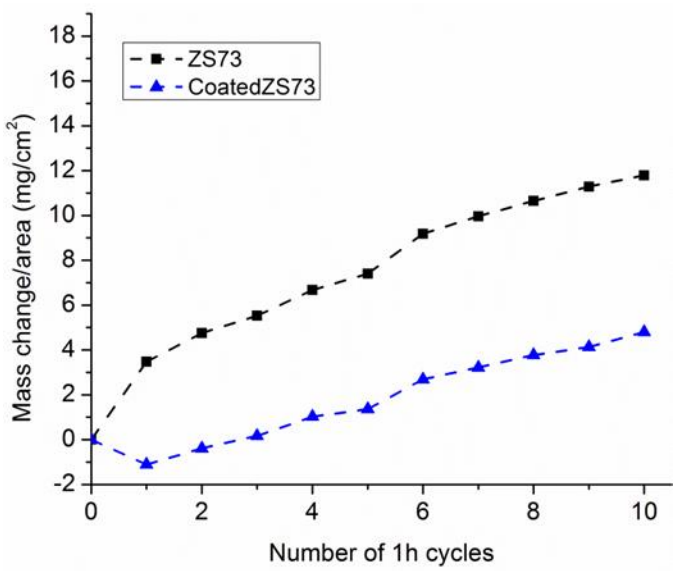

Fig. 14 Mass change during cyclic oxidation at 1450°C of a Mo-Si-B coated ZrB_2-30 vol% SiC sample (CoatedZS73) and an uncoated ZrB_2-30 vol% SiC sample (ZS73).

Four additional sets of samples were prepared at Iowa State University and sent to the University of Wisconsin-Madison to deposit the Mo-Si-B coating. The first two sets are SiC-ZrB_2 ceramics; the two compositions are 70 vol% ZrB_2-30 vol% SiC and 60 vol% ZrB_2-30 vol% SiC-10 vol% AlN. These samples were sintered at 2000°C for 2 hours and ground and polished to 600 grit. These samples were also coated via the two-step process as detailed above. There has been some difficulty in coating these samples in that the disc geometry is very thin, thus leading to sharp

DISTRIBUTION A: Distribution approved for public release.

edges even after attempts to round the edges. Traditionally the initial layer of Mo is deposited on ceramic samples at the University of Wisconsin-Madison through decomposition of $Mo(CO)_6$, but this has proven largely ineffective for this set of samples. A new technique using a slurry made up of Mo powder and nitrocellulose lacquer does show some promise for depositing the initial layer of Mo on the ceramic samples. Nonetheless, several samples have been fully coated and conditioned (1300°C for 5 hours in air) and were sent to Iowa State University for further testing.

The second two sets of samples received from Iowa State University are Mo-W-Si-B alloys. The first nominal composition is $Mo_{50}W_{20}Si_{20}B_{10}$ and the second nominal composition is $Mo_{50}W_{20}Si_{15}B_{15}$. These samples were prepared using a tri-arc melter and then drop cast into 10 mm rods. The rods were subsequently sectioned via electrical discharge machining (EDM). The alloys were coated via pack cementation to co-deposit Si and B (35:1 Si:B wt % ratio) for 50 hours at 1000°C under Ar. Samples of the composition $Mo_{50}W_{20}Si_{15}B_{15}$ have been coated and conditioned (1500°C for 5 hours in air) successfully. Oxidation testing performed at Ames Laboratory show a significant enhancement of the oxidation resistance of Mo-W-Si-B alloys when a Mo-Si-B based coating is applied to the surface. The coated alloy was pre-treated at 1500°C for 5 hours. The top layer comprised of an aluminoborosilicate scale; the bulk of the coating, underneath the top layer, was comprised of $MoSi_2$ and Mo_5Si_3. No significant damage was observed during the oxidation behavior of the coated alloy at various temperatures Ffig.15).

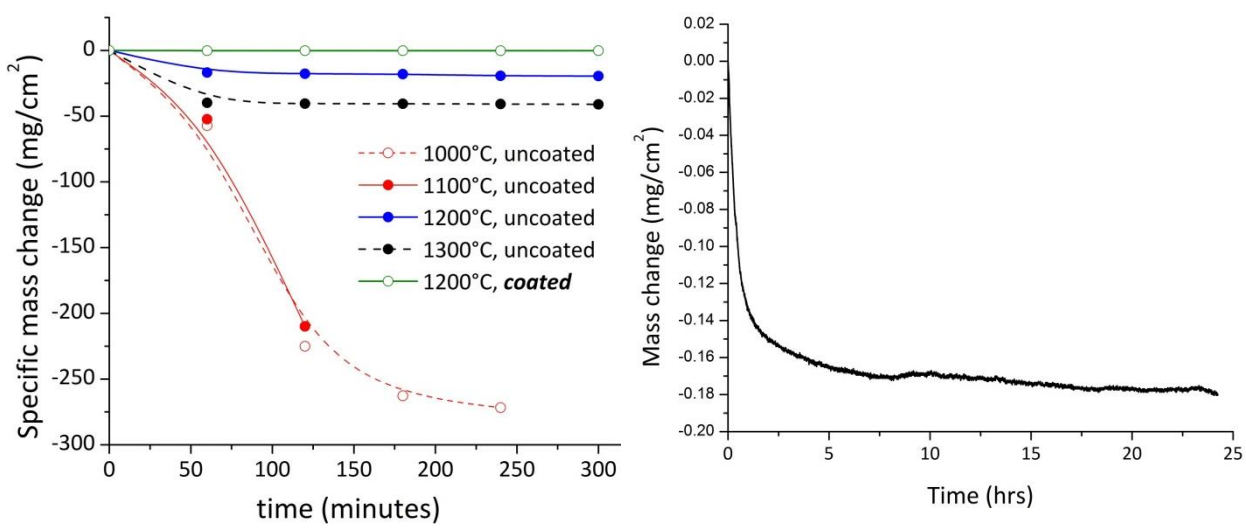

Fig. 15 Oxidation kinetics of the coated and uncoated $Mo_{50}W_{20}Si_{15}B_{15}$ alloy between 1000 – 1300°C; (b) isothermal oxidation kinetics of the coated alloy at 1000°C.

<u>Active Oxidation of SiC and Mo-Si-B Coated SiC</u>

Proposed leading-edge materials for hypersonic and reentry vehicles such as SiC-based composites must be evaluated under the high temperature, low partial pressure of oxygen conditions that will be experienced in service. Such conditions can induce a phenomenon known as active oxidation in SiC, in which the oxidation products are volatile SiO(g) and CO(g) rather than the protective layer of SiO_2. Previous active oxidation tests were performed at NASA Glenn at 1500°C and 100 ppm O_2/balance Ar and showed rapid consumption of both SiC/C and Mo-Si-B coated SiC/C. In an attempt to prevent active oxidation of the Mo-Si-B based coating on SiC, small (0.25 – 5 wt%) additions of Al have been explored. The Al substitutes for the Si in the pack cementation composition, thus depositing Al, Si and B simultaneously. These Mo-Si-B-Al coatings have been shown to prevent rapid mass loss in low oxygen environments on SiC/SiC composites, as shown below (fig. 16). However, the Al additions did not improve the resistance to active oxidation compared to the coating without the Al additions. This was due to a combined effect of Al additions reducing the viscosity of the external glass, as well as the oxidation of the BN interphase to produce boria, thereby further reducing the viscosity of the glass. The reduced viscosity is then accompanied by an enhanced inward diffusion of oxygen as well as enhanced kinetics that would promote crystallization of the coating over an extended period of time. However, it is worth noting that the low viscosity of the glass did allow for any coating breach to be sealed quickly, and that all coating samples performed much better in terms of mass loss compared to the uncoated SiC/SiC composite.

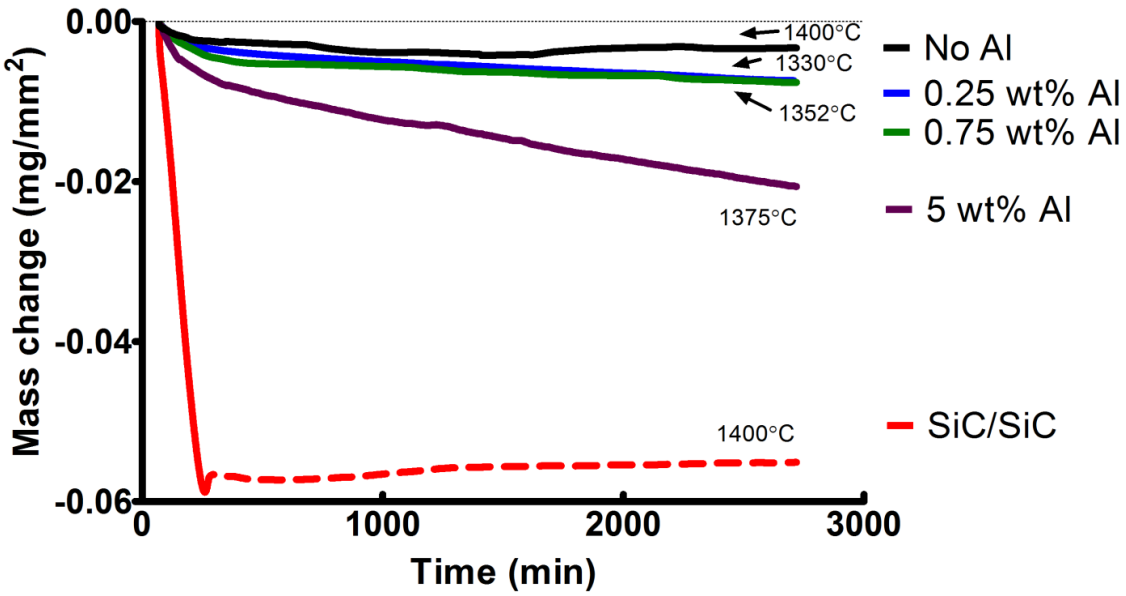

Fig. 16 Thermogravimetric analysis of uncoated, Mo-Si-B coated, and Mo-Si-B-Al coated SiC/SiC composites in 100 ppm O_2/balance Ar environment. Each sample test temperature is noted by the respective curve. “No Al” refers to Mo-Si-B coated SiC/SiC. Respective additions of Al are noted next to each respective curve. “SiC/SiC” refers to uncoated SiC/SiC composite.

DISTRIBUTION A: Distribution approved for public release.

Given the scarcity of SiC/SiC composites available, CVD SiC was used as the substrate in current testing. Thermogravimetric analysis (TGA) at 1385-1400°C in 100 ppm O_2/balance Ar for 20-45 hours of three CVD SiC coupons showed initial rapid mass loss, though the effect of preoxidation at 1500°C for several hours to produce an ambient silica layer was minimal in terms of extended mass change. This initial rapid mass loss exhibited by the CVD SiC samples is indicative of active oxidation. A plot of the mass change and the test conditions are given in the graph (fig. 17) and table below.

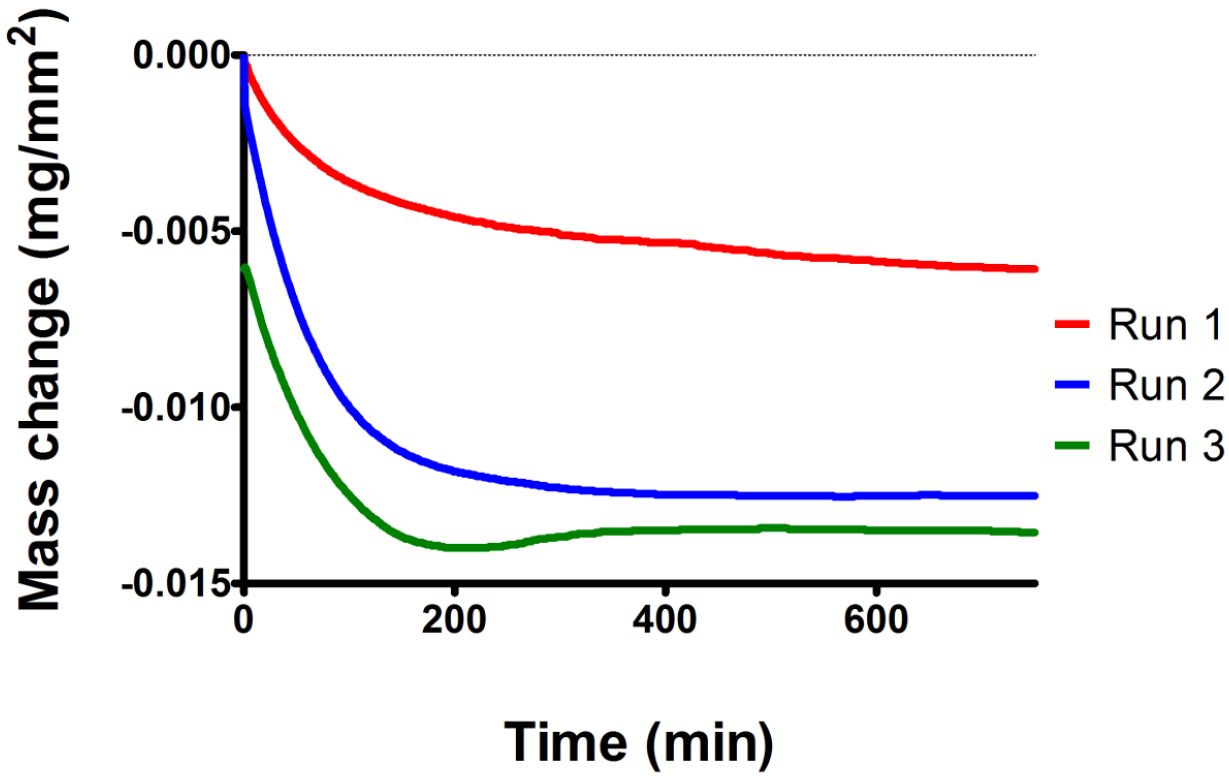

Fig. 17 TGA results for CVD SiC coupons exposed to flowing 100 ppm O_2/balance Ar at 1385-1400°C. Details pertaining to each run are displayed in Table XI. The data has been cut off at 750 minutes to show the initial mass loss in greater detail.

DISTRIBUTION A: Distribution approved for public release.

TGA Conditions for CVD SiC Coupons in Flowing 100 ppm O_2/Balance Ar Environment

Run number	**Oxidation condition**	**Flow rate (mL/min)**	**Temperature (°C)**	**Dwell time (hh:mm)**	**Steady state mass loss (mg/mm^2-min)**
1	None	100 for the first 20:15, then 150 for the remaining 22:25	1400	42:40	$1x10^{-6}$
2	None	150	1400	45:00	$4x10^{-7}$
3	1500°C for 5 hours in ambient air	150	1385	20:00	$7x10^{-7}$

An alternative way to include aluminum in the Mo-Si-B coating is a three-step process. Instead of substituting the Al in the Si-B pack cementation process, there is a second separate pack cementation solely to deposit aluminum. This provides better control of how much aluminum is deposited by eliminating the competition from Si and B fluorides during the pack cementation process. The three-step process also limits aluminum additions to the exterior surface of the coating. In this process, the samples coated with Mo-Si-B should be oxidized in air prior to the second Al pack cementation. In this way the aluminum reacts with the external aluminoborosilica glass to form alumina. Aluminum was deposited onto the surface of the conditioned samples through pack cementation at 1000°C for 1 hour. The aluminum pack cementation powder composition was 1-5 wt% Al, 2.5 wt% NaF and balance Al_2O_3 filler. The resulting coating had an external alumina layer (mixture of α and θ-phase) with an underlying aluminoborosilica glass with incorporated Mo-silicide phases, determined to be largely Mo_5Si_3.

A test in ambient air was performed on Mo-Si-B + 5 wt% Al coated CVD SiC to determine the compatibility of the coating with the substrate. The sample was oxidized cyclically at 1450°C in ambient air. The cycles were one hour each, with 30 minutes outside of the furnace in between each cycle. A mass change of +0.94 wt% was determined after the completion of ten cycles. While mullite was not easily resolved by X-ray diffractometry (fig. 18), it must exist within the Mo-Si-B + Al coating. However, if the mullite is restricted to the surface of the coating this should not affect the self-healing behavior of the coating as long as the layer of aluminoborosilica glass underneath does not crystallize or evaporate. The small amounts of Al (<5 wt%) and incidental Al_2O_3 additions to the coating should allow the glass to remain fluid as long as the interaction with the glass is limited. This was proven by the limited mass gain

DISTRIBUTION A: Distribution approved for public release.

exhibited by the Mo-Si-B + 5 wt% Al coated CVD SiC sample cyclically oxidized at 1450°C for ten one-hour cycles. Any spallation due to crystallization and/or CTE mismatches would have resulted in a significant mass loss – the loss of both the alumina top layer and the aluminoborosilica glass – that could not be regained through the oxidation of exposed SiC to form SiO_2. The Al additions, then, appear to be compatible with the Mo-Si-B coating as well as the CVD SiC substrate.

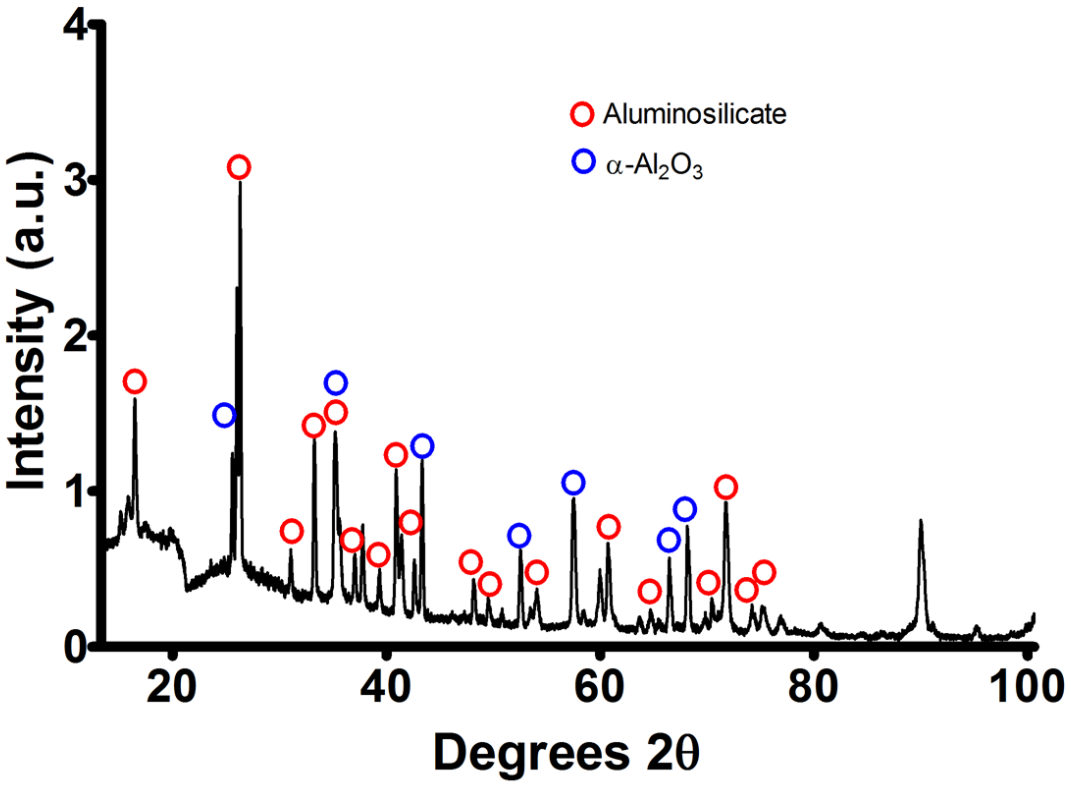

Fig. 18 X-ray diffraction from the surface of a Mo-Si-B + 5 wt% Al coated CVD SiC coupon after 10 one-hour cycles at 1500°C in ambient air.

Thermogravimetric analysis was conducted on oxidized CVD SiC, Mo-Si-B coated CVD SiC and Mo-Si-B + 5 wt% Al coated CVD SiC at 1400°C in flowing 100 ppm O_2/balance Ar gas. The results are plotted in figure 19. It is clear that the Mo-Si-B + 5 wt% Al sample has superior resistance to mass loss in active oxidation conditions, in terms of steady state mass loss (~9x10-6 mg/mm2-min) as well as total mass change. Post-test plan view SEM micrographs showed large grains of alumina and regions of aluminoborosilica glass (fig. 20). The cross-sectional view in figure 21 shows a layer of alumina on the surface of the sample, with intermixed $MoSi_2$ and Mo_5Si_3 and aluminoborosilica underneath. The aluminum content in the aluminoborosilica layer indicated was ~5-10 at%, as determined by EDS.

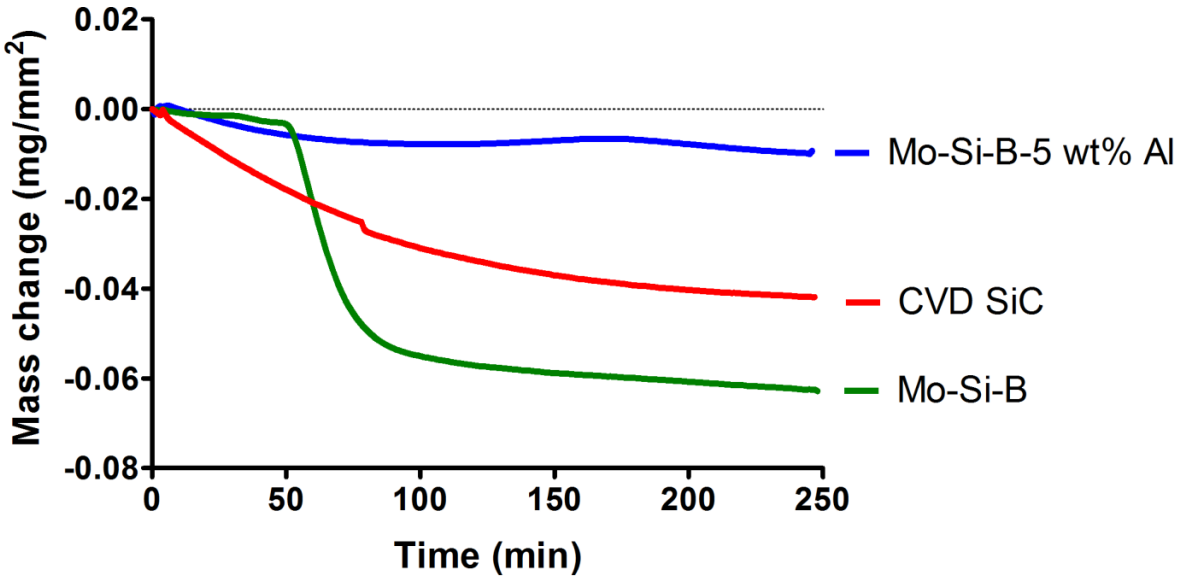

Fig. 19 In situ mass change results from exposure of oxidized CVD SiC ("CVD SiC"), Mo-Si-B coated CVD SiC ("Mo-Si-B") and Mo-Si-B + 5 wt% Al coated CVD SiC ("Mo-Si-B-5 wt% Al") to 100 ppm O_2/balance Ar flowing at 100 mL/min at 1400°C for 4 hours each.

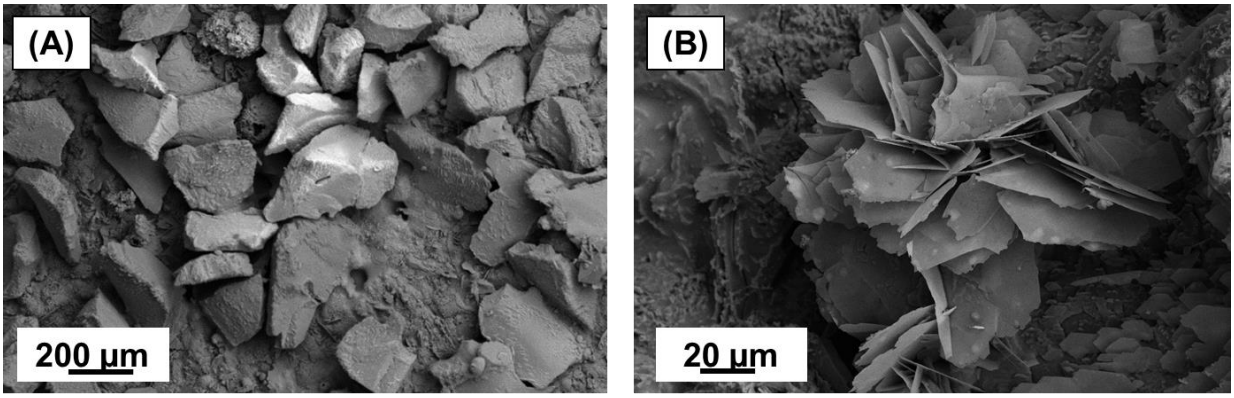

Fig. 20 Plan view backscattered SEM image showing (A) α-Al_2O_3 and (B) θ-Al_2O_3 on the surface of as-packed Mo-Si-B + 5 wt% Al on CVD SiC.

The evidence here supports the reduced oxygen diffusion through the external glass of the Mo-Si-B based coating due to the additions of Al/Al_2O_3 on the surface. Further, a reaction between the aluminoborosilica glass and the external alumina additions will produce mullite, which will dissolve below 1634°C until a critical alumina saturation is reached within the glass. This formation and dissolution of mullite at the glass/Al_2O_3 interface is expected to continue uninhibited, ceasing only with saturation of the glass phase or complete consumption of the outer layer of alumina, resulting in continuous enrichment of the aluminoborosilica glass with alumina.

DISTRIBUTION A: Distribution approved for public release.

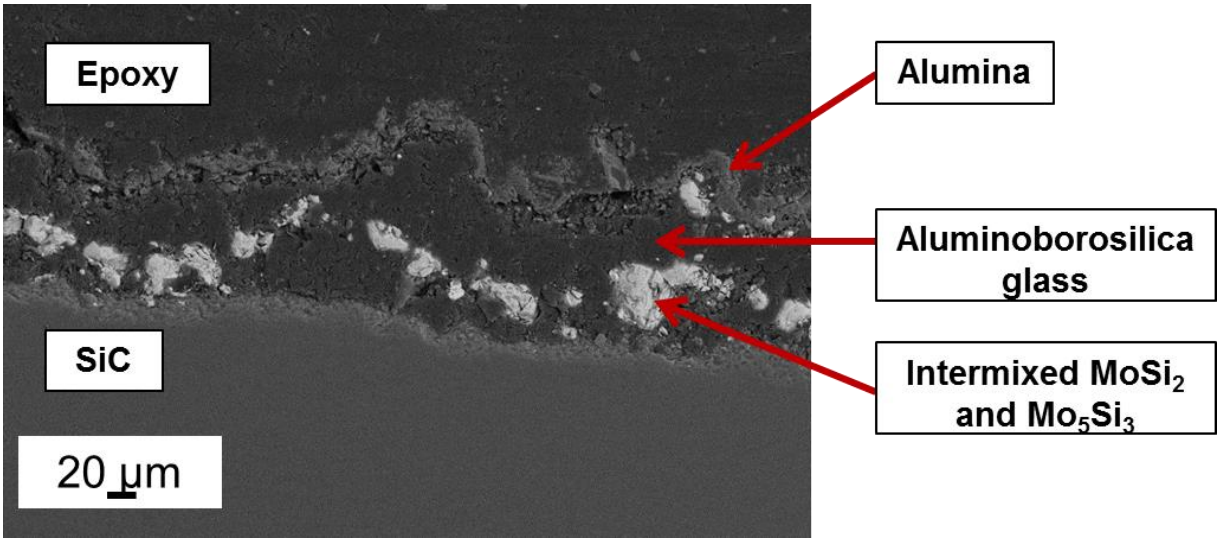

Fig. 21 Cross-sectional backscattered SEM image of Mo-Si-B + 5 wt% Al coated CVD SiC after exposure to 100 ppm O_2/balance Ar flowing at 100 mL/min at 1400°C for 4 hours.

Thus the enhanced Al/Al_2O_3 content of the external aluminoborosilica glass produced by the Mo-Si-B + 5 wt% Al coating appears to suppress interfacial reaction between SiC and SiO_2 to become sluggish, providing experimental proof for the thermodynamic evidence that the addition of alumina to silica will reduce the activity of Si in the silicate. That is, the proposed chemical reaction between SiC and SiO_2 to produce SiO(g) and CO(g) becomes sluggish as the Al_2O_3 content of SiO_2 increases. As indicated by the steady state mass loss rate of $9x10^{-6}$ mg/mm^2-min there is certainly still some formation of gaseous products; however, it is an order of magnitude slower than the mass loss rate observed with the oxidized CVD SiC (mass loss rate: ~$3x10^{-5}$ mg/mm^2-min) and Mo-Si-B coated CVD SiC (mass loss rate: ~$5x10^{-5}$ mg/mm^2-min) samples.

Multiphase Solidification of Mo-Nb-Si-B Alloys

Multiphase Mo-Nb-Si-B cast alloys are potential candidates for application in jet turbine engines due to their superior creep properties and adequate oxidation resistance at ultrahigh temperature above 1200 C. In order to satisfy several application requirements , it is required to control multiphase solidification microstructure of (Nb,Mo)-bcc, (Mo,Nb) Si -T and (Mo,Nb) SiB -T in the Mo-Nb-Si-B quaternary alloys..In the present study, in order to understand the mechanism of a threephase eutectic reaction in the Mo-Nb-Si-B quaternary system, the crystallography of the bcc/T /T three-phase eutectic microstructure has been examined in directionally solidified alloys. The directional solidification was conducted on a Mo-32.2Nb-19.5Si-4.7B (at.%) alloy using an optical floating zone (OFZ) furnace in a flowing Ar gas atmosphere at a constant growth rate of 10 mm/h. The microstructure was observed by SEM. The orientation of the constitute phases was analyzed by EBSD (fig. 22) The microstructure of the directionally solidified alloys is characterized by elongated T phase regions surrounded by inclusions of the bcc and T phases with an interwoven morphology. The T grains in eutectic cells

are faceted on the (001) planes and elongated along the [110] direction. The T phase has an orientation relationship of (001) // (011) and [130] // [2-11] with the bcc phase, whereas no particular orientation relationships were detected for the T phase with the bcc and T phases. These crystallographic features of bcc/T /T three-phase eutectic microstructure suggest that the primary T phase crystallizes and grows along the [110] direction in liquid phase, followed by nucleation of the bcc phase on the interface between T and liquid phases, resulting in a final bcc/T two-phase eutectic reaction surrounding the elongated T phase. The microstructure and crystallographic features have also been examined in the as-cast three-phase eutectic Mo-Nb-Si-B alloy prepared by arc-melting. . From the evaluation of the microstructures in arc cast ingots at a constant 32.6 at%Nb the path of the liquidus valleys has been determined that establishes the solidification reaction as a eutectic. The incorporation of the experimental results into a computational thermodynamic analysis provides insight on the partitioning of components within each phase during solidification. . The identification of the multiphase eutectic reaction to yield the $(Mo,Nb)_{ss}$ + T_1 + T_2 interwoven morphology establishes solidification as a potential processing method.

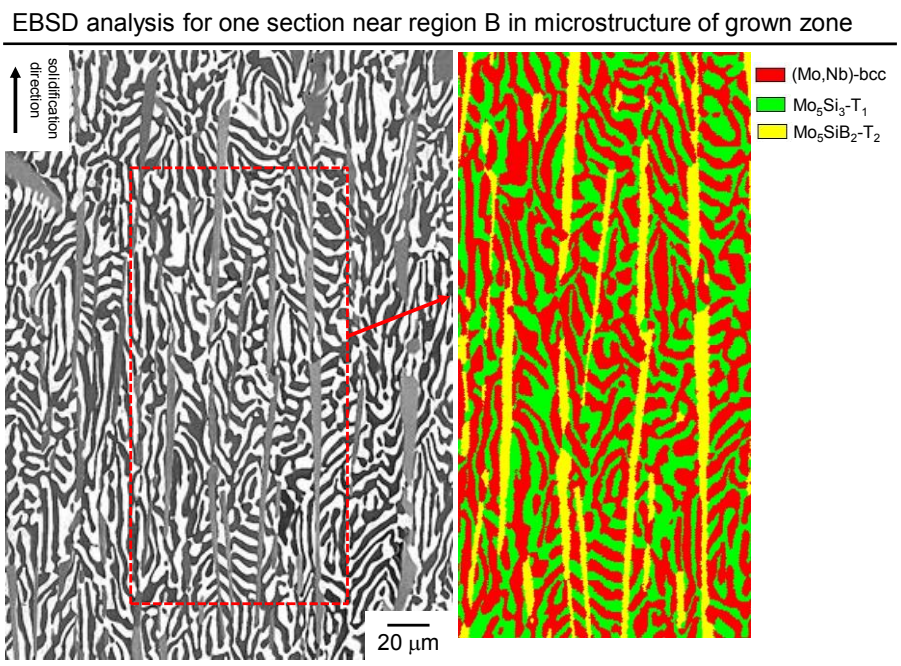

Fig. 22 EBSD analysis of directionally solidified sample illustrating the three phase microstructure.

Control of Si Solubility in Mo

In the Mo-Si-B system three phase alloys based upon the co-existence of a Mo_{ss} solid solution phase, the Mo_5SiB_2, T_2 phase and a Mo_3Si phase have demonstrated exceptional high temperature creep strength and useful inherent oxidation resistance that can be enhanced by coating designs. However, as is common with many Mo based alloys, the ambient temperature

ductility is limited. The origin of the limited ductility has been debated in the literature with different mechanisms ranging from extrinsic grain boundary embrittlement due to segregation of impurities to intrinsic characteristics due to the difficulty in dislocation slip. In the case of Mo-Si-B alloys it has been reported that the Si content in the Mo_{ss} phase causes extensive work hardening and contributes to the limited ductility.

Based upon this background we have started to examine strategies to reduce the Si solubility in the Mo_{ss} phase with suitable minor alloying additions that do not change the basic multiphase microstructure. One approach is based upon adding a minor solute component that has a high affinity for Si. In another approach we have employed solutes that are known to affect the lattice parameter of Mo. In the preliminary work we have measured lattice parameters for alloys after equilibration at 1800°C. In binary Mo-Si alloys increasing the Si content decreases the lattice parameter of Mo_{ss}., a_0(Mo) At low addition levels up to 1 at.% in Mo-Si-B alloys Cr and Y decrease a_0(Mo) while Ti and Hf increase a_0(Mo). The increase in a_0(Mo) is understandable since the atomic volumes of Ti (10.64 A^3) and Hf (13.42 A^3) are larger than that for Mo (9.41 A^3). Similarly the small atomic volume for Cr (7.78 A^3) would be expected to decrease a_0(Mo), but the decrease in a_0(Mo) with the addition of Y with a large atomic volume (19.89 A^3) is opposite to the trend expected based on atom size.

Evidence for interstitial and substitutional Si point defects in Mo (ss)

In order to control the solubility of Si with in the Mo(ss) phase of Mo-Si-B alloys Ce or Y were added to the alloy during fabrication. Both Ce and Y formed a new Re_5Si_3 phase. The Ce_5Si_3 shows to be insoluble with Mo silicides and would segregate to the top of the alloy during arc melting. The Y_5Si_3 proved to be very soluble with Mo silicides. However neither additions lowered the solubility of Si in the Mo(ss) phase. It was discovered however that with the additions of Y the lattice parameter could be increased while keeping the concentration of silicon near the same as non-yttrium containing samples. This gives rise to the idea that there are two locations for Si to form with in the BBC phase. The first and most assumed is in a substitutional location. The second is an interstitial location. For the Mo(ss), the interstitial location is most likely a split dumbbell defect along the [110] direction (fig. 23). This defect has been modeled extensively in pure Mo systems and offers the lowest energy requirements of other interstitial possibilities.

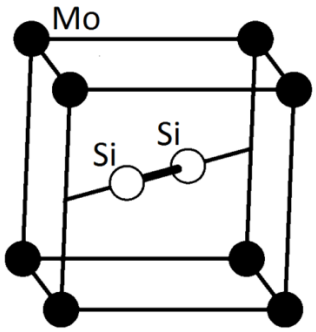

Fig. 23 Split dumbell interstitial configuration.

DISTRIBUTION A: Distribution approved for public release.

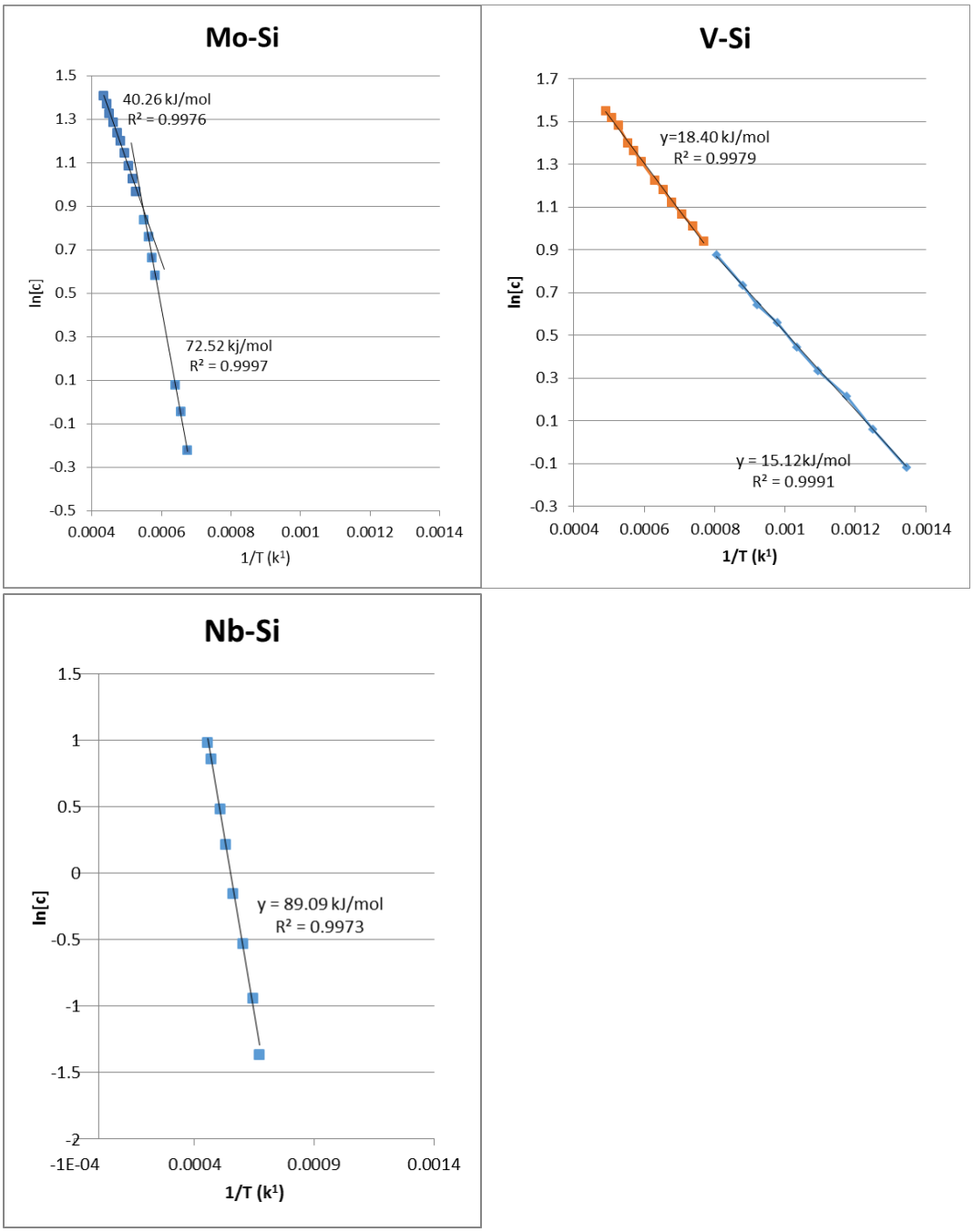

Fig. 24 Arrhenius plots of Mo(ss), V(ss) and Nb(ss) with Si.

An Arrhenius plot of the maximum solubility also shows evidence of multiple locations where Si can be located.. In smaller atom size BCC metals Si is known to form substitutional while in larger BCC metals Si will form interstitially. Comparing the Arrhenius plots of Cr and Nb it can be seen that steeper slopes will correspond to interstitial locations while shallower slopes correspond to substitutional locations.

An ab-initio model was constructed to gain understanding of the formation energy of possible defect locations. The zero point of the ab-initio energy was set at the BCC Mo cell with no defects. The formation energies for all defects, except for substitutional defects, show a very high energy formation (fig. 25). This leads to the belief that only substitutional defects will be present. At present there is a disagreement between known and accepted phase diagrams of the Mo-Si system and first principle ab-initio results.

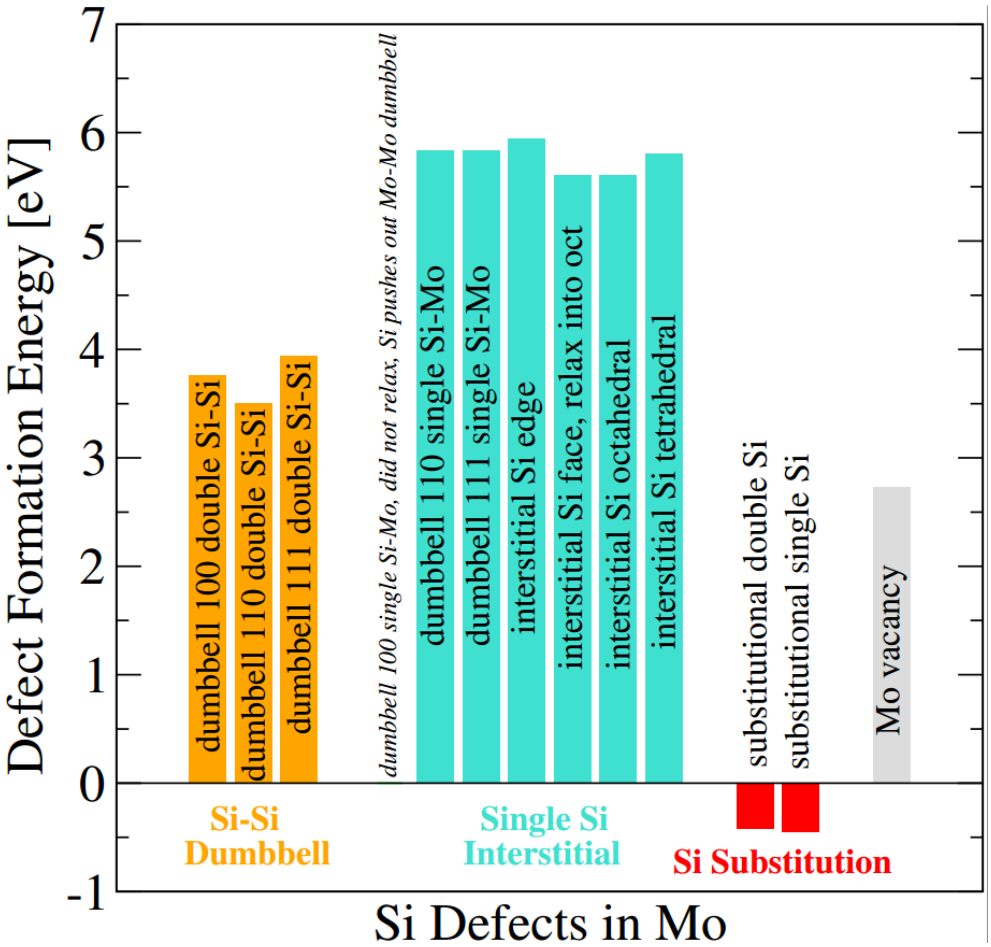

Fig. 25 Plot of formation energies from ab-initio calculation of Mo(ss)

<u>Dislocation Energetics and Deformation Behavior of Mo_5SiB_2</u>

In order to complete the analysis we have decided to add additional calculations for other slip planes observed in T_2. More specifically, we also consider (012)plane with [100], [012] and [221] slip vectors, and (110) plane with [001] and [100]. With these additions the analysis should essentially cover all observed slip systems. These are more complex planes, and we had some difficulties calculating them at first. Now we have been able to overcome the difficulties, and we are finishing the calculations. The preliminary results indicate that [100](012) and [001](110)

DISTRIBUTION A: Distribution approved for public release.

slips can also operate with similar or somewhat higher stacking fault energies in addition to the ones that were previously considered.

Soft boride phase

Due to the difficulty of restricting Si in the Mo(ss) phase an alternate method was explored. It was found that the metastable Mo_3B_2 phase could be alloyed with up to 40 at. % Hf (fig. 26) . This phase has shown to have a hardness of <900 kgf/mm^2 making it softer than hardened steel. If this phase also has high Young's modulus similar to all borides, the fracture toughness of this phase will be high enough to ensure crack termination. This boride also has no solubility with Si, so that it can alleviate the solution hardening and embrittlement due to Si.

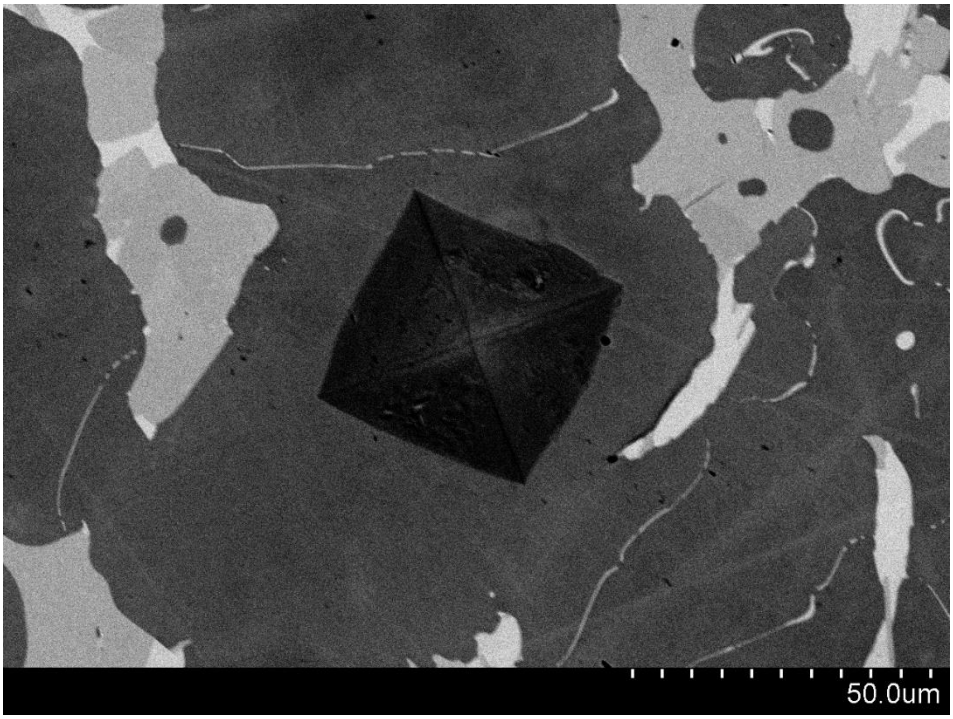

Fig. 26 Soft boride with the formula $(Mo_{1-x}Hf_x)_3B_2$; x=30

1) Publications

1. J.H. Perepezko and R. Sakidja "Mo-Si-B Alloys for Ultra-High Temperature Applications", Japan Inst. Metals-123 High Tempeature Resistant Metallic Materials Committee Report: Advanced High Temperature Materials, 53, No. 1, 39-49 (2012).

2. N. Sekido, K. Hildal, R. Sakidja and J.H. Perepezko, Stability of the Nb5Si3 phase in the Nb-Mo-Si system, Intermetallics, **41**, 104-112 (OCT 2013)

DISTRIBUTION A: Distribution approved for public release.

3. J.H. Perepezko, Mo-Si-B Alloys for Ultra-High Temperature Applications , 18th Plansee Seminar 2013, Eds. L.S. Sigl, H. Kestler and J. Wagner, (Plansee, Ruette, Austria) RM24/1-15 (2013).

4. P.J. Ritt, P.A. Williams, S.C. Splinter, J.H. Perepezko, "Arc jet testing and evaluation of Mo–Si–B coated Mo and SiC–ZrB_2 ceramics," Journal of the European Ceramic Society 34 [15] 3521-33 (2014)

5. 5.J.H. Perepezko, B.A. Pint and D. R. Forrest, Structural Intermetallics**:**Alloy Design, Processing, and Applications, Adv. Mat. and Proc., 22-25, Sept. 2014.

6. N.I. Medvedeva, O.Y. Kontsevoi, A.J. Freeman, and J.H. Perepezko, Deformation behavior of Mo_5SiB_2, Phy. Rev. B (under revision)

7. N. Takata, N. Sekido, M. Takeyama and J. H. Perepezko, Crystallography of Bcc/T_1/T_2 Three-Phase Microstructure in the Directionally Solidified Mo-Nb-Si-B Alloy, MRS Proceedings, **1760** (2015), mrsf14-1760-yy03-03.

8. N. Takata , N. Sekido , M. Takeyama , J.H. Perepezko , M. Follett-Figueroa, and C. Zhang, Solidification of Bcc/T_1/T_2 Three-Phase Microstructure in Mo-Nb-Si-B Alloys, submitted to Intermetallics

9. Environmental Resistance of Mo-Si-B Alloys and Coatings J. H. Perepezko, T. Sossaman, P. Ritt, I. Downs (in preparation).

2) <u>Presentations</u>

1. "Experimental and Theoretical Stability Assessment in Mo-rich Mo-Si-B Ternary System", Sungtae Kim, <u>Ridwan Sakidja</u>, John Perepezko, Materials Science & Technology 2012, Oct 2012 Pittsburgh Pa
2. J. H. Perepezko "High Temperature Mo-Si-B Alloys: Phase Stability and Oxidation Performance" Beyond Nickel-Based Superalloys ECI Conference Bad Berneck, Germany, May 13-17, 2013
3. J. H. Perepezko, "Mo-Si-B Alloys for Ultra- High Temperature Applications" 18th Plansee Seminar 2013 International Conference on Refractory Metals and Hard Materials Reutte, Austria, June 3-7, 2013
4. J. H. Perepezko, High Temperature Mo-Si-B Alloys: Phase Stability and Oxidation Performance, (invited) Thermec'2013, Las Vegas, NV, December 2-6, 2013.
5. P.J. Ritt, J.H. Perepezko, "Oxidation of the Mo-Si-B Based Coating in Oxygen Deficient Environments," The Second International Education Forum on Environment and Energy Science, Huntington Beach, CA, December 13-17, 2013

DISTRIBUTION A: Distribution approved for public release.

6. Multiphase Microstructures and Stability in High Temperature Mo-Si-B Alloys (invited), J.H. Perepezko,: 2014 TMS Annual Meeting & Exhibition, Symposium: Materials for High-temperature Applications: Next Generation Superalloys and Beyond,
7. P.J. Ritt, J.H. Perepezko, "Oxidation of the Mo-Si-B Based Coating in Oxygen Deficient Environments," The Minerals, Metals & Materials Society Annual Meeting, San Diego, CA, February 16-20, 2014
8. J.H. Perepezko, T. Sossaman, P.J. Ritt, "High-Temperature Oxidation of Mo-Si-B Alloys and Coatings," International Symposium on High-temperature Oxidation and Corrosion, Hakodate, Hokkaido, Japan, June 23-27, 2014
9. High Temperature Environmental Resistance of Mo-Si-B Alloys and Coatings J. H. Perepezko, T. Sossaman, P. Ritt, I. Downs, Thermal Barrier Coatings IV, Kloster Irsee Irsee, Germany, June 22-27, 2014
10. Environmental Resistance of Mo-Si-B Alloys and Coatings J. H. Perepezko, T. Sossaman, P. Ritt, I. Downs, International Workshop on Advanced Structural Materials Tohoku University, Sendai, Japan, July 31-August 2, 2014
11. Crystallography of the BCC/T1/T2 Eutectic in Mo-Nb-Si-B Alloys, N. Takata, N. Sekido, M. Takeyama and J. H. Perepezko, The Minerals, Metals & Materials Society Annual Meeting, Orlando, FL, March 2015.

Personal

Professor John H. Perepezko, PI
Patrick Ritt, Graduate student, Completed PhD in August 2015
Michael Follett-Figueroa, graduate student

DISTRIBUTION A: Distribution approved for public release.

Chemical Physics Letters 577 (2013) 16–21

Contents lists available at SciVerse ScienceDirect

Chemical Physics Letters

journal homepage: www.elsevier.com/locate/cplett

First measurement of the BO $B\ ^2\Sigma^+$ radiative lifetime by laser-induced fluorescence via the $B\ ^2\Sigma^+$–$X\ ^2\Sigma^+$ transition

Jason D. White, Jochen Marschall *, Richard A. Copeland

Molecular Physics Laboratory, SRI International, 333 Ravenswood Avenue, Menlo Park, CA 94025, United States

ARTICLE INFO

Article history:
Received 29 March 2013
In final form 12 May 2013
Available online 27 May 2013

ABSTRACT

Observation of the temporal evolution of the fluorescence following laser excitation of boron monoxide molecules to the $B\ ^2\Sigma^+$ state is used to extract the radiative lifetime and collisional removal rate constant with N_2 as the colliding partner. The two lowest vibrational levels in the ^{11}BO $B\ ^2\Sigma^+$ state are examined. The radiative lifetimes are 101 ± 8 ns for $\upsilon' = 0$ and 108 ± 8 ns for $\upsilon' = 1$. The rate constant for collisional removal of B-state $\upsilon' = 0$ ^{11}BO molecules by N_2 is $(1.1 \pm 0.1) \times 10^{-11}$ cm^3 s^{-1}.

© 2013 Elsevier B.V. All rights reserved.

1. Introduction

The oxidation of solid boron is extremely exothermic and potentially offers large advantages in gravimetric and volumetric efficiencies over hydrocarbon-based fuels for missile propellants [1]. This potential has led to numerous studies of the surface and gas-phase chemistry of boron combustion processes [2–7]. The boron monoxide (BO) radical is a key intermediate in boron combustion processes [4,8,9]. Boron monoxide is also an important volatile product appearing in the boundary layers of high-enthalpy flows interacting with diboride-based thermal protection materials [10]. The oxidation of boron species in combustion [5–7] or plasma environments [10] leads to the production of electronically-excited BO and boron dioxide (BO_2) molecules and strong blue-green visible emission associated with the BO ($A\ ^2\Pi$–$X\ ^2\Sigma^+$) and the BO_2 ($A\ ^2\Pi_u$–$X^2\Pi_g$) systems.

The two lowest-lying electronically excited states of the BO molecule, $A\ ^2\Pi$ and $B\ ^2\Sigma^+$, lie 2.96 and 5.35 eV above the ground state, respectively [11]. The B state has allowed radiative transitions to both the A and X states. The emission from the B–X system occurs in the ultraviolet, whereas the emission from B–A system occurs at visible wavelengths. Both excited $A\ ^2\Pi$ and $B\ ^2\Sigma^+$ states can be generated by gas-phase chemistry in discharge-activated gas flows seeded with various boron and oxygen species–an approach that has been used by a number of investigators to produce A-X (or α-band) and B-X (or β-band) emission for spectroscopic analysis [11–15]. The combination band system B–A is weak, and its emissions overlap with the much stronger A–X emissions in the visible [12]. Observation and characterization of B–A emission in a discharge source has apparently been reported only once, by Mulliken [12], who noted, 'All the bands of the new system are very weak as compared with like-numbered α and β bands.'

In 1980, Clyne and Heaven [16] reported a laser-induced fluorescence (LIF) study of BO via the A–X transition and obtained excitation spectra of the (υ',0) bands for $\upsilon' \leqslant 11$. They determined an A-state radiative lifetime of 1.78 ± 0.14 μs for $\upsilon' = 0$ and found no significant dependence of lifetime on υ' for $\upsilon' = 0$, 4, 7, 9, 10, and 11. Clyne and Heaven reported an averaged lifetime value of 1.76 ± 0.13 μs for these six vibrational levels. Subsequently, Hinchen [17] used LIF to measure the collisional removal rate constants for BO in the $\upsilon' = 0$ and 2 levels of the A state by He, Ar, O_2, N_2, NO, NO_2, N_2O, F_2, and CF_4, and found the A-state radiative lifetimes to be 1.75 μs for $\upsilon' = 0$ and 1.37 μs for $\upsilon' = 2$. These two studies are in stark contrast to an earlier LIF measurement using a broad bandwidth excitation source (~16 cm^{-1}) by Huie et al. [18], which yielded lifetime values for the A $\upsilon' = 1$ and $\upsilon' = 2$ states about an order of magnitude shorter and most likely in error [16]. Llewellyn et al. [19], Stanton et al. [20], Oldenborg and Baughcum [21], and Belyung et al. [22] have used LIF in the $A\ ^2\Pi$–$X\ ^2\Sigma^+$ system to study the reaction of BO with O_2.

While there have been numerous studies using LIF in the A state, no studies have employed LIF in the B electronic state. Laser excitation to the B state and fluorescence collection in the ultraviolet has the potential to be a useful diagnostic for *in situ* detection of BO in plasmas, flames, and reactive boundary layers, since ultraviolet fluorescence detection avoids the strong visible emissions from BO and BO_2 commonly seen in these environments. Here, we report the first measurements of the radiative lifetimes and collisional removal rate constants for the $\upsilon' = 0$ and $\upsilon' = 1$ levels of ^{11}BO B state, as determined by laser excitation via the (0,0) and (1,0) bands of the B–X system [(υ',υ'')].

2. Experimental

Boron monoxide was produced in a flowing discharge system by mixing trace amounts of boron trichloride (BCl_3) into a partially-dissociated nitrogen flow that was titrated below the N-atom

* Corresponding author.
E-mail address: jochen.marschall@sri.com (J. Marschall).

0009-2614/$ - see front matter © 2013 Elsevier B.V. All rights reserved.
http://dx.doi.org/10.1016/j.cplett.2013.05.028

DISTRIBUTION A: Distribution approved for public release.

endpoint with nitric oxide (NO) as described by Clyne and coworkers [16,19]. The titration reaction

$$N + NO \rightarrow O + N_2 \quad (1)$$

is very fast, with a room temperature rate constant [23] of 3×10^{-11} cm^3 s^{-1} and allows control of the O-atom to N-atom ratio in the flow up to the endpoint where all nitrogen atoms are consumed. The reaction sequence leading to the formation of BO is thought to involve the sequential stripping of chlorine from BCl_3 by atomic oxygen [16]. The absence of significant O_2 concentrations in the gas-phase minimizes the rapid reaction

$$BO + O_2 \rightarrow BO_2 + O \quad (2)$$

that has a room temperature rate constant [20–22] of 1 to 2×10^{-11} cm^3 s^{-1}.

Figure 1 shows the layout of the experimental setup. The gases N_2 (BIP ultra-high purity, <100 ppb contamination), NO (99.5%), and a 5% BCl_3/N_2 mixture (99.999%) were introduced into the quartz reactor using electronic mass flow controllers calibrated in standard cubic centimeters per minute (sccm). Nitrogen dissociation was achieved using a microwave discharge (Opthos, 2.45 GHz) operated at 90 W. Gas pressures were measured using 1 and 10 Torr capacitance manometers (MKS Baratron) that had previously been zeroed under high vacuum ($\sim 10^{-6}$ Torr) conditions. Pressure measurement uncertainty does not exceed ±0.5%. All experiments were performed at room temperature.

To ensure good mixing, NO was added downstream of the discharge through a small glass capillary protruding into the center of the flow tube. The BCl_3/N_2 mixture was added downstream of the titration port through a retractable injector aligned with the flow tube centerline about 10 cm upstream of the detection region. The mass flows of NO and the 5% BCl_3/N_2 mixtures ranged from 0.08 to 0.36 sccm and 0.2 to 5.3 sccm, respectively. The main N_2 mass flow was varied over a much larger range from 38 to over 1800 sccm, and the cell pressure changed correspondingly from about 0.3 to 7 Torr. Under all test conditions, we operated below the titration endpoint.

Most measurements were performed at an O-atom to BCl_3 ratio around 9, where the addition of BCl_3 to the flow generated a strong blue chemiluminescence. An optical spectrometer (Newport OSM-100-UV-NIR) was used to disperse this blue light and confirm its origin as the BO *A*–*X* system by comparison with simulated spectra computed with the PGOPHER program [24]. The spectroscopic constants of Mélen et al. [11] for the *X*, *A*, and *B* electronic states of the ^{11}BO and ^{10}BO isotopomers were used. Frank–Condon factors for the *A* (υ' = 0–13)–*X* (υ'' = 0–22) and the *B* (υ' = 0–13)–*X* (υ'' = 0–14) transitions were taken from Liszt and Hayden-Smith [25]. A more limited range of Frank–Condon factors from Nicholls et al. [26] was used for the *B* (υ' = 0–5)–*A* (υ'' = 0–5) transitions. No emissions associated with the *B*–*X* or *B*–*A* systems could be identified in the experimental spectra.

Laser excitation at the appropriate ultraviolet (UV) wavelengths in the 226–233 nm range was produced by frequency tripling the tunable red light output of a Quanta-Ray PDL-1 dye laser operated with LDS-698 laser dye dissolved in methanol and pumped at 532 nm with the second harmonic output of a Quanta-Ray DCR-3 Nd:YAG laser. Two beta-barium borate crystals (BBO-2 37.4° and BBO-1 53.2°, respectively) were used for first frequency doubling and then frequency mixing to generate the UV light. A Galilean telescope was used to down-collimate the UV excitation beam by a factor of ~4 and the beam was directed through quartz Brewster angle windows into and out of the reactor.

The UV laser pulse energy exiting the reactor was monitored with Molectron J3-09 energy meter. Laser beam size measurements showed that 95% of the pulse energy was contained in a beam area of approximately 0.4 mm^2. The typical energy delivered to the excitation volume during a nominal 6 ns laser pulse was ~300 μJ, with a corresponding average fluence of ~1.2 W mm^{-2}.

Fluorescence was collected at right angles to the excitation beam by a gated Hamamatsu 636 photomultiplier tube (PMT). The PMT was fit with a Schott Glass UG11 filter in series with a 265 ± 7.5 nm notch filter, a combination designed to block laser excitation wavelengths below 240 nm and capture fluorescence from the B (υ' = 0) → X (υ'' = 2–4) and B (υ' = 1) → X (υ'' = 3–4) bands. The peak transmittance of this filter combination is only about 4% and less than 1% of the total fluorescence from either the B (υ' = 0) or B (υ' = 1) levels is collected. The fluorescence collection efficiency for the B (υ' = 1) level is about 30% higher for than for the B (υ' = 0) level.

The Nd:YAG laser was triggered at 10 Hz using a Stanford Research Systems (SRS) DG535 digital delay generator, which was also used to time the opening of the PMT gate. A fast photodiode was used to capture residual red dye light and trigger the data acquisition system. The PMT signals were amplified by a factor of

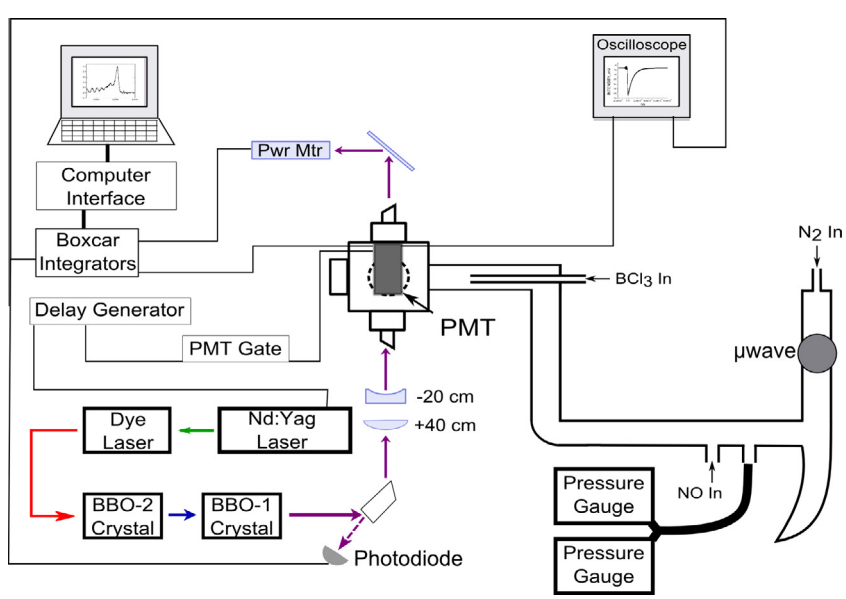

Figure 1. Experimental setup.

DISTRIBUTION A: Distribution approved for public release.

5 using an SRS 240 preamplifier. For excitation spectra, the dye laser was scanned at 0.01 nm s^{-1} and the amplified signals were averaged over a gate width of 120 ns by SRS 250 boxcar integrators. For lifetime measurements, the amplified PMT signals were collected directly by a Lecroy Waverunner 204-WXi, 2 GHz digital oscilloscope. The LIF waveforms produced by 1000 laser shots were averaged to give a representative decay curve for each test condition.

3. Results and discussion

Figure 2 shows an experimental excitation spectrum over the 233.40 to 233.10 nm wavelength range (top panel) and a corresponding PGOPHER spectral simulation (bottom panel). The experimental spectrum is seen to arise from the BO $B \leftarrow X$ (0,0) bands. The isotope ratio of ^{11}B to ^{10}B is about 4 to 1 [27] and the spectra are dominated by the ^{11}BO $B \leftarrow X$ (0,0) band contributions. The ^{10}BO $B \leftarrow X$ (0,0) band head lies at 42874.68 cm^{-1}, and the ^{11}BO $B \leftarrow X$ (0,0) band head lies at 42882.31 cm^{-1}.

The individual P- and R-branch transitions of the ^{11}BO $B \leftarrow X$ (0,0) band are labeled in Figure 2 by their total angular momentum quantum number N. Angular momentum coupling in the $B\ ^2\Sigma^+$ electronic state falls into Hunds' case (b). For $^2\Sigma^+$, the state quantum number $\Lambda = 0$, thus N, the angular momentum of nuclear motion, and K, the total angular momentum apart from spin, are equal. Selection rules for this state dictate that $\Delta N = \pm 1$. Rotational transitions are labeled by their lower state N value. The spin splitting for each sublevel is small and within the bandwidth of the laser system. Similar excitation scans and simulations were performed in the BO $B \leftarrow X$ (1,0) band to identify specific rotational transitions.

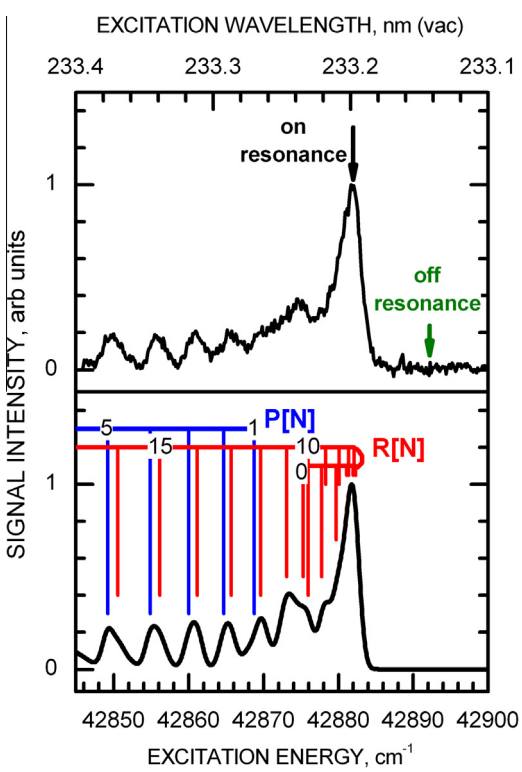

Figure 2. Top panel: experimental LIF excitation spectrum over the 233.40–233.10 nm wavelength range at a nitrogen pressure of 0.57 Torr; $B \rightarrow X$ ($\upsilon' = 0$, $\upsilon'' = 2$, 3, 4) fluorescence collected with a combination of UG11and 265-nm bandpass filters. Excitation wavelengths used for $B \rightarrow X$ fluorescence decay and background measurements are indicated as 'on-resonance' and 'off-resonance'. Bottom panel: simulated spectrum for BO (1.8 cm^{-1} resolution, highly saturated) and the rotational assignments of the transitions for the ^{11}BO isotope.

The rotational features in the excitation scan of Figure 2 are likely saturated and power broadened. A spectral resolution of about 1.8 cm^{-1} is required for a reasonable simulation of the experiment. Measurements of LIF intensity versus pulse energy, performed by pumping the tightly spaced R[3-7] transitions at the ^{11}BO $B \leftarrow X$ (0,0) band head, confirm that excitation is not linear even at laser pulse energies 20 times less that typically used in the measurements.

In our measurements, we have targeted the ^{11}BO isotope. The majority of fluorescence decay curves for the ^{11}BO B ($\upsilon' = 0$) state were acquired as a function of nitrogen pressure by pumping the R[3-8] transitions at 233.201 nm, labeled 'on-resonance' in Figure 2. These transitions are about 7.6 cm^{-1} to the blue of the ^{10}BO $B \leftarrow X$ (0,0) band head and so are free from any ^{10}BO interference. To account for unwanted contributions in the LIF signal from scattered laser light, window fluorescence, and chemiluminescence in the reaction zone, additional background measurements were performed at a wavelength of 233.145 nm where no BO excitation is expected or observed for either boron isotope. This position is labeled 'off-resonance' in Figure 2. Examples of on- and off-resonance LIF measurements are shown in Figure 3a for an N_2 pressure of 0.57 Torr.

Background-subtracted fluorescence decay curves were fit with a single exponential function of time of the form

$$I = a\exp(-t/\tau_{\text{eff}}) + b \tag{3}$$

beginning at the peak fluorescence intensity and extending (at least) to the time where the intensity dropped to <1% of its peak value. For all data collected below 0.5 Torr, the correlation coefficients of the fits exceeded 0.95; above this pressure, the correlation coefficients typically exceeded 0.99. Figure 3b shows the background-subtracted fluorescence data of Figure 3a on a log scale, along with an exponential fit yielding an effective fluorescence lifetime of 102 ns.

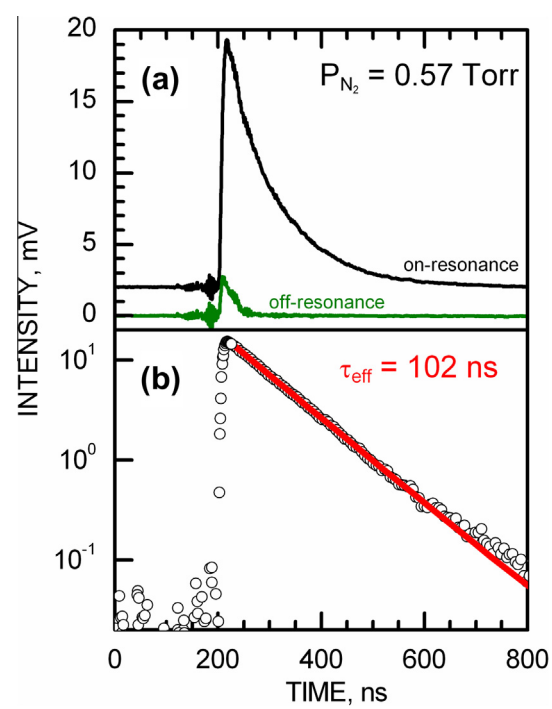

Figure 3. (a) Experimental fluorescence signal (on-resonance with ^{11}BO) and background (off-resonance) at a nitrogen pressure of 0.57 Torr. (b) Background-subtracted fluorescence decay (open circles) and the exponential fit (solid line) used to extract an effective fluorescence lifetime of 102 ns (decay constant of 9.80 μs^{-1}).

DISTRIBUTION A: Distribution approved for public release.

A similar procedure was carried out in additional B ($\upsilon' = 0$) fluorescence decay measurements exciting the more isolated (0, 0) band P[11] transition to $N' = 10$ (on-resonance at 233.626 nm; off-resonance at 233.649 nm) and to measure fluorescence decay constants for the B ($\upsilon' = 1$) state by pumping the P[13] transition $N' = 12$ in the (1,0) band (on-resonance at 227.055 nm; off-resonance at 227.082 nm). The selection of the specific features for excitation was influenced by NO LIF features also present in this wavelength region.

Figure 4 summarizes our decay constant (i.e., τ_{eff}^{-1}) measurements on a Stern–Volmer plot for the electronically excited states prepared as described for Figure 2. The measurements cover a pressure range from about 0.3 to 7 Torr. Below this pressure range, the LIF signal-to-noise was insufficient for fitting and above this range the gas flows and the microwave discharge were difficult to stabilize.

The B ($\upsilon' = 0$) decay constants measured by pumping the P[11] transition to $N' = 10$ (open triangles in Figure 4) overlap with measurements made by pumping the R[3–7] transitions to $N' = 4$-8 (closed squares in Figure 4), suggesting no rotational level dependence of B-state lifetime or collisional removal in these experiments. Although there is some overlap of data points at low pressures, the fluorescence decay rate for the $\upsilon' = 1$ level clearly falls below that of the $\upsilon' = 0$ level for all nitrogen pressures.

Because the $\upsilon' = 0$ and 1 levels of the B state lie about 3 eV below dissociation limit [28] and about 7.5 eV below the ionization limit [29], depopulation by predissociation or ionization is not important. The fluorescence decay constant for a given temperature and vibrational level can be approximated as a linear function of nitrogen pressure as

$$\tau_{\text{eff}}^{-1} = \tau_{\text{rad}}^{-1} + k_{N_2} P_{N_2} \quad (4)$$

where P_{N_2} is the N_2 pressure in Torr. In our experiments, N_2 is always in excess of all other gas species present through either microwave dissociation, titration with NO, or reaction with BCl_3 by more than 2 orders of magnitude. Therefore only collisional deactivation by N_2 is included in the data analysis. Figure 4 shows linear least squares fits of Eq. (4) to the decay constant data. The radiative lifetime of the B state (τ_{rad} in μs) is determined from the inverse of the zero pressure intercept, and the apparent rate constant for collisional deactivation of the B state by N_2 (k_{N_2} in $\text{Torr}^{-1}\ \mu\text{s}^{-1}$) is determined from the slope.

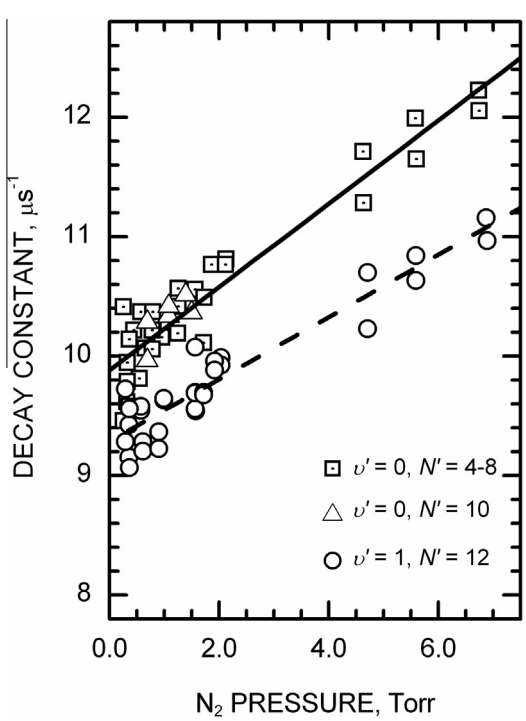

Figure 4. Experimental fluorescence decay constants versus nitrogen pressure for the $\upsilon' = 0$ level (squares and triangles) and $\upsilon' = 1$ level (circles) of the ^{11}BO $B\ ^2\Sigma^+$ state. Linear least squares fits for each vibrational level are shown by the fitting lines.

We discuss the $\upsilon' = 0$ results first. The linear fit to the $\upsilon' = 0$ data yields an intercept of $9.88 \pm 0.06\ \mu\text{s}^{-1}$ and a slope of $0.349 \pm 0.022\ \text{Torr}^{-1}\ \mu\text{s}^{-1}$, where the fitting uncertainties are about 6% for the slope and less than 1% for the intercept. The uncertainties associated with the measurement of pressure and the fitting of Eq. (3) to experimental fluorescence decay curves are less than 1% for each decay constant plotted in Figure 4. Therefore, including error weighting in the least-squares fitting of the decay constant data with Eq. (4) has negligible effect on extracted intercept and slope values.

We note that the scatter between individual decay constant measurements is much higher than 1%, indicating that experimental reproducibility, rather than pressure measurement or fitting errors, is the more realistic metric for assigning uncertainties. The largest scatter in decay constant values occurs at low pressures near 0.3 Torr, with 2-σ statistical errors of about 7%. We assign similar uncertainties to our values of lifetime and removal rate constants and report a radiative lifetime of 101 ± 8 ns and an apparent nitrogen removal rate constant of $(1.1 \pm 0.1) \times 10^{-11}$ - $\text{cm}^3\ \text{s}^{-1}$ for the ^{11}BO B ($\upsilon' = 0$) level. Here, we have expressed the removal rate constant in more conventional units using the ideal gas law and a room temperature of 298 K. The collisional cross section corresponding to this removal rate is $2.3 \pm 0.2\ \text{Å}^2$.

The fit of Eq. (4) to the $\upsilon' = 1$ data yields an intercept of $9.28 \pm 0.05\ \mu\text{s}^{-1}$ and a slope of $0.261 \pm 0.017\ \text{Torr}^{-1}\ \mu\text{s}^{-1}$. However, in this case, the interpretation of k_{N_2} is complicated by the possibility of collisional transfer to the B ($\upsilon' = 0$) level and the collection of B ($\upsilon' = 0$) → X ($\upsilon'' = 2$–4) emission, which could affect measured fluorescence decays.

To investigate the impact of this process, we constructed a simple kinetic model for the effective fluorescence decay rate as a function of collisional transfer from $\upsilon' = 1$ to $\upsilon' = 0$. The model incorporates the measured radiative lifetime and removal rate constant for the $\upsilon' = 0$ level, the measured radiative lifetime of the $\upsilon' = 1$ level, and the relative fluorescence collection efficiency of our filter combination for emission from the B ($\upsilon' = 1$) and B ($\upsilon' = 0$) levels. Using this model, we can find the 'true' $\upsilon' = 1$ collisional removal rate coefficient that reproduces our measured effective removal rate constant for any given experimental pressure and assumed transfer efficiency.

In the lower limit of no collisional transfer from $\upsilon' = 1$ to $\upsilon' = 0$, our measured effective removal rate constant is the 'true' value; in the upper limit of 100% collisional transfer from $\upsilon' = 1$ to $\upsilon' = 0$, the 'true' removal rate constant is almost 3 times higher than the measured value. We find that the computed fluorescence decay curves for all assumed levels of transfer between these two limits are extremely well fit by a single exponential function. Thus, the quality of fit between Eq. (3) and the experimental fluorescence decay curves gives no information on the extent of $\upsilon' = 1$ to $\upsilon' = 0$ transfer.

The model was used to create simulated data sets of effective fluorescence decay constant versus pressure for given transfer efficiency and 'true' collisional removal rate values. We find that the simulated data sets are slightly non-linear functions of pressure for any non-zero transfer efficiency. However, over the pressure range of our experiment, this deviation from linearity is extremely small; it could not be detected within the experimental scatter shown in Figure 4, nor could the quality of the fit between Eq. (4) and the experimental data in Figure 4 give any information

DISTRIBUTION A: Distribution approved for public release.

about $\upsilon' = 1$ to $\upsilon' = 0$ transfer. Linear fits of Eq. (4) to the simulated data sets always generated intercepts and slopes that reproduced the lifetime value input into the model and the measured effective decay constant, respectively.

From these computational exercises, we conclude that the intercept obtained by fitting Eq. (4) to the experimental decay constant data is unaffected by possible $\upsilon' = 1$ to $\upsilon' = 0$ collisional transfer, and we report a B ($\upsilon' = 1$) lifetime of 108 ± 8 ns. However, the slope of the fit cannot be uniquely interpreted, since measured effective fluorescence decay constants can be reproduced by a various combinations of the transfer efficiency and the 'true' collisional removal rate constants. Therefore, we can only report that the collisional removal of B ($\upsilon' = 1$) by nitrogen lies in the range of about $(0.7–2.5) \times 10^{-11}$ cm^3 s^{-1}. More accurate determination of this collisional removal rate constant and the relative contribution of vibrational energy transfer within the B state will require additional wavelength resolved fluorescence experiments.

The expected ratio of A state ($\upsilon' = 0$) to B state ($\upsilon' = 0$) lifetimes is given by

$$\frac{\tau_{\mathrm{rad},A(0)}}{\tau_{\mathrm{rad},B(0)}} = \frac{\overline{\nu}^3_{B(0)}}{\overline{\nu}^3_{A(0)}} \frac{|R_{e,B-X}|^2}{|R_{e,A-X}|^2} \tag{5}$$

where $R_{e,A-X}$ and $R_{e,B-X}$ are the electronic transition dipole moments, and $\overline{\nu}^3_{A(0)}$ and $\overline{\nu}^3_{B(0)}$ are the mean transition energies cubed, given by $\overline{\nu}^3_0 = \sum_{\nu''} q_{0,\nu''} \nu^3_{0,\nu''}$. Using the Frank–Condon factors, $q_{0,\nu''}$, of Liszt and Hayden-Smith [25] and transition energies, $\nu_{0,\nu''}$, calculated from the spectroscopic constants of Melen et al. [11], we compute $\overline{\nu}^3_{B(0)}/\overline{\nu}^3_{A(0)} \cong 10$. The ratio of electronic transition dipole moments for the BO A–X and B–X transitions has not yet been determined, however based on theoretical calculations for the isovalent compounds AlO [30] and BS [31] we expect $R_{e,B-X} > R_{e,A-X}$. Our measured B ($\upsilon' = 0$) state lifetime is about 17 times shorter than the A ($\upsilon' = 0$) state lifetimes reported by Clyne and Heaven [16] and Hinchen [17], and thus consistent with expectation.

Clyne and Heaven [16] could not verify any vibrational level dependence in the their A state lifetime measurements; however, Hinchen [17] found that the lifetime of the $\upsilon' = 0$ level was ~30% longer than that of the $\upsilon' = 2$ level. Within the error bars associated with our measurements, there is a small but discernible vibrational level dependence of the B state lifetimes, with the $\upsilon' = 0$ lifetime being about ~7% shorter than the $\upsilon' = 1$ level lifetime.

Clyne and Heaven [16] could only report an upper limit of 2×10^{-11} cm^3 s^{-1} for the collisional removal of the A state by N_2 because they were unable to detect any systematic changes in effective lifetimes over a limited pressure range from 0.3 to 1.15 Torr. Subsequent measurements of A state removal by N_2 performed by Hinchen [17] resulted in a much lower rate coefficient of 1.24×10^{-13} cm^3 s^{-1}. We find that the B state removal rate by N_2 is almost 100 times faster than Hinchen's value for the A state.

The $\upsilon' = 0$ and $\upsilon' = 1$ vibrational energy levels of the ^{11}BO B state lie 43 812 and 45 073 cm^{-1} above the ground state potential energy minimum, respectively [11]. Using the spectroscopic constants of Benesch et al. [32] for ground state nitrogen, the energetically closest N_2 X (υ') levels are N_2 (21) at 44 014 cm^{-1} and N_2 (22) at 45 730 cm^{-1}. Direct collisional transfer of the ^{11}BO B-state energy into the ground-state vibrational manifold of nitrogen seems unlikely given the endothermic energy defects N_2 X (21)–^{11}BO B (0) = 202 cm^{-1} and N_2 X (22)–^{11}BO B (1) = 657 cm^{-1} and the large vibrational quantum number change from N_2 (0) that would be required.

A more likely explanation for the rapid N_2 removal rates observed is the availability of near-resonant vibrational levels in other electronic states of the ^{11}BO molecule. The B (0) level lies close to $\upsilon' = 28$ level of the X state and the $\upsilon' = 18$ level of the A state. Similarly, B (1) is near the X (29) and A (19) states as well as the $\upsilon' = 0$ level of the $^4\Sigma^+$ state predicted in the computations of Karna and Grein [33] and as yet unobserved.

Shi et al. [34] have computed the vibrational level spacing of the A state up to $\upsilon' = 59$ and the X state up to $\upsilon' = 65$ and obtain reasonable agreement with available experimental measurements up to A ($\upsilon' = 8$) and X ($\upsilon' = 17$) [34]. We add the experimental A state term energy [11] to the level spacing computed by Shi et al. [34] to compare A (υ') with B (υ') energy levels. Computed energy defects are: X (28)–B (0) = 119 cm^{-1}, A (18)–B (0) = 59 cm^{-1}, X (29)–B (1) = 42 cm^{-1}, A (19)–B (1) = −295 cm^{-1}. From the spectral constants given by Karna and Grein, we compute $^4\Sigma^+$ (0)–B (1) = −175 cm^{-1}. These energy defects are all either exothermic or lie well below k_BT (207 cm^{-1}) at room temperature.

It is interesting to compare our results to experiments and computations for the isovalent molecule aluminum monoxide (AlO). The $B\,^2\Sigma^+$ state of AlO molecule has a very similar radiative lifetime around 100 ns with measurements by Johnson et al. [35] (average of 127 ± 4 ns for levels $\upsilon' = 0$, 1, and 2), Dagdigian et al. [36] (100 ± 7, 102 ± 7, and 102 ± 4 ns for levels ($\upsilon' = 0$, 1, and 2), Salzberg et al. [37] (100 ± 17 ns for $\upsilon' = 1$) [37], and Campbell et al. [38] (102 ± 8 ns for $\upsilon' = 1$). The removal of the AlO $B\,^2\Sigma^+$ state by N_2 has been reported as highly ineffective by Johnson et al. [35], who found no change in the fluorescence decay rate with N_2 pressures up to 20 Torr, and Campbell et al. [38], who put an upper limit on the N_2 removal rate constant of 1×10^{-13} cm^3 s^{-1} based on N_2 pressure measurements up to 250 Torr. In contrast, Salzberg et al. [37] report a $\upsilon' = 1$ level N_2 removal rate constant of $(2.00 \pm 0.55) \times 10^{-11}$ cm^3 s^{-1}.

4. Summary

Laser-induced fluorescence in the ^{11}BO $B\,^2\Sigma^+$ state was used to explore the properties of the B-state emission and collisional removal. Radiative lifetimes of 101 ± 8 and 108 ± 8 ns were determined for the $\upsilon' = 0$ and $\upsilon' = 1$ vibrational levels of the B state. The rate constant for N_2 collisional removal of the ^{11}BO B in the $\upsilon' = 0$ level is $(1.1 \pm 0.1) \times 10^{-11}$ cm^3 s^{-1}. The rate constant for N_2 collisional removal of ^{11}BO B in the $\upsilon' = 1$ level is in the range $(0.7–2.5) \times 10^{-11}$ cm^3 s^{-1}. Additional wavelength resolved fluorescence experiments are required to determine the collisional transfer pathways and refine the $\upsilon' = 1$ value.

Acknowledgements

This research was supported by the Aerospace Materials for Extreme Environments Program of the Air Force Office of Scientific Research through contract FA9550-11-1-0201. The US Government is authorized to reproduce and distribute reprints for Governmental purposes notwithstanding any copyright notation thereon. The views and conclusions contained herein are those of the authors and should not be interpreted as necessarily representing the official policies or endorsements, either expressed or implied, of the Air Force Research Laboratory or the US Government.

References

[1] M.K. King, J. Spacecr. Rockets 19 (4) (1982) 294.
[2] W. Zhou et al., Combust. Flame 117 (1–2) (1999) 227.
[3] W. Zhou et al., Symp. (Int.) Combust. 26 (2) (1996) 1909.
[4] R.C. Brown et al., Combust. Flame 101 (3) (1995) 221.
[5] M.J. Spalding, H. Krier, R.L. Burton, Combust. Flame 120 (2000) 200.
[6] S. Yuasa et al., Combust. Flame 113 (1998) 380.
[7] S. Yuasa, H. Isoda, Combust. Flame 86 (1991) 216.
[8] R.A. Yetter et al., Combust. Flame 83 (1–2) (1991) 43.
[9] L. Pasternack, Combust. Flame 90 (3–4) (1992) 259.
[10] M. Playez et al., J. Thermophys. Heat Transfer 23 (2) (2009) 279.
[11] F. Mélen, I. Dubois, H. Bredohl, J. Phys. B: At. Mol. Opt. Phys. 18 (1985) 2423.
[12] R.S. Mulliken, Phys. Rev. 25 (3) (1925) 259.

DISTRIBUTION A: Distribution approved for public release.

[13] J.A. Coxon, S.C. Foster, S. Naxakis, J. Mol. Spectrosc. 105 (2) (1984) 465.
[14] D. Robinson, R.W. Nicholls, Proc. Phys. Soc. 75 (6) (1960) 817.
[15] F.A. Jenkins, A. McKellar, Phys. Rev. 42 (4) (1932) 464.
[16] M.A.A. Clyne, M.C. Heaven, Chem. Phys. 51 (1980) 299.
[17] J.J. Hinchen, J. Chem. Phys. 99 (1993) 4403.
[18] R.E. Huie, N.J.T. Long, B.A. Thrush, Chem. Phys. Lett. 55 (3) (1978) 404.
[19] I.P. LLewellyn, A. Fontijn, M.A.A. Clyne, Chem. Phys. Lett. 84 (3) (1981) 504.
[20] C.T. Stanton, N.L. Garland, H.H. Nelson, J. Phys. Chem. 95 (1991) 8741.
[21] R.C. Oldenborg, S.L. Baughcum, AIP Conf. Proc. 146 (1986) 562.
[22] D.P. Belyung et al., Symp. Int. Combust. 27 (1) (1998) 227.
[23] S.P. Sander, et al., Chemical Kinetics and Photochemical Data for Use in Atmospheric Studies: Evaluation Number 17, Jet Propulsion Laboratory, Pasadena, CA, 2011.
[24] C.M. Western, PGOPHER, a Program for Simulating Rotational Structure, University of Bristol, 2012.
[25] H.S. Liszt, W. Hayden-Smith, J. Quant. Spectrosc. Radiat. Transfer 11 (7) (1971) 1043.
[26] R.W. Nicholls, P.A. Fraser, W.R. Jarmain, Combust. Flame 3 (1959) 13.
[27] K.J.R. Rosman, P.D.P. Taylor, Pure Appl. Chem. 70 (1) (1998) 217.
[28] P. Coppens, S. Smoes, J. Drowart, Trans. Faraday Soc. 64 (1968) 630.
[29] M. Asano, T. Kou, J. Chem. Phys. 20 (10) (1988) 1149.
[30] C. Zenouda et al., J. Mol. Struct. (THEOCHEM) 458 (1–2) (1998) 61.
[31] X. Yang, J.E. Boggs, Chem. Phys. Lett. 410 (4–6) (2005) 269.
[32] W. Benesch, J.T. Vanderslice, S.G. Wilkinson, Astrophys. J. 142 (1965) 1227.
[33] S.P. Karna, F. Grein, J. Mol. Spectrosc. 122 (2) (1987) 356.
[34] D.H. Shi et al., J. Mol. Spectrosc. 264 (1) (2010) 56.
[35] S.E. Johnson, G. Capelle, H.P. Broida, J. Chem. Phys. 56 (1) (1972) 663.
[36] P.J. Dagdigian, H.W. Cruset, R.N. Zare, J. Chem. Phys. 62 (5) (1975) 1824.
[37] A.P. Salzberg et al., Chem. Phys. Lett. 180 (3) (1991) 161.
[38] M.L. Campbell et al., Chem. Phys. Lett. 194 (3) (1992) 187.

DISTRIBUTION A: Distribution approved for public release.

AFOSR Report – University of Vermont

I. Introduction

When the grant started in 2011 the 30 kW ICP Torch Facility at UVM was operational thanks to prior funding from AFOSR (FA9550-08-1-0414) and efforts were underway to exploit the optical access with laser and emission spectroscopic measurements of gas-surface interactions. The work proposed by UVM and SRI International was aimed at making the reactant species (O and N atoms) measurements quantitative and robust, while beginning the large effort to quantify reaction products leaving the surface (O_2, N_2, NO, BO, SiO, CO, CN, ……). Changes in grant management at the time led to the decision by AFOSR to combine this activity with work from material scientists at ISU and UWM. This provided a welcome supply of interesting material samples to test, but such tests came at the expense of the diagnostic development effort. Graduate students performed these tests with help from a post-doctoral researcher and the PI, while also pursuing their MS and PhD thesis investigations.

This report is organized in sections that describe the main accomplishments of the diagnostic development effort. These accomplishments include:

1. Development of a novel technique for measuring surface reaction rates in a plasma facility
2. Quantitative measurements of surface catalyzed recombination efficiencies for oxygen atoms combining on copper and hot and cold quartz
3. Measurements showing that surface catalyzed recombination in air plasma on copper proceeds first by $N+O+s \rightarrow NO+s$, contradicting current understanding
4. Quantitative measurement of the carbon nitridation rate for high temperature graphite, which is a component of many high temperature materials
5. Quantitative measurement of nitrogen atom recombination on hot graphite, which showed that N atom recombination is nearly fully catalyzed. This contradicts low temperature results from diffusion reactor studies.
6. Demonstration of material surface evolution during testing for SiC, which changes its properties
7. Development of a supersonic nozzle to reach higher heat flux levels and operation of the facility on pure oxygen
8. Development of a numerical code to simulate the conditions in the ICP Torch Facility using a state-of-the-art, open-source DNS code (NGA) coupled with the best high temperature gas property library available (MUTATION)
9. Establishment of the minimum requirements for a facility and diagnostics for material screening, including facility characterization

Each of these accomplishments is described in the following sections, with references to further detail in theses, conference papers, and published articles.

DISTRIBUTION A: Distribution approved for public release.

II. Measurement of Surface Reaction Rates (1-5)

The idea of applying laser diagnostic measurements to the near-wall region of a material surface in a high-temperature plasma flow is not new, and the current effort began with simulations of reacting boundary layers in air and nitrogen plasmas using a version of the Von Karman Institute's (VKI's) boundary layer code [1]. This parametric study assessed the influence of sample diameter, facility pressure, and surface catalycity on species number density distributions and temperature in the reacting boundary layer. From this study, estimates of laser beam energy, focal spot size, and species detectivity were developed for N and O atom LIF.

The measurement campaign at UVM started with copper and quartz samples exposed to nitrogen, air, and eventually oxygen plasmas while the laser was tuned to excite an appropriate electrical transition of either O or N as detailed below in Fig. 1.

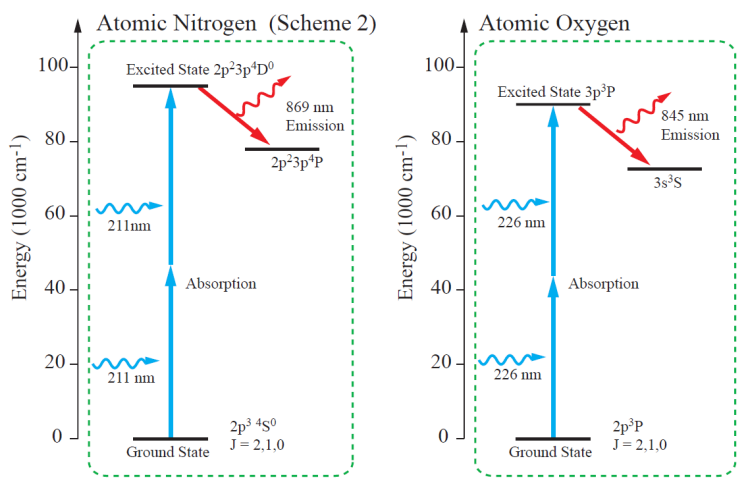

Fig. 1 Two-photon LIF excitation strategies for N and O

Simultaneous measurements of translation temperature and species number density are obtained by scanning the laser wavelength over the transition and recording both the beam energy and fluorescence from both the ICP Torch Facility and a microwave discharge flow reactor. The optical arrangement is shown in Fig. 2 below. This measurement approach requires that the facility be operating at a steady condition, and this is ensured by allowing sufficient time for the facility to come to thermal equilibrium. Stability of the plasma flow is ensured by proper choice of chamber pressure and mass flow rate to avoid typical free jet flow instabilities and to avoid transition to turbulent flow.

Measured property extraction from the measured signal levels is illustrated in Fig. 3. Temperature is found from the transition line width, and the spectrally integrated LIF signal is proportional to the total species density.

DISTRIBUTION A: Distribution approved for public release.

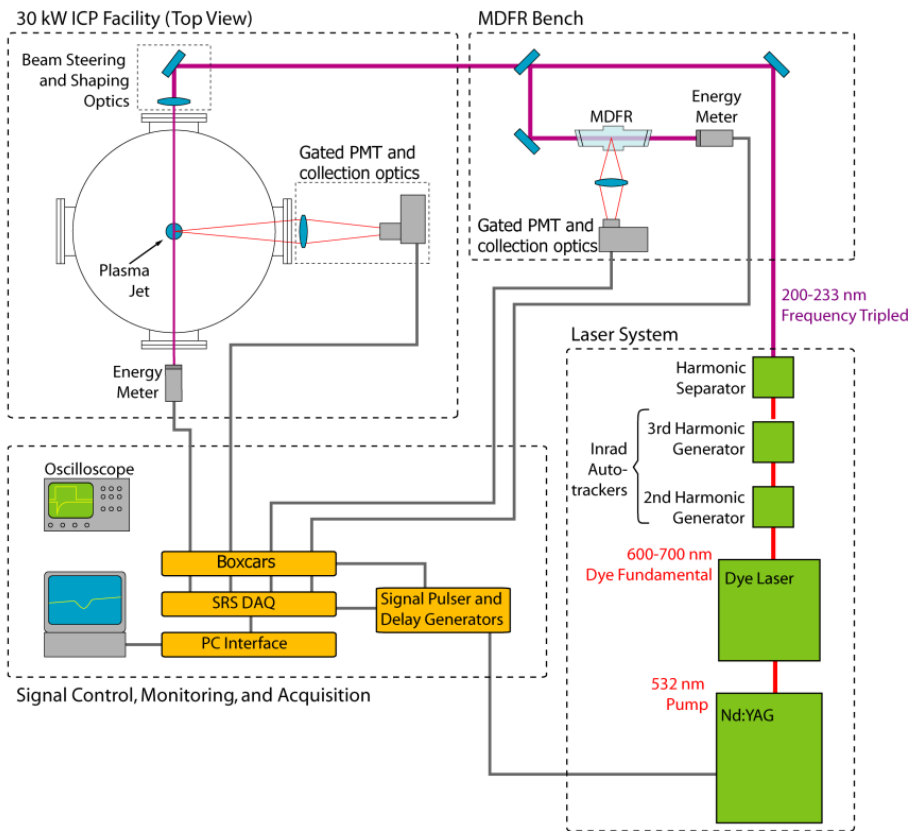

Fig. 2 Optical arrangement for LIF measurements in ICP Torch Facility

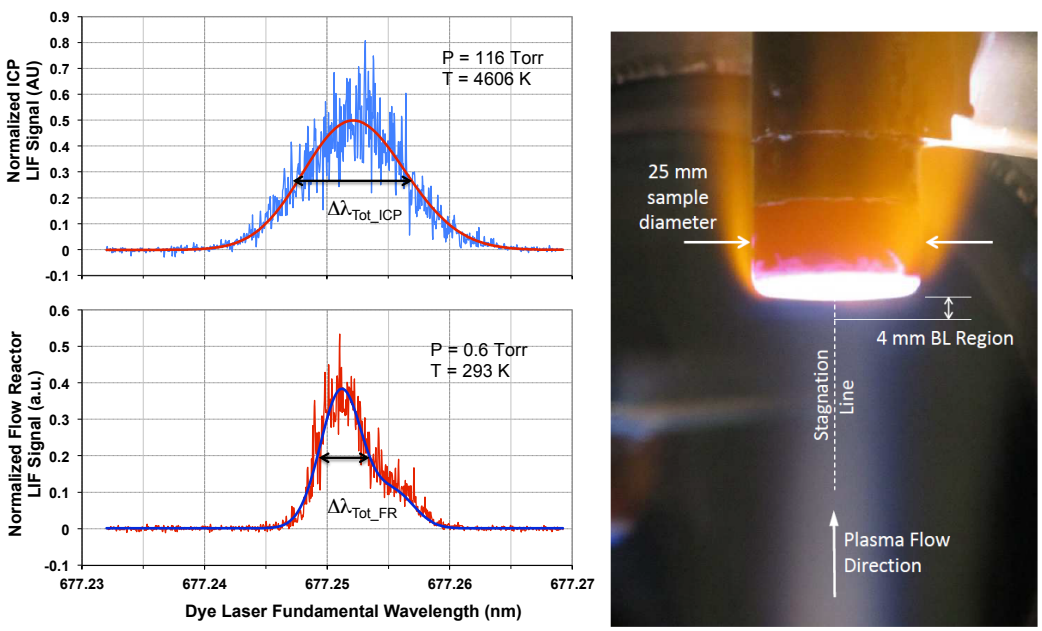

Fig. 3 ICP and MDFR LIF signals (left) and survey geometry (right)

The approach to measuring the surface reaction rates requires that the beam and detector alignment be preserved while moving both either toward or away from the surface. This is illustrated in the image at the right of Fig. 3.

DISTRIBUTION A: Distribution approved for public release.

Initial test results showed that the LIF-based approach could distinguish very well the difference between catalytic and non-catalytic surfaces. Figure 4 shows results for different surfaces exposed to oxygen-argon plasmas. The copper surface strongly catalyzes the oxygen atoms to form molecules, while both cold and hot quartz do not. The increase in the spectrally integrated area near the surface is following the total density trend in the constant pressure boundary layer. These results were described in conference and meeting papers [2-5].

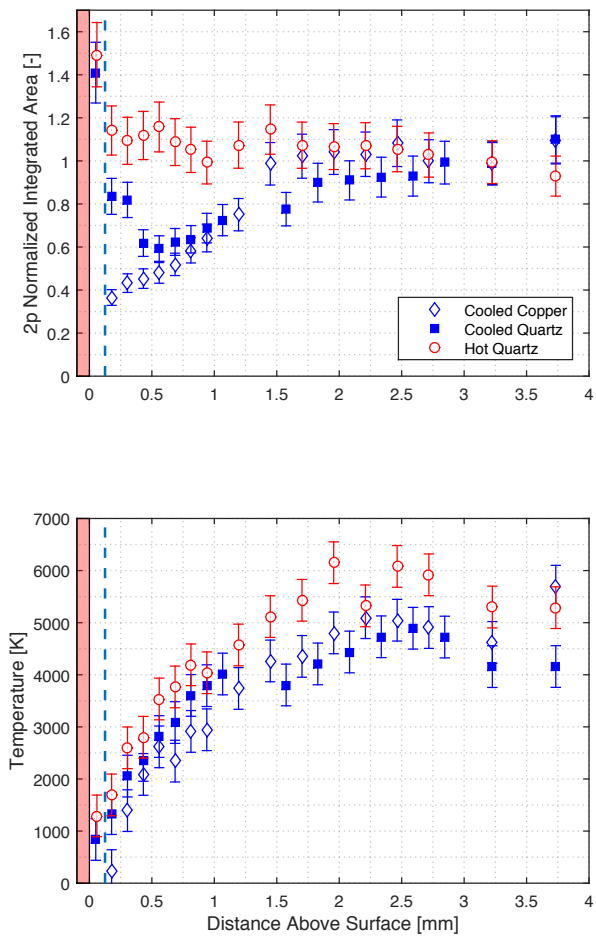

Fig. 4 LIF Measurements of temperature and integrated area for oxygen argon plasma

The most important contribution that UVM has made consists of developing the theoretical framework for deriving quantified surface reaction rate values from the measured values shown in Fig. 4. This process is illustrated in Fig. 5 for the case of a copper surface exposed to oxygen/argon plasma. The approach starts with Goulard's mass balance at the surface [6], which is then converted to a mole fraction basis to better make use of the flow properties measured by LIF. The measured area integrals are all normalized to the value at the boundary layer edge, which is near 3 mm. Variable relationships are indicated on the figure.

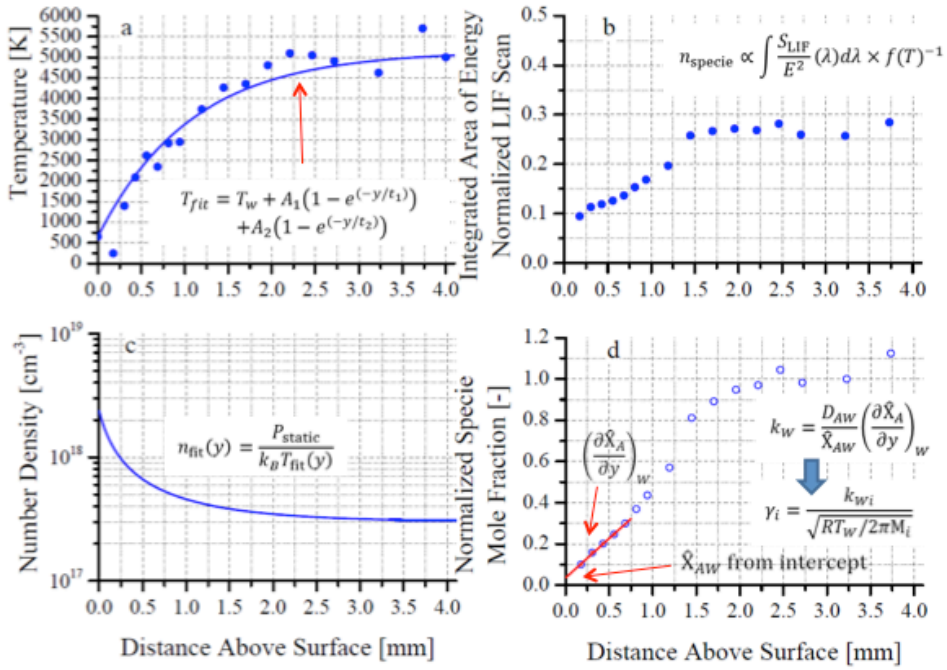

Fig. 5 Method for determining wall reaction rates from relative LIF measurements

This approach has been used to determine surface catalyzed recombination rates for atomic oxygen on copper, cold quartz, and hot quartz [7]. As mentioned therein, the values were: 1) cold copper, $\gamma = 0.0415 \pm 0.0056$; 2) cold quartz, $\gamma = 0.0016 \pm 0.0002$; and 3) hot quartz, $\gamma = 0.0091 \pm 0.0012$.

Similar measurements have been performed for nitrogen atom recombination in nitrogen [4] and air [5] plasmas and preliminary results for different materials are shown below in Fig. 6 for air plasma.

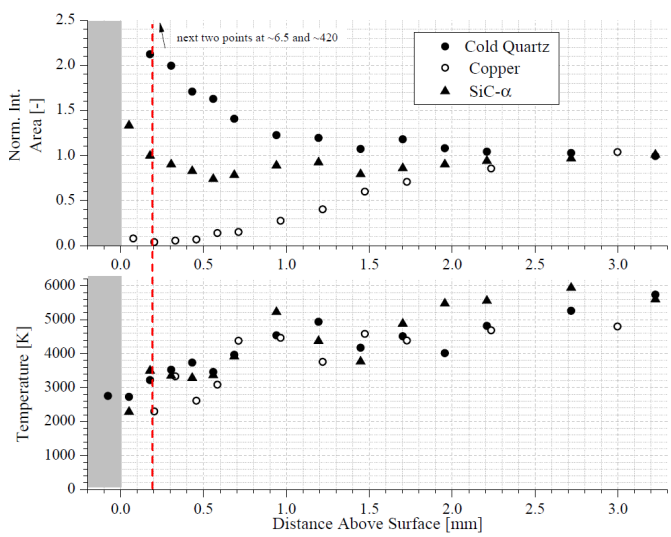

Fig. 6 N atom LIF results for different materials in air plasma

The results shown above in Fig. 6 indicate strong N atom consumption at the surface for the copper test. As discussed in [5] this does not happen in nitrogen plasma, which shows that cold copper is not strongly catalytic to nitrogen recombination. Moreover, measurements O atom LIF for air plasma over copper showed that oxygen atom density was nearly constant approaching the material surface, which contradicts the results shown above in Figs. 4 and 5. With the laser operating at 226 nm, additional efforts were made to probe NO LIF and these results showed strong non-equilibrium NO populations near the surface. This led to the conclusion that copper acts as a fully catalytic surface by first producing NO by N+O+s→NO+s, and then the fast gas phase reaction NO+N→N_2+O acts to deplete the nitrogen atom population near the wall while replenishing the oxygen atom population in the same region.

The approach has also been applied to the study of graphite nitridation, which yielded the interesting result that hot graphite is more catalytic to nitrogen atom recombination in nitrogen plasma than a cold copper surface. Measured flow properties are shown below in Fig. 7

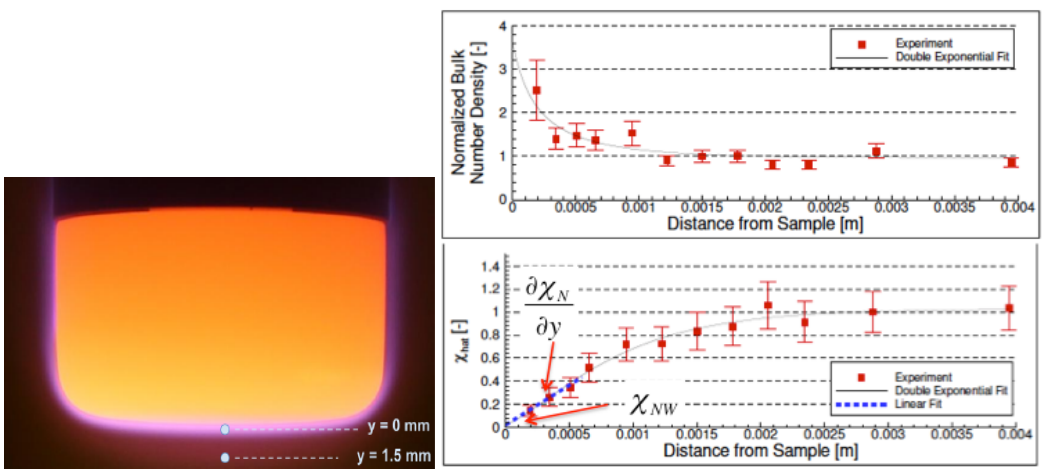

Fig. 7 LIF measurements of N atom over hot graphite

The analysis of the LIF measurements of atomic nitrogen and temperature were used to determine the nitridation and surface recombination rates [8] and these are summarized in the table below. The recombination rate for nitrogen on hot graphite is GREATER than that for oxygen on cold copper.

Reaction	k [m-s^{-1}]	γ
Total	59.8±14.9	0.153±0.039
Carbon Nitridation	2.51±0.44	0.00645±0.002
Nitrogen Recombination	57.25±14.9	0.147±0.039

Table 1. Rate values for nitridation and recombination for graphite

Direct evidence of molecular nitrogen formation at the surface was found by using high-resolution, spatially resolved emission measurements to detect

nitrogen emission from the first positive system (B→A) near 500 nm. The radial profiles shown below in Fig. 8 clearly show that at the location closest to the graphite surface there is a strong increase in the nitrogen molecule emission, while there is much less of an increase for hot quartz, which is known to be non-catalytic. This is direct evidence of the enhanced recombination for graphite [8]. This result contradicts results from diffusion reactor measurements for heated graphite [9].

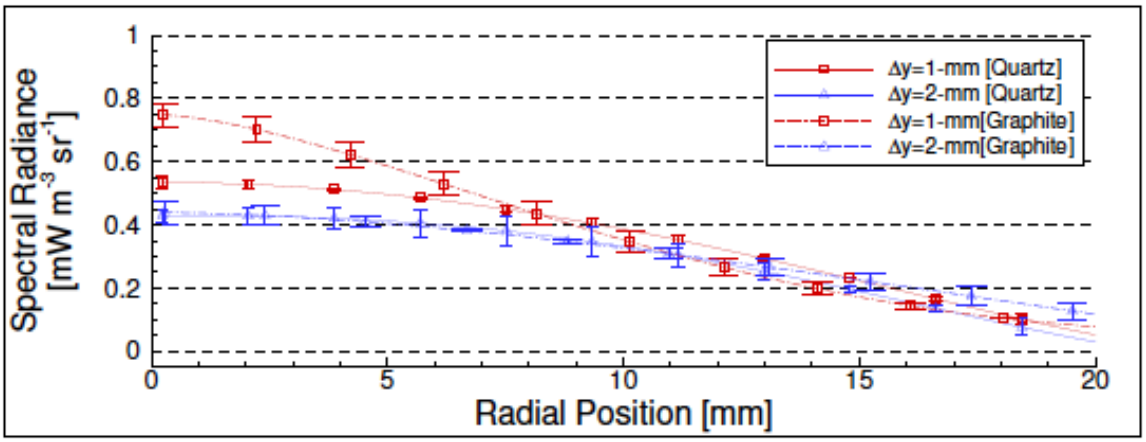

Fig. 8 Nitrogen molecule first positive emission over hot quartz and hot graphite

The ICCD camera offers a significant enhancement to the point-wise measurement capability that has been developed around the LIF diagnostic. A set of early images obtained of the reacting boundary layer is shown below for different laser focusing strategies (beam or sheet).

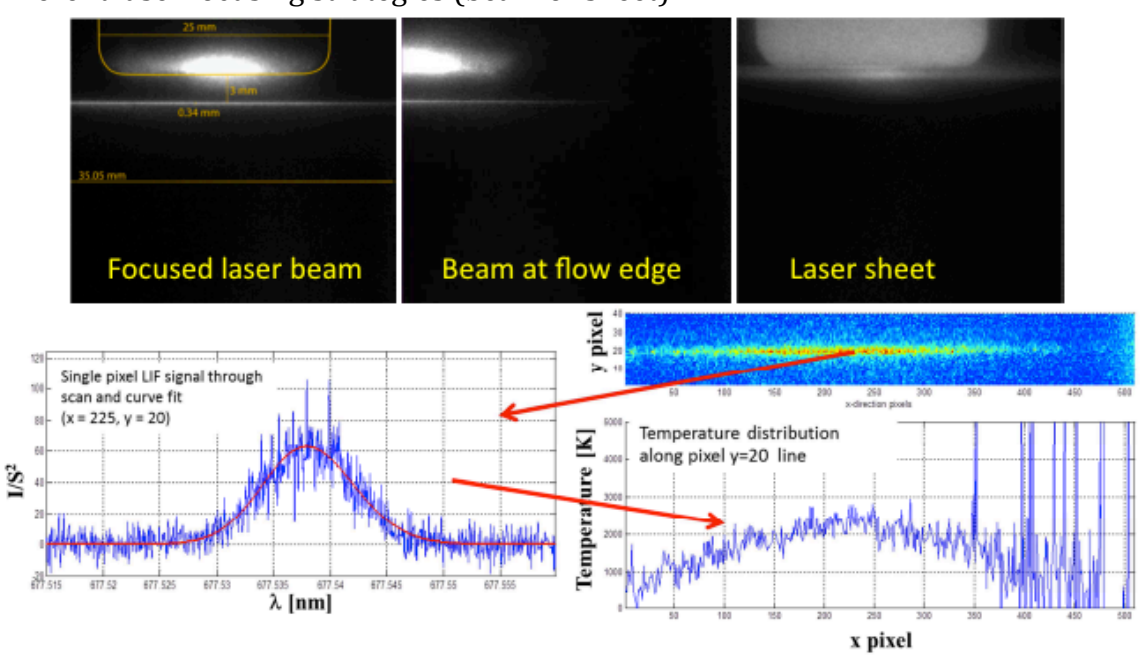

Fig. 9 ICCD camera recording field of LIF measurements for O atom in air plasma

When fully implemented this approach will yield both axial and radial species gradients to enable assessment of the radial influence on interpretation of surface reaction rates. This early work was reported in a conference paper [10]. Note that this camera has a state-of-the-art intensifier that has enhanced sensitivity at wavelengths that are needed for two-photon LIF applications.

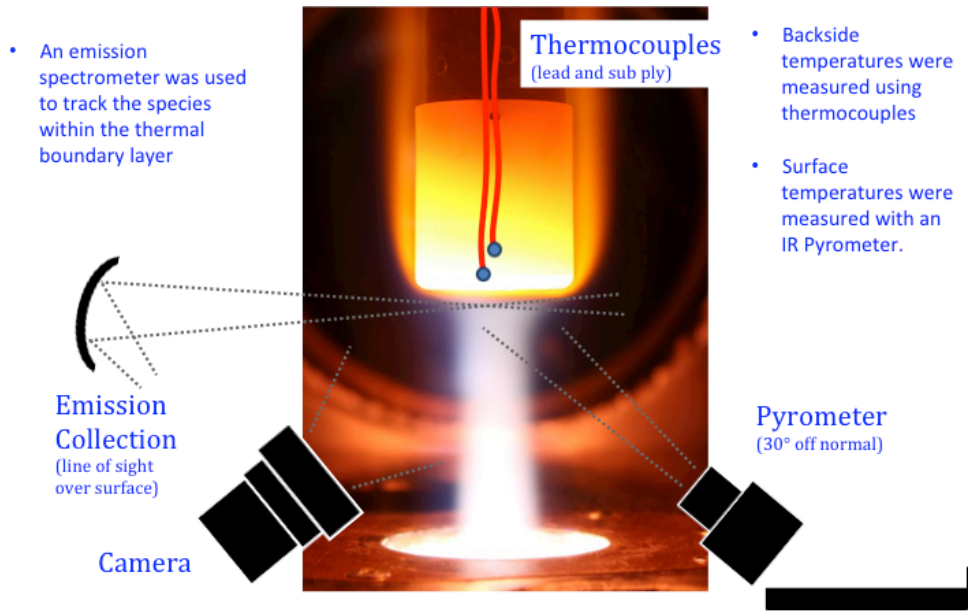

Fig. 10 Arrangement for studies of transient effects as materials oxidizes

III. Surface Property Evolution During Plasma Testing (6)

Using SiC cloth samples that were available from testing for the HIADS project, Owens looked at transient phenomena that were driven by exposure to atomic oxygen. This flexible TPS material is being developed for inflatable decelerators to serve as the outer protective material. Tests in the UVM ICP Torch Facility showed that this high-nicalon material performed reasonably well, and could survive to higher temperatures than other materials [11]. The test instrumentation for this investigation is shown above in Fig. 10. The materials were interesting as well because of the increased surface are compared to monolithic SiC. However, at the ICP Torch test conditions oxide layer growth was a volumetric phenomenon and not a surface one as for monolithic SiC.

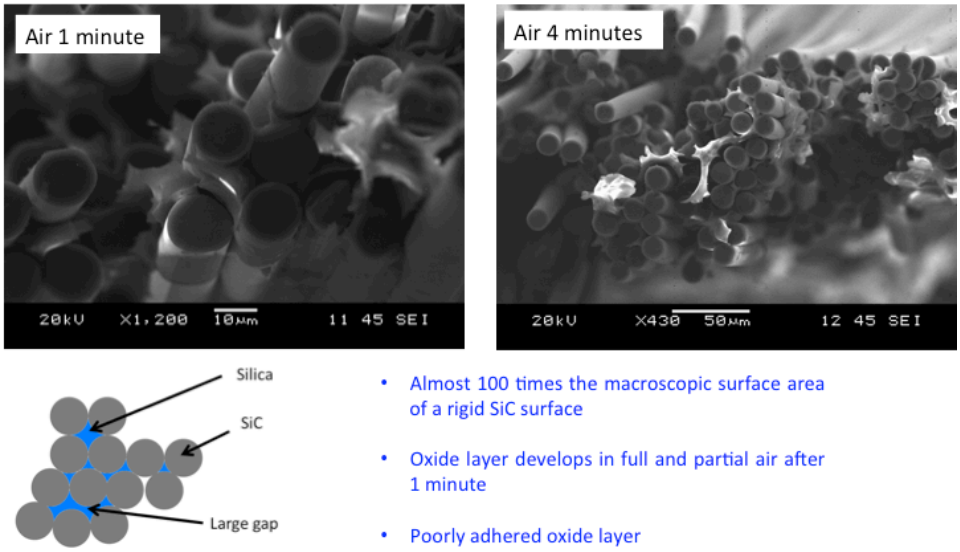

Fig. 11 Oxidation of flexible SiC showing silica growth in gaps

During oxidation the exothermic reactions leading to silica growth provided an increase in temperature for the material compared to tests in nitrogen plasma. This is shown by the surface temperature comparison for the left image in Fig. 12. Note that the oxidation effect appears to stabilize, and once the virgin material has developed the oxide content, then there is no further excess heating of the material and it eventually reaches a stable surface temperature. This is illustrated on the right side image. Nitrogen exposure also produces a transient effect that we currently interpreted as removing either oxygen or carbon from the surface.

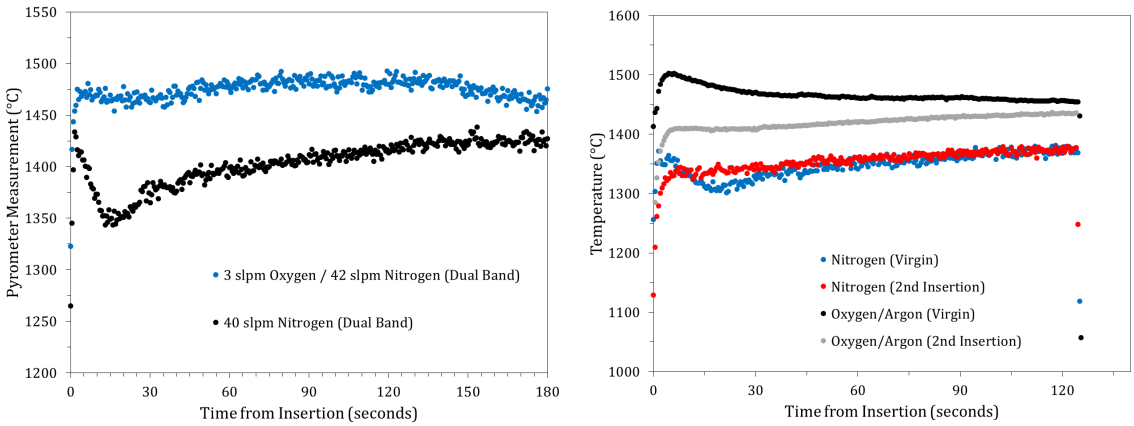

Fig. 12 Surface heating caused by oxidation (left) and surface temperature stabilization on re-exposure (right)

Further studies were conducted to look at emitting species near the surface of the flexible SiC coupons as the plasma composition changes. Results from these studies are shown below, where different spectral features are tracked as the plasma composition changes. The earlier part of the test shows that with exposure to nitrogen plasma the material temperature (indicated by gray body emission) is increasing and reaching a more stable value at about 9 min. There is a strong initial

transient peak in CN emission, which coincides with the temperature dip shown above. At 10 min, air is added and immediately the N emission decreases and O is clearly present near the surface. The O emission decrease from the peak tracks inversely with the increase in surface temperature. The O emission recovers as less O atom is incorporated in silica in the material.

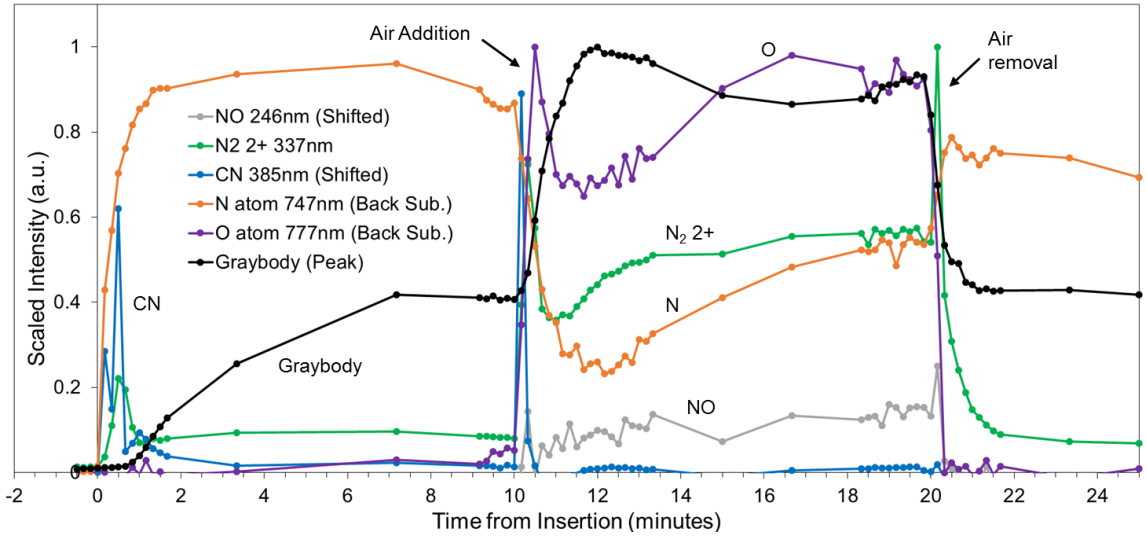

Fig. 13 Emitting species and gray body emission for SiC in different plasmas

These tests show that measured quantities, including surface catalyzed recombination rates, depend on the time that the measurements are made. The virgin material surface is highly reactive to atomic oxygen and then it becomes passive after about 10 min exposure. Note that oxidation strongly weakened the material [12]. This material has been useful for illustrating the link between the processes shown in Fig. 14 below:

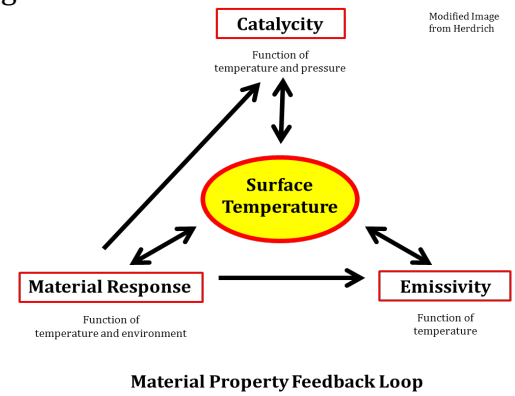

Fig. 13 Link between material properties during exposure to plasma

IV. Enhancements to ICP Torch Facility (7)

Efforts to improve the facility to reach higher surface temperatures on materials such as SiC fostered investigations of water-cooled induction coils, which did not work well. Additional efforts led to the development of a supersonic nozzle, and this

did work, providing supersonic flow and higher heating rates to material samples [13]. This work was funded by AFOSR, and it is being followed up with a senior design project to provide "swing-in" capability for the nozzle so that it can be installed during plasma tests. An image of the hot plasma flow is shown at the left hand side of Fig. 14 below. The image was for air in argon, and the classical diamond pattern of accelerating and decelerating supersonic flow is clearly seen. At the center is the subsonic plasma jet for air plasma, showing stable laminar flow. The right hand image shows the plasma jet operating on pure oxygen, which was made possible by re-plumbing the facility with special Teflon tape to reduce potential sparking from human body oil on regular tape.

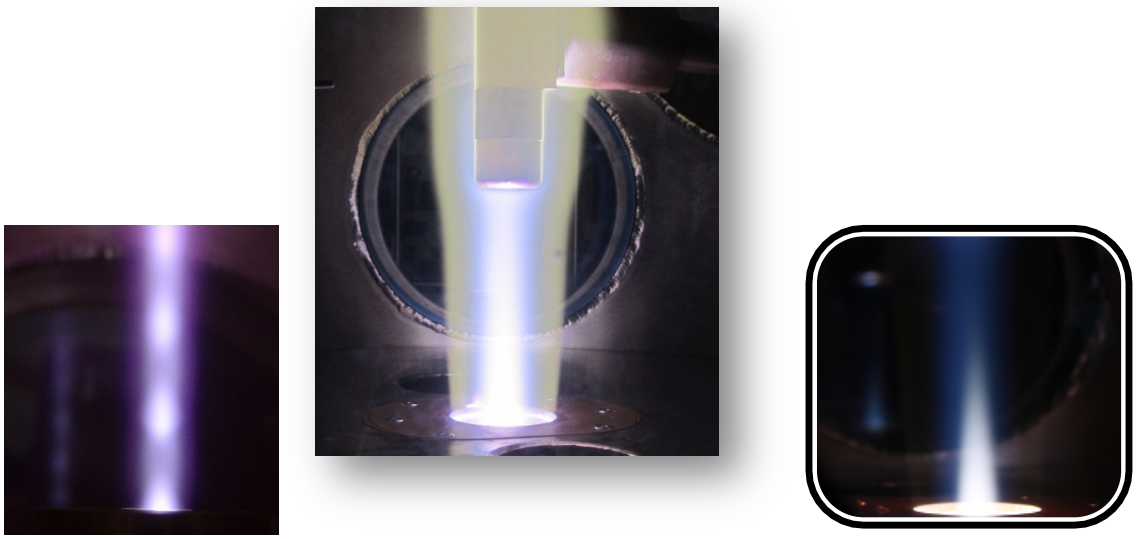

Fig. 14 ICP Torch facility: supersonic operation (left); laminar air plasma (center) and pure oxygen (right)

V. Numerical Model of ICP Flow (8)

AFOSR funding supported one graduate student who spent two years of intensive study to develop a numerical model of the flow facility. Working with Prof. Dubief and his graduate students, Max Dougherty incorporated the needed high temperature gas property library (MUTATION from VKI) into the NGA flow solver.

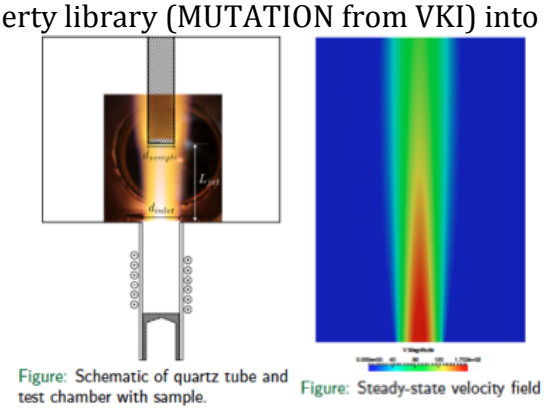

Fig. 15 Velocity field in subsonic ICP Torch Facility

A computation of the velocity field is shown above in Fig. 15 for a typical ICP Torch Facility operating condition. The simulation starts with inflow conditions at the quartz tube exit and resolves the flow and thermal properties up to and including a simple sample geometry as illustrated on the left hand side of the figure.

The code is being validated against standard test cases, and it is also being used to replicate tests that have been conducted at UVM as shown below in Fig. 16 where nitrogen mole fraction values in the axial direction above the sample surface are compared with code predictions that are computed for different catalytic efficiencies [14].

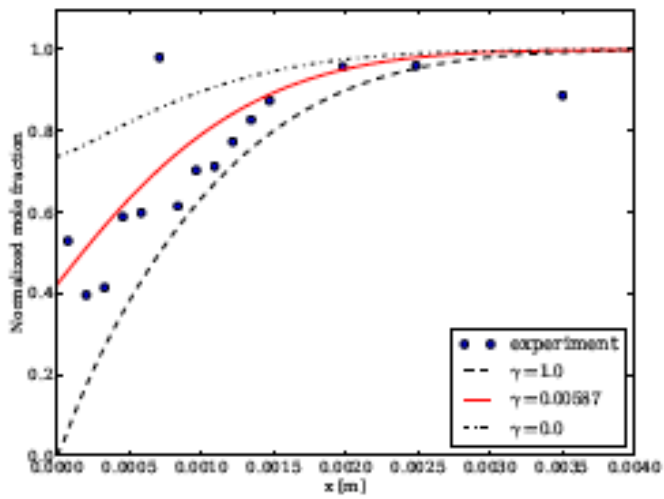

Fig. 16 Early comparison between measured and calculated relative mole fraction values for nitrogen plasma and quartz

VI. Facility and Diagnostic Requirements for Material Screening (9)

The need for more rapid development of performant high-temperature materials has been recognized by DoD, NASA and DARPA and we gave our recommendations for how this can be accomplished at a recent meeting devoted to this subject [15]. Based on the lessons learned during material testing for ISU, UWM and MO-SCI, we recommend the following facility and diagnostic configuration be considered for improved material screening:

1. Surface temperature measurement with two-color pyrometer
2. Radiometer to allow wide band assessment of emissivity
3. Fully-catalytic cold wall heat flux measurements
4. High definition video camera to record surface evolution during tests
5. Mass loss characterization (by camera during tests if needed)
6. Near-surface emission measurements for UV-NIR region (this also can provide independent measurement of surface temperature if needed)

DISTRIBUTION A: Distribution approved for public release.

7. Documentation of facility test conditions including:
    a. Stagnation pressure at sample surface
    b. Velocity gradient at boundary layer edge
    c. Flow enthalpy (with documentation of measurement technique)
    d. Atomic species densities at boundary layer edge

Note that the last three requirements amount to fully characterizing the plasma facility test conditions. This is not a trivial exercise, but if it is not done, then there is no knowledge of what environment heated the material.

VII. Grant Statistics

Archival Publications

1. D. G. Fletcher and J. M. Meyers, "Surface Catalyzed Reaction Efficiencies in Oxygen Plasmas from Laser Induced Fluorescence Measurements", Submitted to *J. Thermophysics & Heat Transfer*, December 2015.
2. W. Owens, D. Merkel, F. Sansoz and D. Fletcher, "Fracture Behavior of Woven Silicon Carbide Fibers Exposed to High-Temperature Nitrogen and Oxygen Plasmas", *J. Am Ceram. Soc.*, Vol 98, No. 12, pp. 4003-4009, December 2015.
3. A. J. Lutz, "Experimental Investigation and Analysis of High-Enthalpy Nitrogen Flow over Graphite", Ph.D. Thesis, May, 2015
4. M. J. Dougherty, "Numerical Simulations of Reacting Flow in an Inductively Coupled Plasma Torch", Ph. D. Thesis, May, 2015
5. W. P. Owens, "Aerothermal Characterization of SiC Flexible TPS Using a 30 kW ICP Torch", Ph. D. Thesis, May, 2015
6. D. A. Hurley, D. R. Huston, and D. G. Fletcher, "Remote Monitoring of Harsh Environments using Acoustic Emissions", *J. Engineering Mechanics*, Vol 139, No. 3, pp. 286-295, March, 2013. (owing to an oversight, the AFOSR grant was NOT acknowledged).
7. J. M. Meyers, W. P. Owens, and D. G. Fletcher, "Detection of Surface Catalyzed Reaction Products", Catalytic Gas Surface Interactions, AVT Specialist's Meeting AVT-199/RSM-0029, January 2013
8. W. P. Owens, J. M. Meyers, A. J. Lutz, S. Smith, and D. G. Fletcher, "Direct Assessment of Surface Catalyzed Reaction Efficiencies", Catalytic Gas Surface Interactions, AVT Specialist's Meeting AVT-199/RSM-0029, January 2013
Published electronically by the Applied Vehicle Technology Panel of the NATO Science and Technology Organization, (see http://www.cso.nato.int) for NATO countries only plus Japan, Switzerland and Russia. (Chair and Editor: D. G. Fletcher)

Refereed Conference Proceedings:

1. Owens, W. P., Meyers, J. M., and Fletcher, D. G., "Flexible TPS Surface Catalysis Testing in a 30 kW ICP Torch Facility", AIAA 2012-3095, 43rd AIAA Thermophysics Conference, New Orleans, June (2012).

2. A. J. Lutz, W. P. Owens, J. M. Meyers, and D. G. Fletcher, "Experimental Analysis of Carbon Nitridation and Oxidation Efficiency with Laser-Induced Fluorescence", AIAA 2013-0924, 51st AIAA Aerospace Sciences Meeting, January (2013)
3. J. M. Meyers, W. P. Owens, and D. G. Fletcher, "Surface Catalyzed Reaction Efficiencies in Nitrogen and Oxygen Plasmas from Laser Induced Fluorescence Measurements", AIAA 2013-3139, 44th AIAA Thermophysics Conference, June, (2013)
4. Meyers J. M., Owens, W. P., and Fletcher, D. G., "Surface Catalyzed Reaction Efficiencies in Air Plasmas Using Laser Induced Fluorescence Measurements", AIAA 2013-3140, 44th AIAA Thermophysics Conference, June (2013)
5. W. P. Owens, J. M. Meyers, and D. G. Fletcher, "Surface Catalysis and Oxidation of Flexible Thermal Protection Materials in Air Plasma", AIAA 2013-3141, 44th AIAA Thermophysics Conference, June, (2013)
6. A. J. Lutz and D. G. Fletcher, "Investigation of Non-Equilibrium Nitrogen Plasmas", AIAA 2015-2961, 46th AIAA Thermophysics Conference, June, (2015)
7. J. M. Meyers and D. G. Fletcher, "Planar Two-Photon LIF Measurements of Atomic Species in a High-Temperature Inductively Coupled Plasma Environment", AIAA 2015-2959, 46th AIAA Thermophysics Conference, June, (2015)
8. W. P. Owens, J. M. Meyers, and D. G. Fletcher, "Surface Reaction and Oxidation Effects on Flexible Thermal Protection Materials", TP15-0402, CAMX - The Composites and Advance Materials Expo, October, (2015).

Journal Articles in Progress:

1. W. P. Owens and D. G. Fletcher, "Material Response of Silicon Carbide Flexible TPS during a Simulated Mars Entry", to be submitted to *Applied Surface Science*
2. W. P. Owens, J. M. Meyers and D. G. Fletcher, "Transient Thermal Properties of SiC Fabrics Caused by Oxidation", to be submitted to *Journal of the American Ceramic Society*
3. W. P. Owens, S. F. Smith, J. Uhl, J. M. Meyers, M. J. Dougherty, A. J. Lutz and D. G. Fletcher, "Development of a 30 kW Inductively Coupled Plasma Torch for Performance Analysis of New Flexible TPS Materials", to be submitted to *Aerospace Science and Technology*
4. W. P. Owens and D. G. Fletcher, "Theoretical and Experimental Analysis of SiC Oxidation in an Aerothermal Environment", journal TBD
5. W. P. Owens, D. M. Merkel, F. Sansoz, and D. G. Fletcher, "Propagation of Exothermic Oxidation Reactions Leading to Catastrophic Failure of SiC Flexible TPS Materials", to be submitted to *Journal of Materials Engineering and Performance*
6. A. J. Lutz, W. P. Owens, J. M. Meyers, and D. G. Fletcher, "Experimental Analysis of Carbon Nitridation Efficiency with Laser-Induced Fluorescence", to be submitted to *Journal of Thermophysics and Heat Transfer*
7. D. G. Fletcher, J. M. Meyers, and W. P. Owens, "Surface Catalyzed Reaction Efficiencies in Nitrogen Plasmas from Laser Induced Fluorescence Measurements", to be submitted to *Journal of Thermophysics and Heat Transfer*

DISTRIBUTION A: Distribution approved for public release.

8. Meyers J. M., Owens, W. P., and Fletcher, D. G., "Surface Catalyzed Reaction Efficiencies in Air Plasmas Using Laser Induced Fluorescence Measurements", to be submitted to *Journal of Thermophysics and Heat Transfer*

Patents: None

Disclosures: None

Presentations (not listed above in conference proceedings):

1. W. Owens, D. Merkel, D. Fletcher and F. Sansoz, "Aero-thermal Testing of Silicon Carbide Flexible TPS in a 30 kW ICP Torch Facility", Materials Science and Technology Meeting, Montreal, October 30, 2013.
2. D. G. Fletcher, W. P. Owens, and J. M. Meyers, "Measurements of Surface Catalyzed Recombination Efficiencies by Laser-Induced Fluorescence", 38th Annual Conference on Composites, Materials and Structures, Cocoa Beach, January 27, 2014
3. W. P. Owens, J. M. Meyers, and D. G. Fletcher, "Performance Report for SiC Flexible TPS in a 30 kW ICP Torch Facility", Presented to HIADS, April 15, 2013
4. W. P. Owens, D. M. Merkel, F. Sansoz and D. G. Fletcher, "Oxidation of SiC Thermal Protection Blankets", 38th Annual Conference on Composites, Materials and Structures, Cocoa Beach, January 27, 2014
5. D. G. Fletcher, "Testing Advanced High-Temperature Materials in High-Enthalpy Environments", Technical Interchange Meeting on Ground Testing for Materials Screening, Tullahoma, TN, November 19, 2014
6. D. G. Fletcher, "Testing Advanced High-Temperature Materials in High-Enthalpy Environments", Workshop on Methods of Materials Screening for High Speed Aerospace Applications, Chantilly, VA, June 22, 2015.
7. C. Tillson, "Investigation of Pyrolysis Gas Chemistry in an Inductively Coupled Plasma Facility", 7th Ablation Workshop, Tullahoma, TN, October 21, 2015.

Test Reports For this Grant:

<u>Missouri S&T – Hilmas, Fahrenholtz, Marschall</u>

1. J. M. Meyers, W. P. Owens, D. G. Fletcher, and J. Marschall, "Zirconium Diboride UHTC Material Testing Report", November 8 2012.

<u>ISU and U. Wisconsin-Madison: Akinc, Kramer, Perepezko, Marschall</u>

2. J. M. Meyers, W. P. Owens, S. F. Smith, and D. G. Fletcher, "Coated Molybdenum Testing – 25 mm Samples", September 26, 2012 (testing from July, 2012)
3. J. M. Meyers, W. P. Owens, and D. G. Fletcher, "Coated Molybdenum Testing – 18 mm Samples", February 28, 2014. (covered tests from October, 2013)
4. J. M. Meyers, W. P. Owens, A. J. Lutz, C. C. Tillson and D. G. Fletcher, "Coated Molybdenum Testing – Conical Sample", May 13, 2014 (covered testing through May for sharper tipped samples)

DISTRIBUTION A: Distribution approved for public release.

4. J. M. Meyers, A. J. Lutz, C. C. Tillson, L. Allen and D. G. Fletcher, "Pre-oxidized and Untreated ZrB2/SiC Samples", September 30 2014 (most recent tests for uncoated samples).
5. J. M. Meyers, C. C. Tillson, L. Allen and D. G. Fletcher, "MOSCI ZrB2-20 ZrC Test Report, February 6, 2015
6. J. M. Meyers, C. C. Tillson, W. P. Owens, and D. G. Fletcher, "Conical Diboride Sample Testing Report ISU", April 16, 2015
7. J. M. Meyers, C. C. Tillson, L. Allen and D. G. Fletcher, "Conical Sample Test Report UW-Madison 2015", July 09, 2015

VIII. References

1. D. G. Fletcher, J. Thoemel, O. Chazot, and J. Marschall, "Realization of a Gas-Surface Interaction Test Case for Model Validation", AIAA Paper No. 2010-1249, 48th Aerospace Sciences Meeting, Orlando, January, (2010).
2. W. P. Owens, J. M. Meyers, A. J. Lutz, S. Smith, and D. G. Fletcher, "Direct Assessment of Surface Catalyzed Reaction Efficiencies", Catalytic Gas Surface Interactions, AVT Specialist's Meeting AVT-199/RSM-0029, January 2013
3. J. M. Meyers, W. P. Owens, and D. G. Fletcher, "Detection of Surface Catalyzed Reaction Products", Catalytic Gas Surface Interactions, AVT Specialist's Meeting AVT-199/RSM-0029, January 2013
4. J. M. Meyers, W. P. Owens, and D. G. Fletcher, "Surface Catalyzed Reaction Efficiencies in Nitrogen and Oxygen Plasmas from Laser Induced Fluorescence Measurements", AIAA 2013-3139, 44th AIAA Thermophysics Conference, June, (2013)
5. J. M. Meyers, W. P. Owens, and D. G. Fletcher, "Surface Catalyzed Reaction Efficiencies in Air Plasmas Using Laser Induced Fluorescence Measurements", AIAA 2013-3140, 44th AIAA Thermophysics Conference, June (2013)
6. R. Goulard, "On Catalytic Recombination Rates in Hypersonic Stagnation Heat Transfer", Jet Propulsion, Vol. 28, pp. 73 - 85, November (1958).
7. D. G. Fletcher and J. M. Meyers, "Surface Catalyzed Reaction Efficiencies in Oxygen Plasmas from Laser Induced Fluorescence Measurements", Submitted to *J. Thermophysics & Heat Transfer*, December 2015.
8. A. J. Lutz, "Experimental Investigation and Analysis of High-Enthalpy Nitrogen Flow over Graphite", Ph.D. Thesis, May, 2015
9. L. Zhang, D. Pejakovic, J. Marschall, and D. G. Fletcher, "Laboratory Investigation of Active Graphite Nitridation by Atomic Nitrogen", *J. Thermophysics & Heat Transfer*, Vol 25, No 2, pp. 193 -200 (2011).
10. J. M. Meyers and D. G. Fletcher, "Planar Two-Photon LIF Measurements of Atomic Species in a High-Temperature Inductively Coupled Plasma Environment", AIAA 2015-2959, 46th AIAA Thermophysics Conference, June, (2015)
11. W. P. Owens, J. M. Meyers, and D. G. Fletcher, "Surface Reaction and Oxidation Effects on Flexible Thermal Protection Materials", TP15-0402, CAMX - The Composites and Advance Materials Expo, October, (2015).

12. W. Owens, D. Merkel, F. Sansoz and D. Fletcher, "Fracture Behavior of Woven Silicon Carbide Fibers Exposed to High-Temperature Nitrogen and Oxygen Plasmas", *J. Am Ceram. Soc.*, Vol 98, No. 12, pp. 4003-4009, December 2015.
13. S. F. Smith, "Investigation of Subsonic and Supersonic Flow Characteristics of an Inductively Coupled Plasma Torch", MS Thesis, University of Vermont, Burlington, VT, May, 2013.
14. M. J. Dougherty, "Numerical Simulations of Reacting Flow in an Inductively Coupled Plasma Torch", Ph. D. Thesis, May, 2015
15. Technical Interchange Meeting on Ground Testing for Materials Screening, Tullahoma TN, November 19 2014.

DISTRIBUTION A: Distribution approved for public release.

1.

1. Report Type

Final Report

Primary Contact E-mail
Contact email if there is a problem with the report.

douglas.fletcher@uvm.edu

Primary Contact Phone Number
Contact phone number if there is a problem with the report

802-656-9863

Organization / Institution name

University of Vermont

Grant/Contract Title
The full title of the funded effort.

Mo-Si-B Alloys and Diboride Systems for High-Enthalpy Environments: Design and Evaluation

Grant/Contract Number
AFOSR assigned control number. It must begin with "FA9550" or "F49620" or "FA2386".

FA9550-11-1-0201

Principal Investigator Name
The full name of the principal investigator on the grant or contract.

Douglas G. Fletcher

Program Manager
The AFOSR Program Manager currently assigned to the award

Dr. Ali Sayir

Reporting Period Start Date

09/15/2011

Reporting Period End Date

09/14/2015

Abstract

This final report summarizes work done by researchers from Iowa State University, University of Wisconsin-Madison, SRI International, and University of Vermont for this grant. The first two groups investigated candidate material systems for high-temperature aerospace applications. These investigations included theoretical, computational and experimental efforts, and focused mainly on molybdenum-silicon-boron and diboride alloy systems. These two groups also collaborated in the production of candidate test samples for evaluation in the inductively coupled plasma torch facility at the University of Vermont, and the molyborosilicate coating performed very well in plasma tests. Researchers from SRI International and the University of Vermont collaborated on the development of improved non-intrusive diagnostics aimed at providing measurements of key gas-surface interactions at plasma torch test conditions that could be related to flight environments. University of Vermont personnel focused their efforts on making quantitative measurements of key surface reaction rates from relative laser based measurements of the reacting species gradients near the surface.

Distribution Statement
This is block 12 on the SF298 form.

Distribution A - Approved for Public Release

DISTRIBUTION A: Distribution approved for public release.

Explanation for Distribution Statement

If this is not approved for public release, please provide a short explanation. E.g., contains proprietary information.

SF298 Form

Please attach your SF298 form. A blank SF298 can be found here. Please do not password protect or secure the PDF The maximum file size for an SF298 is 50MB.

SF 298_df.pdf

Upload the Report Document. File must be a PDF. Please do not password protect or secure the PDF . The maximum file size for the Report Document is 50MB.

FA9550-11-1-0201_final.pdf

Upload a Report Document, if any. The maximum file size for the Report Document is 50MB.

Archival Publications (published) during reporting period:

These are listed in each of the three reports by group. The publication by SRI International is included. Please contact me if a separate list of ALL archival publications needs to be compiled.

Changes in research objectives (if any):

None

Change in AFOSR Program Manager, if any:

None

Extensions granted or milestones slipped, if any:

None

AFOSR LRIR Number

LRIR Title

Reporting Period

Laboratory Task Manager

Program Officer

Research Objectives

Technical Summary

Funding Summary by Cost Category (by FY, $K)

	Starting FY	FY+1	FY+2
Salary			
Equipment/Facilities			
Supplies			
Total			

Report Document

Report Document - Text Analysis

Report Document - Text Analysis

Appendix Documents

2. Thank You

E-mail user

Jan 13, 2016 12:00:39 Success: Email Sent to: douglas.fletcher@uvm.edu